GETTING A HANDLE ON CARBON NANOTUBES

A Dissertation

Presented to the Faculty of the Graduate School

of Cornell University

In Partial Fulfillment of the Requirements for the Degree of

Doctor of Philosophy

by

Samantha Pamela Roberts

January 2014

GETTING A HANDLE ON CARBON NANOTUBES

Samantha Pamela Roberts, Ph. D.

Cornell University 2014

A single wall carbon nanotube is a linear polymer with exceptional mechanical properties. In particular with nanometer diameter and micron length scale a CNT has a high aspect ratio combined with unsurpassed mechanical strength. A CNT provides the ideal geometry for a truly molecular scale bio-mechanical probe.

The work in this thesis was motivated by the concept of "getting a handle" on CNTs. We sought to be able to use the NT as a probe that could both exert forces and measure forces acting on it. The questions this thesis seeks to answer are twofold. (i*) Can a carbon nanotube be used to probe biological systems at the molecular scale?* And conversely: (ii) *Can the techniques of single molecule biology be used to probe an individual carbon nanotube?* In the process of answering these questions we have derived several different functional platforms for cell investigations, single molecule experiments, and exploration of CNT mechanics, as we will see.

Chapters 1 through 3 introduce the unique properties of CNTs, mechanical theory, and growth methods. Chapter 4 shows motivating experiments where living cell-CNT interactions are studied. In Chapter 5 we demonstrate the ability to be able to fabricate highly aligned and parallel cantilevered CNTs—a necessary step toward realizing a probe for application.

In Chapters 6-9 we will describe a platform we have developed borrowing the technique of magnetic-tweezers from the biophysics community. This technique has been used in single-molecule studies to elucidate the properties of long biopolymers such as DNA using magnetic tags to optically resolve the molecules as well as exert forces upon them. In our work we show a similar scheme where the CNT is the molecule of interest. In our design the CNT devices are made by lithographically patterned magnetic iron pads at their ends. With this pad we can both optically resolve to position of the NT as well as exert forces on it. We will show how analysis of

thermal fluctuations gives us measurement methods that are sensitive enough to elucidate the mechanical properties of the NTs. Additionally we can now exert well calibrated forces on the NT on the scale of fN-pN. We conclude by showing how this platform provides a new way to further study the physical properties of CNTs and simultaneously provides the framework to study the forces acting in CNT—biomolecule interactions.

BIOGRAPHICAL SKETCH

Samantha Pamela Roberts was born in 1968 in New Brunswick, New Jersey, and grew up in a small town in Fairfield County Connecticut. Leading an unconventional life from the start, Samantha left home before completing high school to seek her own path through the world. After establishing a successful business and home in Long Island, New York, Samantha returned to school at the age of 31— she first completed her AS in Computer Science at Nassau Community College in 2000, where she was introduced to physics. Samantha then gave up practicalities for passions, selling her house and followed her newfound academic interests to Stony Brook University. Samantha completed her undergraduate studies in 2005 with a major in Physics and a minor in Mathematics. She then continued her studies as a graduate student at Cornell University, where she was fortunate to work and study under the guidance and unfaltering support of Professor Paul L. McEuen. The lessons learned during this graduate experience have been the most epic and life changing experience yet for Samantha, and she is not expecting the future to be any less exhilarating than the past.

Why? Because it's there.

—George Mallory, 1924

ACKNOWLEDGMENTS

I would not be looking at such a beautiful view if it were not for this ivory city on the hill and my McEuenite family.

TABLE OF CONTENTS

Chapter 1

Introduction

1.1 Introduction and Motivation

This thesis seeks to answer two questions:

(i) *Can a carbon nanotube be used to probe biological systems at the molecular scale?*

And conversely:

(ii) *Can the techniques of single molecule biology be used to probe an individual carbon nanotube?*

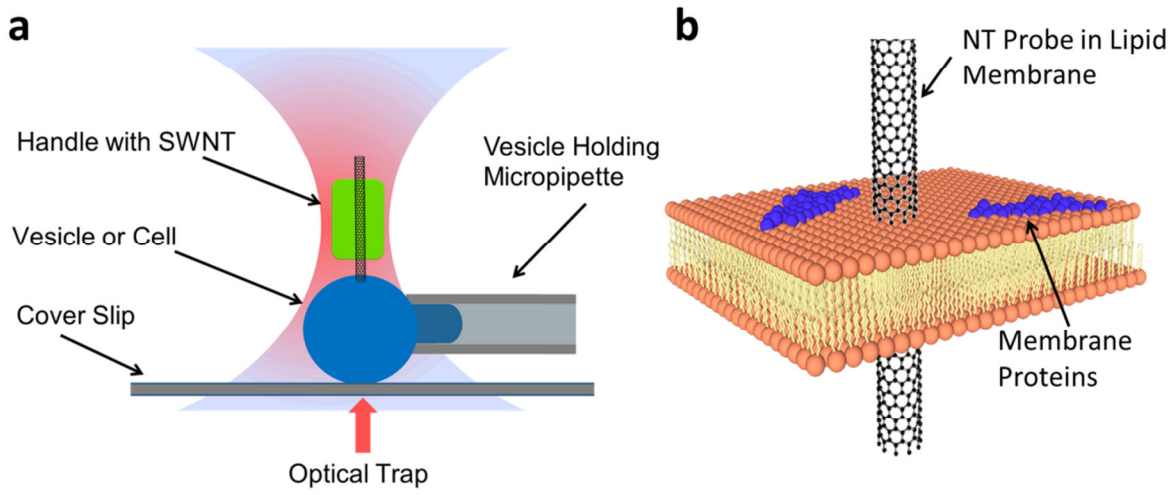

Figure 1.1 Conceptual schematics of a NT implemented as a mechanical probe/sensor. (a) Experiment where NT is attached to a dielectric handle and manipulated by an optical trap. (b) Illustration of a single wall CNT probe interacting with a cell membrane. We note the membrane thickness is 4 nm and the NT diameter averages 1-2 nm.

A potential experiment in the first category is shown in Figure 1.1(a). In this illustration the single wall CNT (black vertical line) is attached to a dielectric handle (green) which is actuated by an optical laser trap which would both exert forces on the NT and measure forces acting on it.

The NT is illustrated probing a cell (blue). A close up view of what the experiment would look like at the molecular level can be seen in Figure 1.1(b). Here we see a CNT penetrating through a 4 nm thick cell membrane, with a NT drawn with accurate diameter relative to the membrane thickness. With this image we get an appreciation of the truly molecular scale of the NT and the exciting new class of experiments that could be conducted with precise control of a SWNT probe

While an optically trappable NT probe of this particular sort has yet to be realized, the work in this thesis was motivated by this concept of "getting a handle" on CNTs. In the process of these studies we have derived several different functional platforms for cell investigations, single molecule experiments, and exploration of CNT mechanics, as we will see.

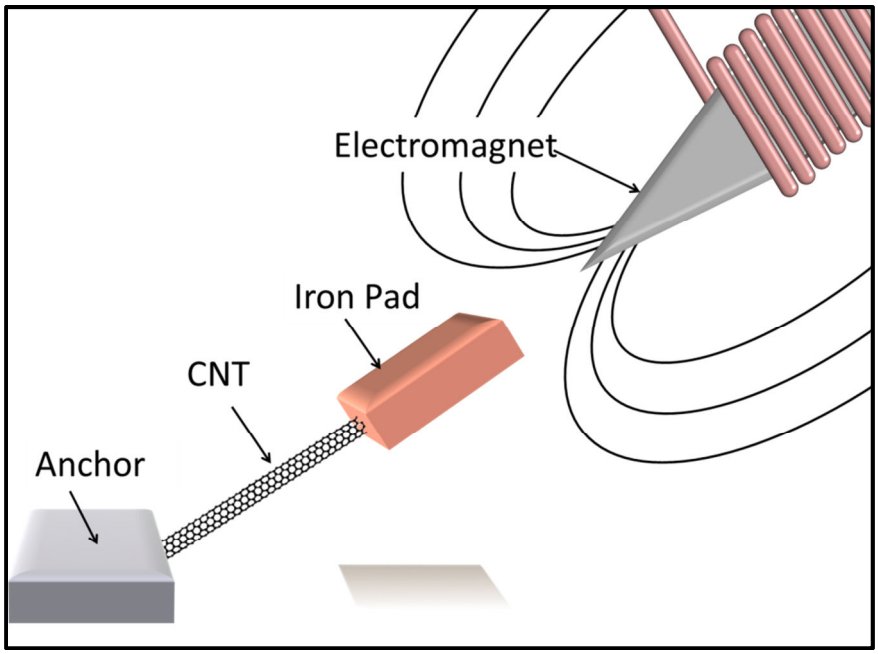

Figure 1.2 Conceptual image of magnetic tweezer experiment that will be described in Chapters 6-9. Here the NT is tethered and its free end is attached to a magnetic iron pad. Forces are exerted on the NT with an electromagnet.

An experiment of the second type is shown in Figure 1.2. Here, magnetic tweezers (a technique developed to study single biological molecules) are used to measure the bending stiffness and force response of a single carbon nanotube. These experiments, discussed later in

this thesis, are the first of their kind, and they give us both information about the nanotube but also are first steps toward creating the kinds of biological probes discussed above.

This chapter serves as an introduction to carbon nanotubes, emphasizing the properties that make them an ideal material for probing biological systems at the nanoscale. We will first look at mechanical properties and compare them to other molecules of similar sizes and shapes. We will then look at the electrical properties by introducing the CNT-field-effect-transistor and its sensing capabilities. We also look at the interesting optical properties of CNTs and show how we can use these to image the NT in unique ways while in biologically relevant environments. We will then show motivational work that shows that CNTs interact will cells in unique ways as well as prior work that has already been conducted with NT probes. We will conclude with a summary and outline of the chapters to follow.

(Note: throughout this thesis we will use NT, CNT, and SWNT interchangeably to all refer to single-wall carbon nanotubes. In the rare instances when multi-walled carbon nanotubes are discussed they will be referred to explicitly as such.)

1.2 Atomic Description of Single Wall CNT

Single-wall carbon nanotubes can be simply modeled as a tightly rolled up graphene sheet that has the form of a cylinder with a radius on the order of 0.3-2.0 nm. A graphene sheet is comprised solely of sp^2 hybridized carbon atoms in a hexagonal structured lattice, as can be seen in Figure 1.3(a). The NT can be rolled up along any number of axes, where the chiral index (n, m) describes the multiple of the basis unit vector pair $(\hat{\boldsymbol{a}}, \hat{\boldsymbol{b}})$ that describes the NT lattice. The chiral vector is defined as:

$$\overrightarrow{\boldsymbol{C_h}} = n\hat{\boldsymbol{a}} + m\hat{\boldsymbol{b}} \tag{1.1}$$

This uniquely describes the geometry of the carbon atoms with respect to the NT axis, but also, uniquely determines the varying electrical and optical properties of CNTs

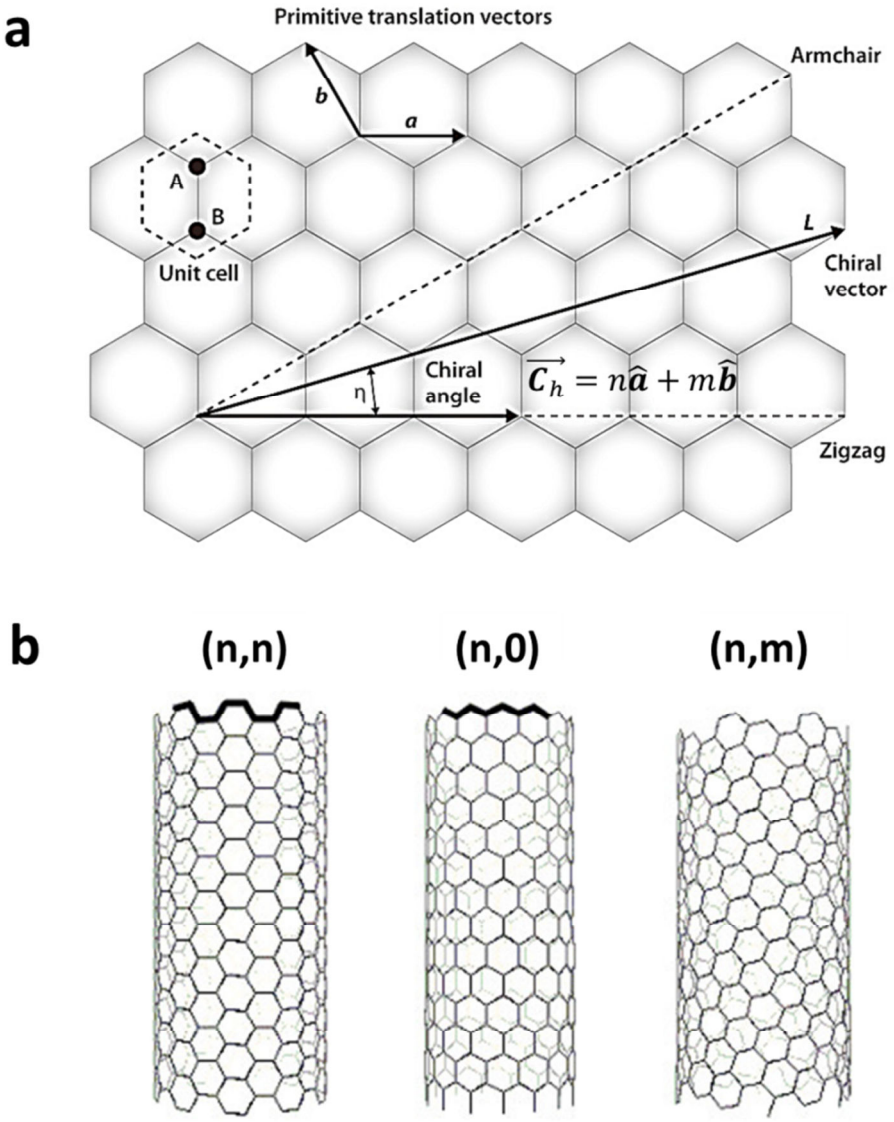

Figure 1.3 Carbon nanotube chirality. Single wall CNTs are simply rolled up sheets of graphene. Electrical and optical properties of CNTs are largely chirality dominated. Figure (a) is from Reference (1) (b) shows three different geometries of CNTs.. The NT labeled (n,n) is an "armchair" NT. The indices (n,0) represents a "zigzag" NT, and the indices (n,m) indicate a chiral NT.

Arm-chair and zigzag are two specific configurations where the chiral vectors are (n, n) and $(n, 0)$ respectively. The NT can also take any other configuration, (n, m) so long as the NT radius remains a reasonable dimension ($r < 2\ nm$). In Figure 1.3(b) armchair, zigzag, and chiral

NTs are illustrated. In particular we note that armchair nanotubes are metallic and zigzag and chiral NTs can be either semiconducting or metallic depending on the (n, m) vector identification.

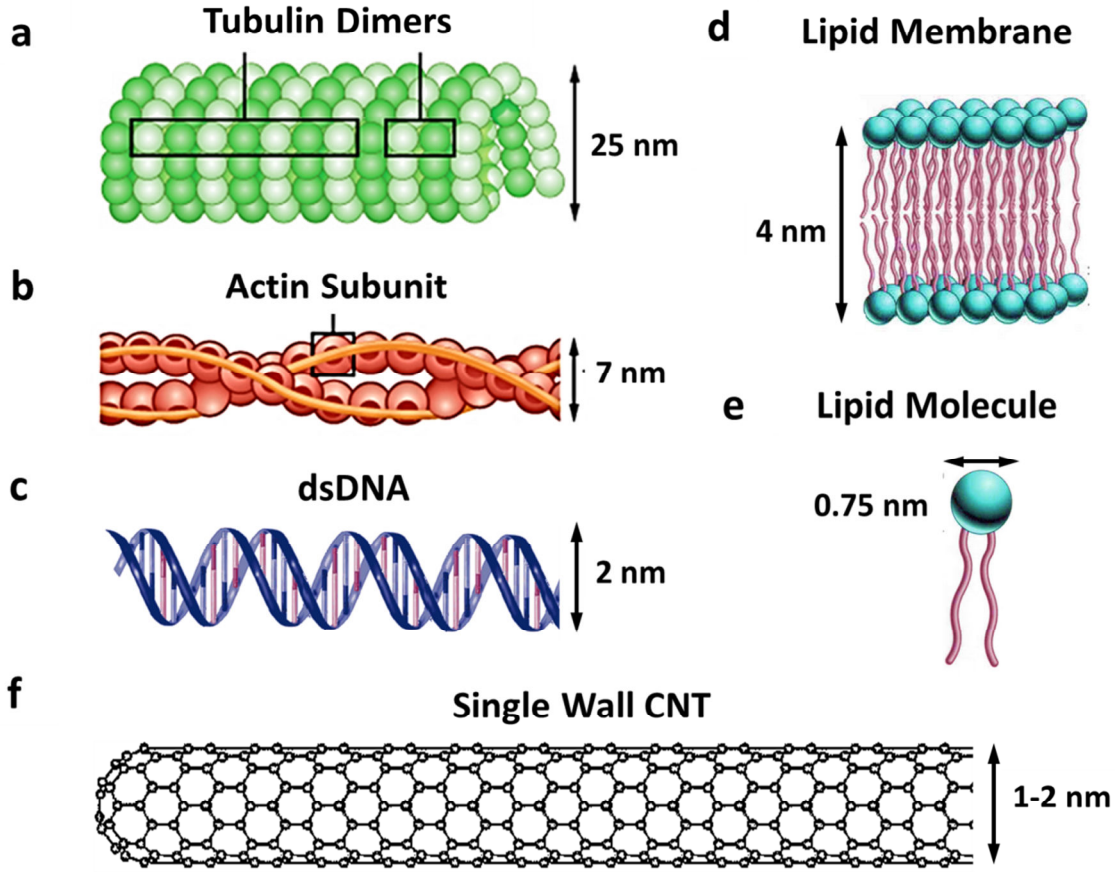

Figure 1.4 Size scales of polymer molecules in cellular studies. Carbon nanotubes are smaller than most linear biomolecules, such as microtubules and actin filaments as seen in (a,b). Figures (a,b) are from Reference (2). Single wall CNTs have a diameter on the same size scale as an extended length of double stranded DNA(c,f). The cross sectional area of a SW-CNT is on the order of area taken up by one individual membrane phospholipid molecule, which has a packing density of $(0.75\,nm)^2/lipid$ as seen in (e). The mechanical properties of CNT are vastly different than those of any other linear molecule. Refer to Section 1.3 for numerical comparisons of the physical properties.

1.3 Mechanical Properties and Relative Size Scales

Single wall NTs have a large Young's modulus(3) $E \approx 1\,TPa$ which gives the NT unparalleled strength when compared to any other material. Additionally a SWNT has a diameter on the order of only 0.5-2.0 nm and routinely can be grown 100's of microns in length, making for a slender hollow molecular tube with a diameter to length aspect ratio that spans impressive 4-5 orders of magnitude.

Looking at Figure 1.4 we see other linear biopolymers and their size scale with respect to that of SWNTs. To compare the properties of CNTs with other linear and tubular molecules we use the persistence length which is the length scale over which molecules bend significantly due to thermal fluctuations—a higher persistence length indicating a more rigid molecule. Double stranded DNA molecules with their rigid backbone have a persistence length of 50 nm, while actin filaments (largely responsible for cell migration and motility), are known to have a persistence length on the order of 15 μm for their larger 7 nm diameter. Meanwhile a 2 nm diameter CNT has a remarkable persistence length of 270 μm.

Furthermore, we see in Figure 1.4(d-e) another illustration that SWNTs are on the size scale of the biological membranes and membrane proteins we would like to investigate. This image shows the NT diameter to be less that the cell membrane thickness and its cross sectional area is on the same size scale of the lipid molecules and proteins that make up the cell membrane, making them an ideal tool for studies of truly single molecule interactions.

We note that devices with features as small as the 1 nm diameter of our NT cannot be realized by standard lithography methods or by growing nanowires from other materials. Nanowires are on the order of 10's to 100's of nanometers in diameter, a size scale that has been shown to be damaging in cell membrane penetration studies and would not be suitable size for truly single molecule experiments we aim to conduct. The intrinsic size scale of the single wall CNT makes them a truly unique molecular scale instrument.

1.4 Single Wall CNT Field Effect Transistor as a Sensor

Even though the NT is just the size of a strand of DNA, it is an electronically functional material. A metallic CNT behaves as an Ohmic wire, while a semiconducting CNT has current voltage characteristics that are able to be modulated by changing the electrostatics of the NT environment, making them useful as molecular-scale sensors.

. We refer to the device geometry in Figure 1.5(a) which shows a semiconducting NT contacted by a source and drain electrode which have a potential across them V_{SD}. We see the device in an electrolyte solution with a gate electrode directly contacting the solution which changes the electrostatic potential around the NT. Figure 1.5(b) shows the conductance as a function of gate voltage of a typical p-type semiconducting NT device. The curves in Figure 1.5(c) illustrate the electronic band structure of the NT as a function of position along the NT for three values of gate potential. These three regions can be seen as the red circles in Figure 1.5(b) and correspond to potentials at which the NT is in an on or an off state. Carbon nanotubes FETs in solutions have a high transconductance, which means that it has a large electrical response for small changes in its electrostatic environment. This feature speaks the electronic sensitivity of the device and the characteristic that makes a CNT-FET an ideal electronic sensor(4).

The exact mechanism of CNT-FET sensing in solutions is reviewed with great detail in (5). We proceed here by way of example, referring to Figure 1.6(a) which illustrates a FET being used as a detector in a cell sensing experiment. These results are from data that we took early on in our cell experiments and is illustrative of the CNT-FET detection scheme. (Subsequent to our work similar findings were published in Reference (6).)

Here we see a similar device to the FET in Figure 1.5, however we note the presence of a trench under the cell. By having a trench under the NT the cell was able to be pushed into direct contact with the NT.

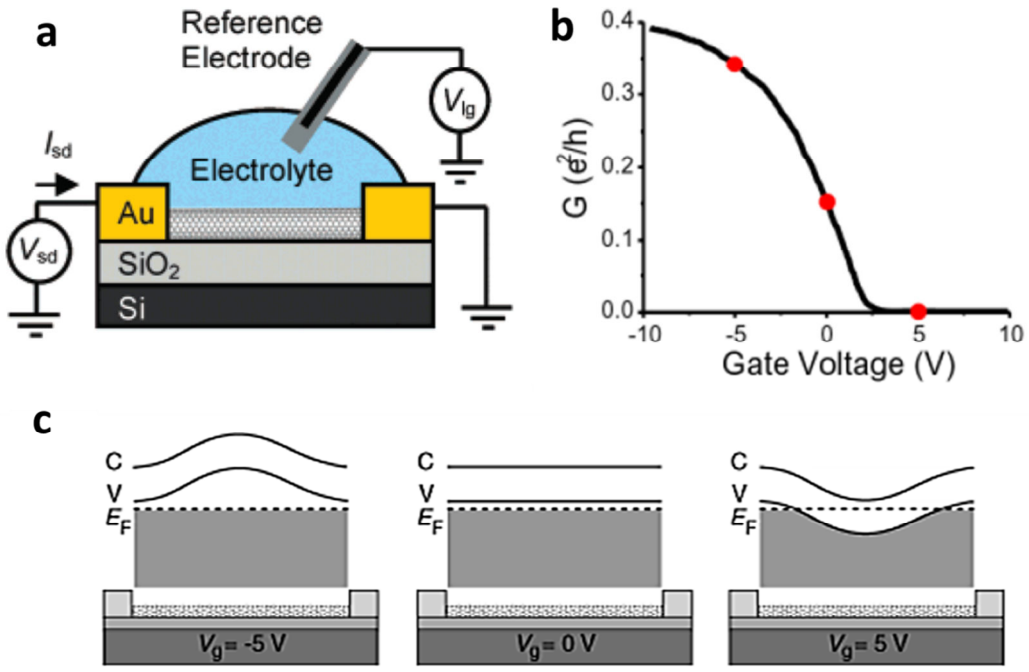

Figure 1.5 Electrolyte gated SWNT field effect transistor. (a) Device schematic of semiconducting SWNT on silicon/silicon-dioxide substrate with electrical source drain contacts which is gated via a salt solution. (b) conductance vs. gate voltage for a typical semiconducting NT device. The inset shows the band structure of a p-type semiconducting NT in contact with a gold electrical contact. (c) Nanotube band diagram for different gate voltages as a function of position along the nanotube axis. At Vg = 0, the Fermi level lies below the valence band edge due to the work function of the metal contacts and the NT is conducting. Changing the gate voltage in either direction bends these bands. In this diagram from reference (7) the band structure At Vg = −5 V, the Fermi level is deeper in the valence band, allowing higher conduction. .At Vg = 5 V, the Fermi level lies in the band gap, turning the transistor off.

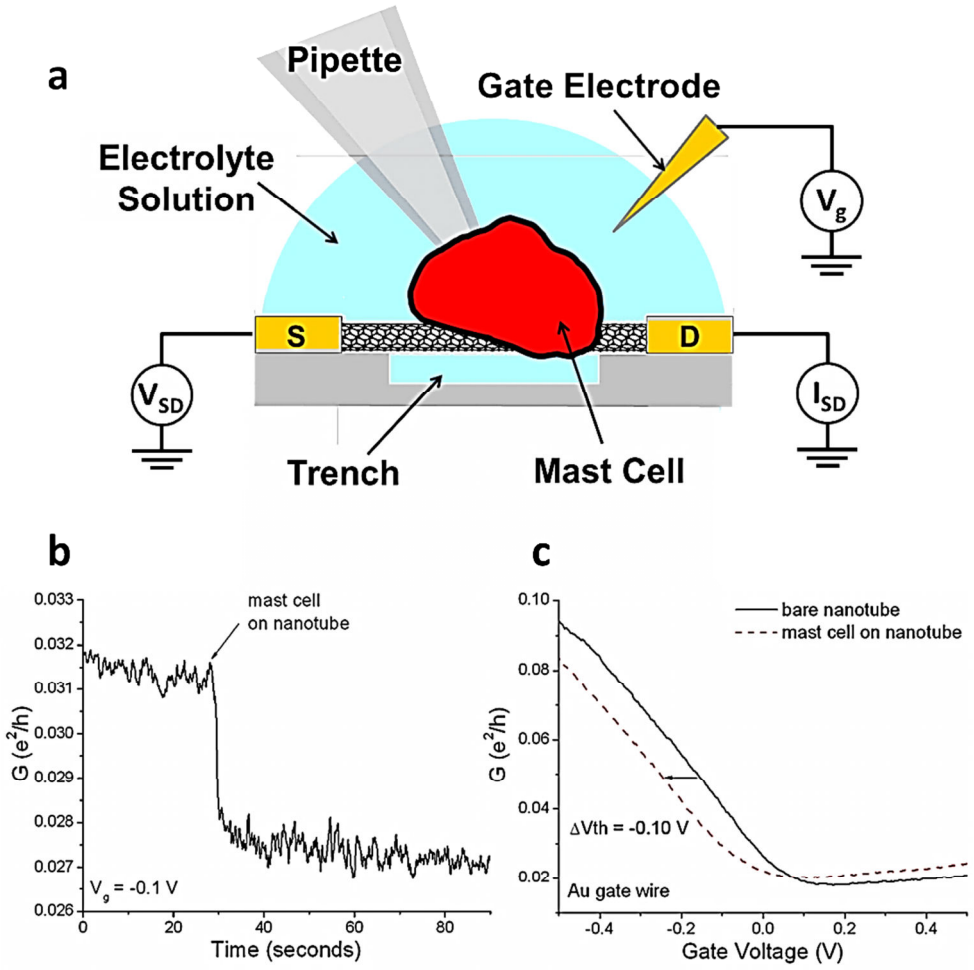

Figure 1.6 Liquid gated CNT field effect transistor in a cell sensing experiment. (a) Typical SWNT-FET device schematic. A CNT is wired between a source and drain electrode and the conductance is varied with a gate electrode setting the potential of the fluid environment. We note the NT is suspended over a trench for increased sensing area and device sensitivity. (b) Nanotube response to a cell placed in contact with it. A decrease in NT conductance can be seen. (c) Conductance vs. gate voltage before the cell was put on the NT (black), and after the NT-Cell was in contact (red). We see a shift is the threshold voltage of -0.10 Volts. The data shown here was obtained by the author with Lisa Larrimore in our early work with cell sensing experiments.

In figures 1.5(b) we see a time trace of the conductance of the NT before, during and after a cell has been placed into contact with the NT. We see that when the cell interacts with the NT there is a resultant drop in conductance. This is how we can tell the NT senses the cell. Additionally, the device conductance vs. gate voltage curves both before and after the cell

interactions are shifted with respect to each other, as seen in Figure 1.6(c), as the dashed and solid lines indicate, which is in response to local gating effects due to the cell interaction.

In addition to cells, this type of CNT-FET detection scheme has been used to sense the presence of other analytes such as lipid membranes(8), DNA(9), proteins(10), and redox molecules(11), just to name a small segment of the experiments reviewed in reference(12). In general the detection scheme is the same: An analyte is brought into contact with a NT. A change of conductance can be seen when the NT detects the analyte. There is a subsequent change in the conductance vs. gate voltage curves presumably due to a local gating effect.

We see that electrically contacted CNTs can be used as sensors to reveal changes in their environment. Additionally the geometry of a CNT wired between two electrodes also allows us to utilize other semiconducting properties of the NT, such as photovoltaic capabilities, which we now explore.

1.5 Carbon Nanotube Photocurrent: Imaging the NT

Having established how semiconducting CNTs can be wired into transistors, we now illustrate how we use the photovoltaic properties of CNTs as a means of observing their location when in solution. We provide here an overview of the technique as we utilize it; an extended discussion of the photovoltaic properties of NTs can be found in references (13)(14)(15).

In Figure 1.7(a) we see a NT device schematic; similar to the illustrated FETs sensors but different in that there is no applied source drain bias. The CNTs are connected to a source and drain electrodes that are both connected to ground. A laser beam is focused to a diffraction-limited spot of ~1μm (depending on the numerical aperture of the objective) and is raster scanned over the electrically contacted CNT. When the laser beam is scanned over a semiconducting CNT it results in excitation of electrons to the conduction band. A schematic illustration of an example CNT band structure can be seen in Figure 1.7(b). The bending in the

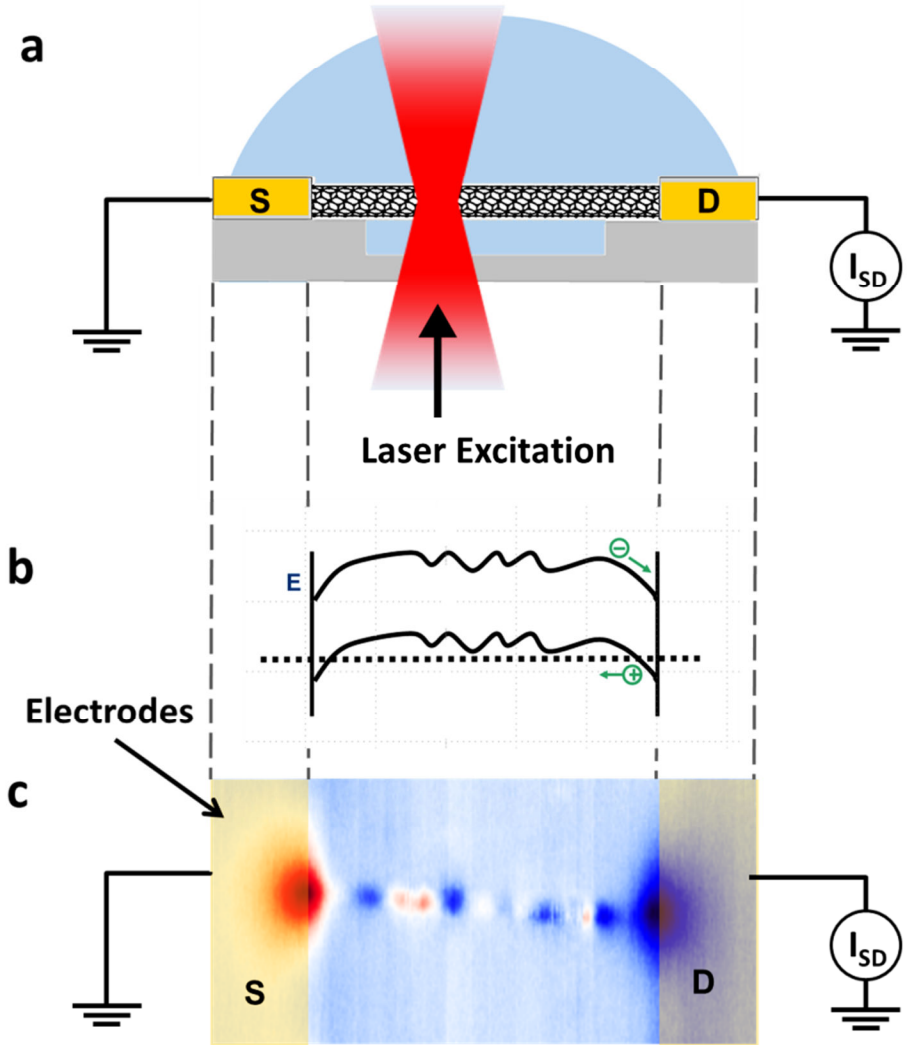

Figure 1.7 Photocurrent of a SWCNT. (a) Measurement schematic—A laser beam is raster scanned across the NT device region. The source and drain electrode are both connected to ground. (b) Schematic of an arbitrary SWNT band structure. Imperfections in the lattice cause a modulation in the band structure that sweep the charge carrier to the electrodes. (c) Photocurrent map showing NT position as a function of position scanned. Red indicates positive current and blue indicates negative current. The PC signal is largest at the contacts. This NT illustrates a device that we further used in cell experiments. The PC signal was generated using a 780 nm wavelength, 10 mW laser intensity, which produces ~2 nA of current at the contacts.

bands arises presumably from defects in the NT lattice and/or charges in the local electrostatic environment. Thus internal to the NT there are regions of local electric fields in the NT, such as those which arise in a P-N junction. These fields sweep the charges excited by the photons to the electrodes and this current is collected via a current preamplifier on its way to ground. As current is only generated when the laser interacts with the NT, a map of the NT in the image plane can be made, an illustration of which can be seen in Figure 1.7(c). The horizontal NT can be seen as alternating blue and red spots representing the sign of the charges collected where red is holes and blue is electrons. This technique is called photocurrent (PC) microscopy and is a non-invasive way to get a measurement of the positions of NTs. The technique works both in air and in solution. This is important as the NT is too small to be optically resolvable, and traditional high-resolution imaging methods such as SEM are not realizable with samples in liquids.

The NT we show illustrated here was from a device that was used in subsequent cell experiments. It was obtained using a 40X 0.6 numerical aperture air objective and a 10 mW 780 nm excitation laser. The region shown illustrates a 15 micron long segment of a single NT that is bridged over two electrical contacts.

1.6 Single-Wall CNT Photoluminescence Imaging

We have just seen that laser light can induce a current in the NT. Additionally incident laser light can also induce photoluminescence (PL) of the semiconducting CNT, another method of imaging NTs while in solution. We will not use this technique in our work, but discuss it here for completeness. In PL imaging, a photon which is absorbed by the NT can impart enough energy to an electron in the NT to excite it to a higher electronic state. Recombination of the electron from a higher energy band with a hole in a lower energy band will cause an emission of a photon with the energy approximately equal to that of the energy gap (Figure 1.7(a)).

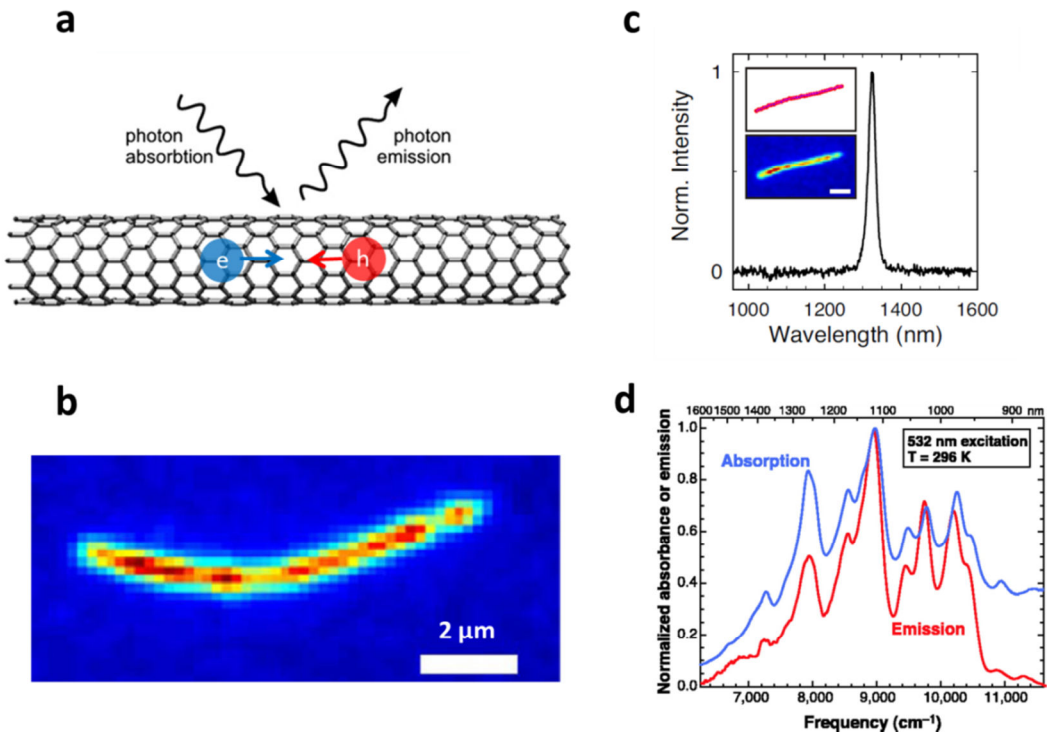

Figure 1.8 Photoluminescence of SWNTs in solution. (a) A schematic of the absorption and emission in a CNT. (b) Infrared image of an individual SWNT in solution(16) (c) We see the emission spectrum is peaked about a single value, as this single NT has only one chirality. (d) Spectra of NTs suspended in solution made up of a distribution of different chirality NTs, revealing themselves as different peaks in the absorption/emission spectra(17).

The photoluminescence of an individual NT is seen in the IR image in Figure 1.7(b). Individual NTs reveal themselves as a single peak in the emission spectra seen in Figure 1.7(c) as the single NT only has one chirality. Figure 1.7(d) shows the emission spectra from an ensemble sample made up of various chirality NTs. We see that there are various absorption peaks. Each chirality NT has a unique band structure, and it therefore has unique colors associated with it. Therefore one can identify the chirality of the NT being investigated just by collecting the light being emitted from it (18). This method has been used to detect the presence of CNTs inside of cells(19), and to determine the persistence lengths of SWNTs while in liquid (16).

In experiments of SWNTs the excitation wavelength is generally on the order of 530-660 nm and the emitted wavelengths are on the order of 800-1600 nm. Therefore this method requires the use of a camera which sees into in the infrared spectrum. The challenge in this technique is that the optical cross section of a NT is low and the emission photon yield is often low, requiring longer acquisition times. However, the strength of this method is that it does not require wiring or staining (such as with fluorophores) as the NT effectively is its own built in fluorophore, and furthermore one that does not bleach with time.

1.7 Motivating Work: CNTs Translocation across Cell Membranes

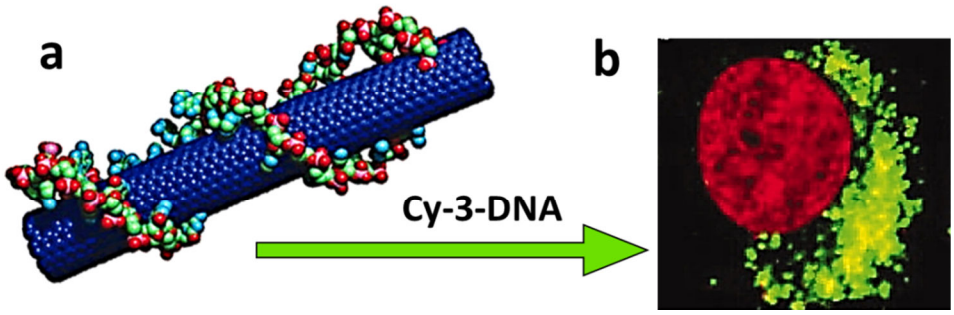

Figure 1.9 Cy3-DNA-SWNT surrounding the cell nucleus. (a) CNTs were functionalized with Cy-3 tagged DNA which fluoresces in the green spectrum. (b) After incubating the functionalized CNTs with cells the 12 hours the NTs can be seen inside the cells via the bright green fluorescence. Images taken from Reference (20)

We now look at some experiments that reveal that biology reacts to the presence of NTs in special ways. This is best illustrated by an example of a cell experiment which can be found in detail in reference (20) and is shown in Figure 1.8(a-b). The basic experiment consists of fluorescent DNA molecules that were attached to short SWNTs. The DNA-CNT conjugate was then added to the media of a cell culture. As a control, the DNA with the fluorophore—but no NT—was incubated with cells prepped in the same manner. After 12 hours of incubation the

cells were imaged. The cells incubated with the NT-DNA conjugates were seen inside of cells, but the cells with just the DNA did not have any fluorescence in them. The conclusion was that cells did not uptake the DNA molecule unless the DNA was attached to a nanotube.

These surprising results indicate that not only can the can NT translocate across the cell membrane, but that it can additionally take additional cargo with it. These results are especially exciting for medical applications in the form of drug delivery and gene therapy and they do not stand alone. Several more experiments of this same sort were conducted using different cell lines, different cargo molecules, and all concluded that somehow CNTs are granted access to a cell's interior(20)(21)(22)(23). This work shows CNTs are routinely up-taken by the cells and can be now be directed to particular organelles and release their cargo.

However all of this is done without a true understanding of the uptake mechanism of the NT into the cell interior. Indeed in the above referenced literature the theorized mechanism is still of active debate, but what is not of debate is that this is an interesting topic indeed for the future of SWNTs in biology and biomedical engineering.

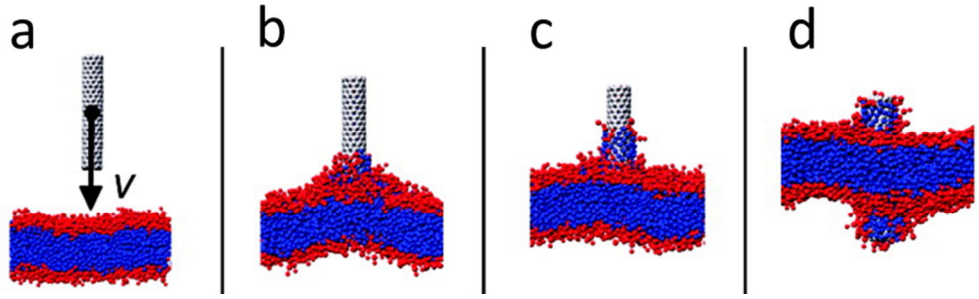

Figure 1.10 Simulation of a SWNT penetrating through a lipid membrane. (a-d) shows a sequential time lapse of a NT passing through the membrane at a fixed velocity. The simulation showed the NT was first pulled into the hydrophobic (blue) region of the membrane. The polar lipid headgroups are shown in red. Image from (21)

It is suggested by simulations that the NT may even be pulled, at least half way, across the cell membrane(22)(21), lowering the high energy hydrophobic surface of the CNT by coating it with lipid membrane molecules(23). This is illustrated in Figure 1.10(a-b). The high curvature of

this membrane response is undesirable, however, and the membrane relaxes, pulling the NT into the membrane interior as it does so as seen in Figure 1.10(c). Additional force is required however to pass through the opposing side of the membrane as in Figure 1.10(d). Simulations show that it takes a SWNT on the order of 100 pNs of force to penetrate a lipid membrane depending on NT diameter.

It would be of great interest to understand the energetics of a CNT penetrating a cell exterior, or experiment on probing a more simplistic model membrane system. In particular it would be of high scientific impact to answer the question (from physical principles): *How does a NT translocate across a cell membrane?* The tools developed in this thesis may make possible such measurements.

1.8 Historical Work: Implementing CNTs as Probes

The idea of wielding a CNT as a probe is not new. Early exploration of the mechanics of NTs drove the field to find a way of studying these properties off the substrate. These studies used the geometry of a CNTs implemented NT attached to the ends of AFM tips. We refer the reader to the various studies for further details(24)(25)(26)(27). Here we summarize some key results of CNT- AFM tip experiments used for cell experiments.

In Figure 1.11(a) we see images from published results which illustrate a multi-walled CNT attached to an AFM tip. In general the SWNT bundles or fortified multi-walled NTs have been welded to AFM tip one by one using the scanning electron beam carbon deposition that is a byproduct of such electron imaging experiments as the welding material. As illustration of the applicability of such a scheme one group(24) used such a CNT-AFM tip to penetrate a cell membrane, as can be seen in Figure 1.11(b). Once inside the cytoplasm the cargo molecule was cleaved by an enzyme native to the cytosol. When the NT is retracted the fluorescently tagged cargo molecule is observed to remain in the cell. An example of a force distance curve in a cell penetration experiment is shown in Figure 1.11(c).

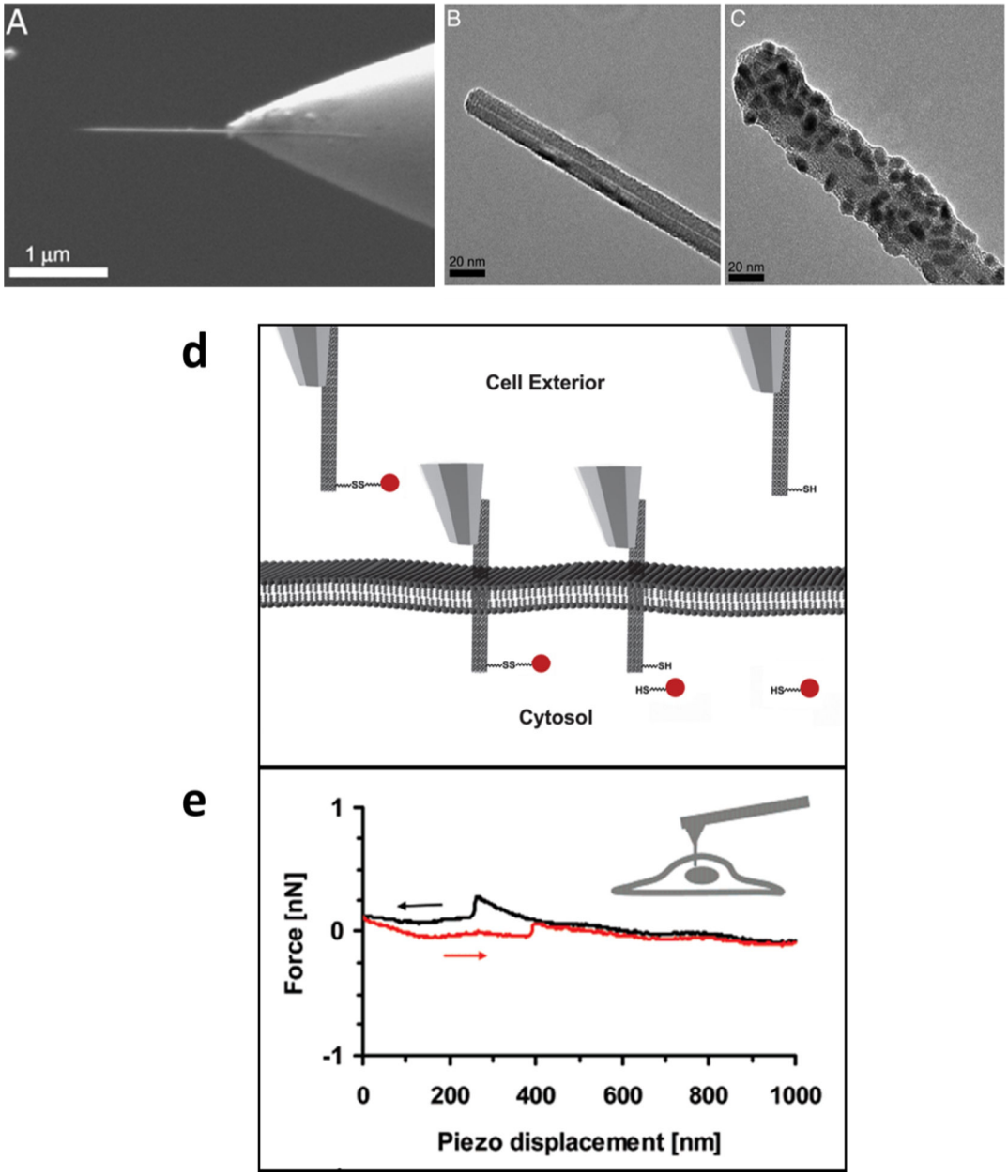

Figure 1.11 Atomic force microscopy tip with attached multiwall CNT at its tip. (a) SEM images of a multiwall NT fused to a AFM tip. (b) Bare MWNT tip 20 nm diameter. (c) Functionalized MWNT tip ~ 40 nm diameter. (d) Experiment where a MWNT-AFM tip was used to penetrate a cell and deliver molecules to the cell interior. (e) Force displacement curve showing the penetration of a cell and the subsequent retraction of the NT probe from the cell. Images taken from Reference (24)

These are exciting demonstrations of the types of control we would like over the forces acting on a NT. We note that these cell penetration experiments differ from what we propose in that they did not employ individual single wall carbon nanotubes instead using CNT ropes and multi-walled nanotubes that were further fortified by metal deposition. It was noted that the large diameter of the probe indented the membrane before penetration. However these proof-of-concept experiments remain important as they are seen as the beginning of the road where we get a grasp on manipulating CNTs.

One thing is clear—we will want to get a more facile method to manufacture CNT devices in parallel other than the one at a time experiments demonstrated in these ambitious studies. What we need is an easier way to manufacture such needle-like CNT probes in a manner that allows high yield and facile implementation in solutions.

1.9 Summary and Outline of Thesis

We now understand the properties of the SWNT that we are looking to harness as well as the motivation and goal of this thesis. Chapter 2 will provide for us the mathematical framework which describes the various mechanical motions of the NT in terms of continuum mechanics. In Chapter 3 we will learn about the ways to grow dense arrays of highly aligned NTs that bring with them the promise of making many devices in parallel. Chapter 4 begins our biological investigations, where we look at the interaction of NTs with living cells via confocal, photocurrent, and SEM microscopy which pieces together a picture of the fascinating ways that cells interact with NTs. These experiments left us wanting for more quantifiable results solutions. We begin our journey toward a probe geometry by a proof of concept cantilever experiment in Chapter 5, where we show that aligned and transferred NTs can be used to make arrays of NTs that extend rigidly over an open trenches patterned to various lengths.

Chapters 5-9 are dedicated to a class of experiments where we use single-molecule techniques to probe individual nanotubes. Chapter 5 starts with a description of class of experiments long

used by the biophysical community for single molecule studies of long polymers like DNA via methods such as optical and magnetic trapping. We learn the operating theory behind these experiments and outline how data acquired by these methods is analyzed. In chapters 7, 8, and 9 our SWNT becomes the studied molecule of interest. We study the NT in and out of externally applied magnetic fields that can manipulate the NT in various ways, as we will see. In Chapter 10 we conclude this thesis with a discussion of future experiments that would have high impact in our understanding of CNT mechanics. Additionally we propose a new class of direct force measurements between biomolecules and CNTs that would make possible the measurement of single molecule bio-interactions in an entirely new manner.

.

Chapter 2

Mechanics of Single-Wall Carbon Nanotubes

2.1 Introduction

Remarkably, classical beam mechanics theory derived centuries ago has been demonstrated to well describe the mechanical properties and mechanical behavior of CNTs(27). The NT can not only be represented by this model, it is apparent from experiment that the NT actually behaves as a beam, even at its atomic scale(28). Historically modeling the NT system in this way gives remarkably accurate representation of the energetics and behavior of CNT systems.

This chapter serves to outline the fundamental motions the NT can undergo and energies associated with those deformations. A total review of the subject as applied to SWNT systems can be found in reference (29) as well as (30). Additionally we will look at simulations of NTs undergoing pure bending and pure torsion and see how these two quantities can be linked. The relationships and definitions arrived at in this chapter will be referred to throughout the rest of this thesis.

2.2 The Bending Energy and Displacement

We start by looking at the amount of energy that it takes to purely bend a beam as shown in figure 2.1. Here the beam is fixed at $x = 0$ and the moment *M* is the torque arising from a force acting in the $+y$ direction at the point $x = L$. The curvature is given by the inverse of the bending radius ρ which is also the second derivative of position. This relationship is appropriately named the curvature-moment relation:

$$\frac{1}{\rho} = \frac{M}{EI_2} = \frac{d^2y}{dx^2} \tag{2.1}$$

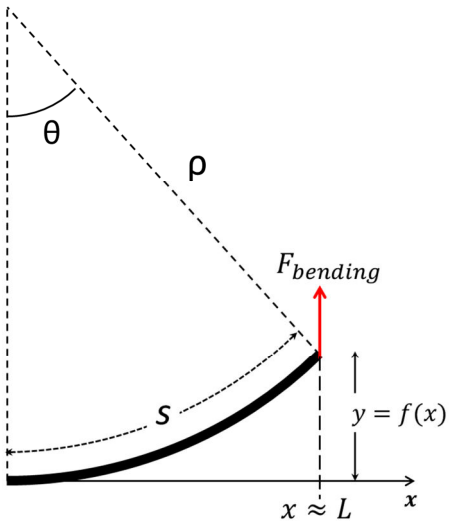

Figure 2.1 Schematic of a beam under pure bending by a point force at its tip. This figure is used in describing variables used in Eqn. (2.1) – (2.10)

E is the Young's modulus and I_2 is the second area moment of inertia of a thin wall cylinder. From Figure 2.4 we see $s = \rho\theta$ and therefore

$$d\theta = \frac{ds}{\rho} \tag{2.2}$$

The strain energy is given by:

$$dU = \left(\frac{M}{2}\right) d\theta = \frac{M}{2\rho} ds \tag{2.3}$$

We insert Eqn. (2.1) into (2.3) and approximating $ds \approx dx$ find for the pure bending energy due to strain

$$U_{bend} = \int_0^L \frac{M^2}{2EI_2} dx \tag{2.4}$$

In our case the torque lever arm and force are perpendicular to each other and the cross product M reduces to its magnitudes:

$$M = \vec{x} \times \vec{F} = |x||F| \tag{2.5}$$

Therefore by Eqn. (2.4) we have for the bending strain

$$U_{bend} = \int_0^L \frac{F^2 x^2}{2EI_2} dx = \frac{F^2}{2EI_2}\left[\frac{x^3}{3}\right]_{x=0}^{x=L} = \frac{F^2 L^3}{6EI_2} \tag{2.6}$$

With the force evaluated at the farthest most point $x = L$. Now the work done to displace the tip a distance *y* with a perpendicular force *F*

$$U_d = \frac{1}{2} Fy \tag{2.7}$$

Equating this displacement energy with the strain energy we find for displacements from equilibrium, *y* as a function of applied force at $x = L$. Meanwhile the strain energy in Eqn. (2.4) can be rewritten from Eqn. (2.1)

$$U_{bend} = \int_0^L \frac{1}{2EI_2}\left(\frac{EI_2}{\rho}\right)^2 dx \tag{2.9}$$

This integral evaluated at *x*=*L* gives the energy cost to bend a NT with curvature 1/ρ over its length L as

$$U_{bend} = \frac{EI_2 L}{2\rho^2} = \frac{Et\pi r^3 L}{2\rho^2} \tag{2.10}$$

Here the approximation $I \approx \pi t r^3$ is valid for thin wall cylinders.

2.3 Euler Buckling Force for single wall CNTs

We now consider axial compressive stresses on the NT along its axis. We want to know how much compressive load the NT can sustain before buckling.

In 1744 Euler applied the calculus of variations specifically to the problem of bending an elastic rod subject to an axial load(31). He derived the critical load under which the rod buckles F_b.

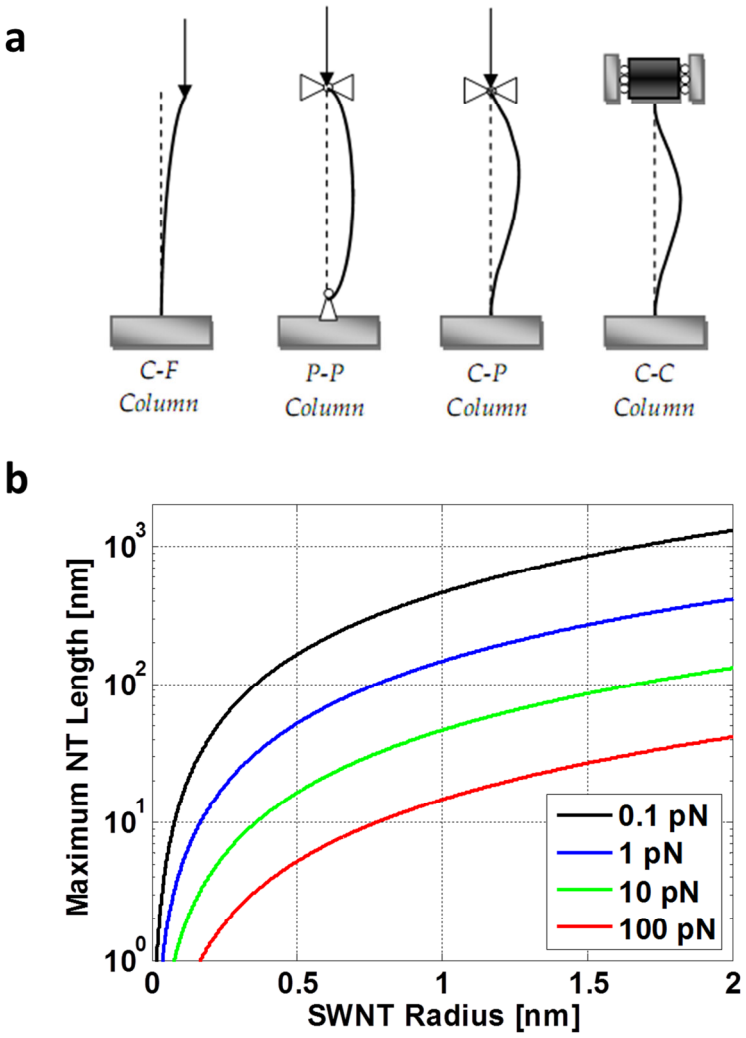

Figure 2.2 Euler Buckling in single-walled CNTs. (a) The mechanism of NT buckling is illustrated here from. Pressure exerted normal to the NT length causes the NT to buckle at the buckling force. (b) Different boundary conditions for buckled geometry as illustrated by reference (32) (c) Graph of maximum SWNT length as a function of radius for four different buckling forces: 0.1 pN, 1 pN, 10 pN and 100 pN.

To attain it ourselves we can simply solve the familiar differential equation given in Eqn. (2.1) for y and use this to solve for the critical axial load that the NT can bear, given the boundary conditions. A load that causes any sideways bending is said to exceed the buckling force. In this case letting the moment $M = Fy$ and $a = F/EI$ we can rewrite Eqn. (2.1):

$$\frac{d^2y}{dx^2} + a^2y = 0 \tag{2.11}$$

This has the solution

$$y(x) = C_1 \sin(ax) + C_2 \cos(ax) \tag{2.12}$$

Satisfying the boundary conditions lets $C_2 = 0$ and we find for the nontrivial solution for $C_1 \sin(a(\alpha L)) = 0$ that $a(\alpha L) = n\pi$. Therefore:

$$\frac{F}{EI} = \left(\frac{n\pi}{\alpha L}\right)^2 \tag{2.13}$$

Here n is a positive integer that represents the mode shape. Using the lowest mode ($n = 1$) we find the buckling force

$$F_b = \frac{\pi^2 EI}{\alpha^2 L_{nt}^2} \tag{2.14}$$

This is a general solution that has a factor α that allows for variation on the boundary conditions which can vary from 0.5-2 depending on how the ends are constrained, as shown in Figure 2.2(b). We model the interaction of the NT with the ridge substrate as a clamped end, and allow the tip at the far end to pivot. This requires $\alpha = 0.69$. We then arrive at the final buckling force for a cantilevered NT probe under compressive axial force

$$F_b \approx \frac{2\pi^3 Etr^3}{L_{nt}^2} \tag{2.15}$$

In Figure 2.2(c) we plot the dependence of the NT length on the NT radius for 4 different buckling forces. We take $E = 1\,TPa$ for a SWNT and $t = 0.34\,nm$. The lines trace out the maximum NT length possible to exert a given force above which the tube will buckle. We see for instance a 1.5 nm radius NT could be made nearly a micron in length to sustain 100 fN axial forces without buckling. Comparatively, an equivalent radius NT would need to be shortened to ~100 nm long to be able to withstand a 10 pN load without buckling.

2.4 The Torsional Energy and Angular Displacements

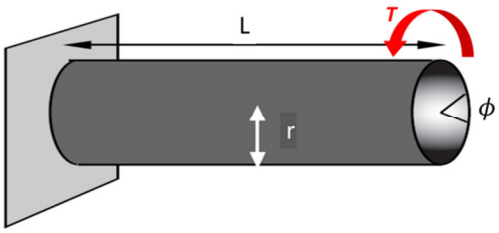

Figure 2.3 Schematic of a beam under pure torsional strain. A torsional force acting at the beam's free end causes an angular displacement, ϕ.

Equivalently to the formulation of Equation 8.4 we can write the energy of torsional strain U_τ as

$$U_\tau = \int_0^L \frac{T^2}{GJ} dx = \frac{T^2 L}{2GJ} \tag{2.16}$$

Here J is the second polar moment of inertia

$$J = \frac{1}{3} C t^3 \tag{2.17}$$

Where C is the perimeter of the cylindrical tube cross sectional region and is simply $C \approx 2\pi r$ where r is the radius of the NT. The torsional modulus G is related to the Young's bending modulus ($E = 1\ TPa$) by way of the dimensionless Poisson's ratio ν ≈ 0.3 where

$$G = \frac{E}{2(1+\nu)} \approx 385\ GPa \tag{2.18}$$

Eqn. 8.11 can also be reformulated usefully in terms of its twist angle $\delta\phi$ in radians

$$U_\tau = \frac{GJ}{2L} (\delta\phi)^2 \tag{2.19}$$

Therefore the purely torsional strain energy stored in the NT is given by

$$U_\tau = \frac{G\pi r t^3}{3L} (\delta\phi)^2 \tag{2.20}$$

2.5 Nanotube Spring Constant

From continuum theory one can find the spring constant for the case of a thin hollow cylindrical cantilevered beam by solving the dynamical problem of a vibrating beam for the resonance frequencies which are related to the NT spring constant by $\omega_0 = \sqrt{k/m}$. The spring constant can be found to be:

$$k_{NT} = \frac{\beta_0^4}{L^3} E I_2 = \frac{\beta_0^4 E t \pi r^3}{L^3} \tag{2.21}$$

The value $\beta_0 = 1.88$ satisfies boundary conditions for a cantilever fixed on one end free to move at the other end, oscillating in its fundamental mode. The spring constant is often related to the thermal motion along δx at the end of a cantilever by the equipartition theorem considering a harmonic restoring potential of the NT by the familiar form:

$$\frac{1}{2} k \langle \delta x^2 \rangle = \frac{1}{2} k_B T \tag{2.22}$$

2.6 Characteristic Length Scales

The persistence length is a measure of the rigidity of long chain polymers, which is another way of viewing our CNT. A longer persistence length indicates a more rigid molecule. Specifically in the case of our single-walled NT cantilevers, it is a measure of the length over which the motion of the tube is correlated and the length scale beyond which the NT loses memory of its orientation(16). This length scale relates the thermal energy to the mechanical properties of the NT:

$$\ell_P = \frac{\kappa}{k_B T} = \frac{EI}{k_B T} = \frac{E t \pi r^3}{k_B T} \tag{2.23}$$

We calculate ℓ_P for a NT with a radius of 1 nm which yields a persistence length of 270 μm. The aspect ratio of persistence length to radius spans 5 orders of magnitude and is quite remarkable to consider. This says that if the NT was the diameter of a climbing rope (~1 cm) that it could extend out nearly a kilometer in length. As another measure of comparison, DNA which also has

a 2nm diameter and a so-called rigid backbone has a persistence length on the order of 50 nm(33), almost 4 orders of magnitude less than the persistence length of SWNTs of same diameter.

Likewise there is a characteristic torsional length given by

$$\ell_\tau = \frac{GJ}{k_B T} = \frac{G}{k_B T}\left(\frac{2}{3}\pi r t^3\right) \tag{2.24}$$

G is the torsional modulus and *J* is the second polar moment of inertia given by Eqns. (2.17) and (2.18). We find $\ell_\tau = 8\ \mu m$ for a 1 nm radius NT. The difference in the characteristic lengths for bending and twisting relate to the respective spring constant of both types of rotation.

2.7 Simulation Results of Bending and Twisting Single-Wall NTs

We now look to the literature for simulations of NT bending and twisting dynamics. In general these are computationally expensive calculations, and the tube dynamics are often calculated for NTs only 6-25 nm long. We have to use some care when using equations derived from such methods to determine their applicability to our micron length scaled devices; however there is much to be learned about NT behavior from these studies.

First, in the case of bending a CNT is described in several places(34)(28)(35)(36) utilizing different molecular simulation platforms. Regardless of the method the results have traits in common: A deformation, proportional to the force in Hooke's law causes the tube to undergo a simple compression on the inner, bending side, and a stretching on the outer side. This can be seen in Figure 2.4(a) Continued strain leads to a collapse of the inside wall of the NT—otherwise known as a buckling event. This event is seen graphically as an abrupt release of energy on the stress strain curve such as seen in 2.4(b). Often simulations show a sequence of such events where each event represents a new morphology of the NT.

In general, at larger bending strains, the single wall NTs are prone to buckling, kink formation and collapse, due to the hollow shell-like structure. Once the NT buckles, it then can pass through a large range of angle without much further force required. This means that the point of a tube

that is buckled can act as a weak spot prone to further mechanical motion. However, below bending angles of 110°, no bonds are broken, in spite of the high value of the strain energy in the exposed area of the kink in Figure 2.4(c). Additionally simulations show these changes are reversible as the tube retains its all-hexagonal structure and returns to its initial straight geometry upon removal of the bending force.

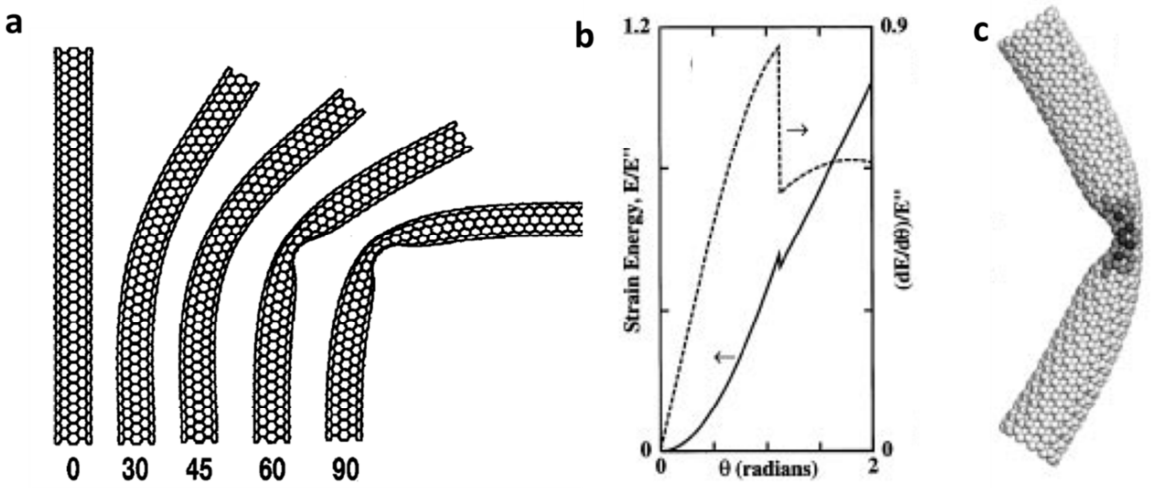

Figure 2.4 Simulations of a SWNT under pure bending stress. (a) The NT can be seen to buckle at 60 °. (b) The buckling of the tube is observed as a singularity on the stress strain curve. (c) Molecular model of buckled CNT with the darker atoms in the kinked region representing higher strain energies. Figures from References (28) and (34).

Now we look at simulations where the NT is under pure torsion(37), as is illustrated in Figure 2.5. All simulation results show that flattening of the tube, or equivalently a collapse of the cross-section can occur due to the torsional load, and this morphology is less energetically demanding than bending or buckling. In the particular case when the NT was constrained at the ends(35) as seem in Figure 2.5(a) and when a critical twist reached $14°/nm$ a transition could be seen in the stress strain curve that relates to the onset of a structural transformation between a twisted state and a flattened helical shape. It is not clear whether the higher energy edges of the collapsed tube induce rigidity to the collapsed NT or not. While this ribbon effect could act as a backbone for the NT structure, It has been shown that AFM measurements of collapsed MWNTs show the

collapsed regions to be softer(38), but these effects include strong van der Waals substrate interactions(39) and it is not clear how the NT will behave off the substrate.

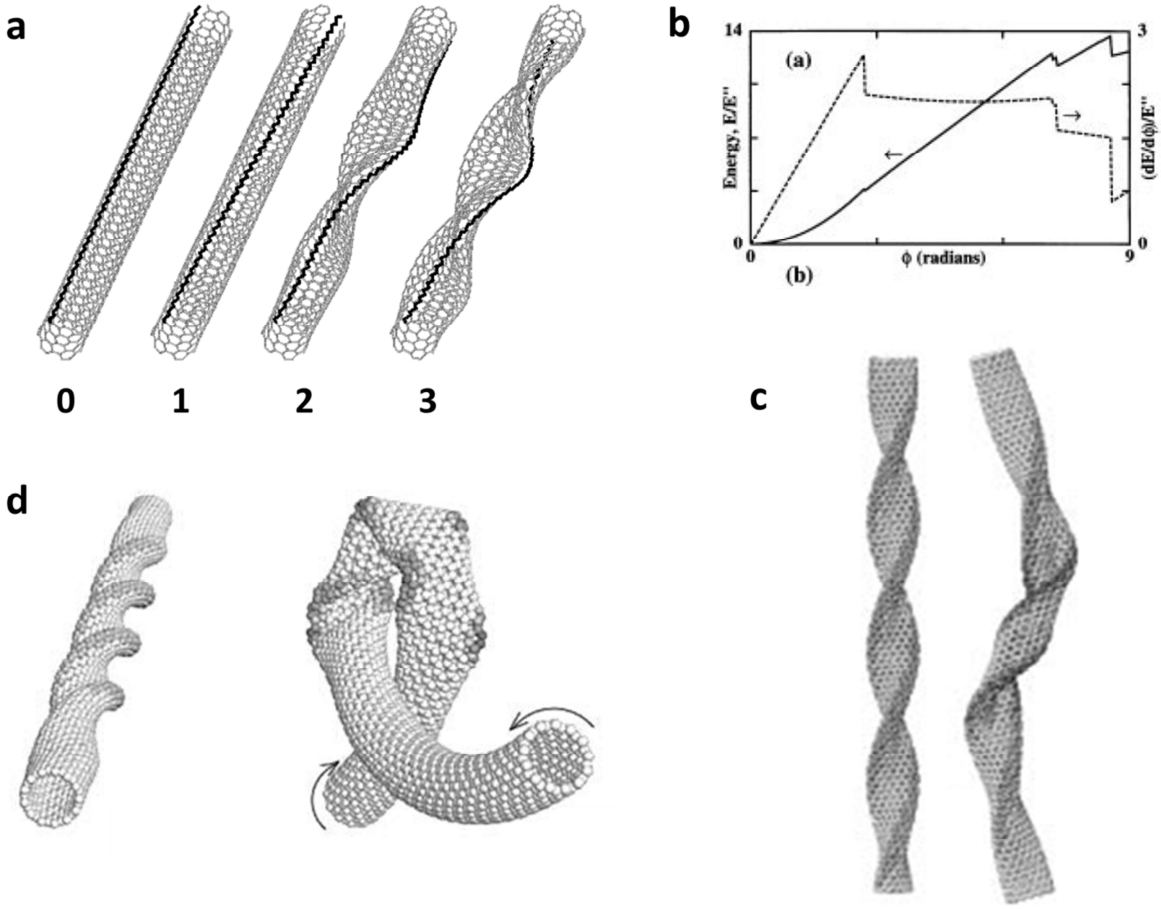

Figure 2.5 Molecular models of showing different equilibrium states of a twisted Single walled CNT. (a) from reference (36) A (6,6) SWNT modeled under axial twist. After ~10°/nm twist (a-2) the NT flattens locally in a collapsed region (a3) shows 25°/nm twist. We note the tube cannot fully flatten as these simulations held the ends of the NTs open. (b and c) from Reference (35) shows a their model of a 1 nm diameter 23 μm long single-walled NT. After 2.7 radians of twist as seen in the graph there is a decrease torsional energy when the cylinder flattens into a straight axis spiral ribbon. At 7.5 radians a sideways buckling occurs with a loss of the straight axis with another drop in energy. (d) A reference with similar results, though they left the ends free to move with respect to each other. In this case twisting after the helical structure is formed causes the tube to convert to a buckled loop structure where twist energy is changed to buckling and bending energy, a simulation of a single wall CNT plectoneme. Images from Ref. (28) and (35)

One reference(35) gave the critical torsional angle for tube collapse to be

$$\phi_c = \left(0.055\, nm^{3/2}\right) L d^{-5/2} \tag{2.25}$$

As a figure of merit this transition occurs for a 2 nm diameter NT 10 μm long at 22.8 radians or about 3.6 rotations about the NT axis. The same theory also predicts that larger diameter NT will collapse from tubular shape to a helical shape at smaller twist angles than narrower diameter NTs.

If twisting is continued after the flattening transition, a sideways buckling occurs in the helical structure with a loss of the straight axis as can be seen in Figure 2.5(c). This transition was found(35) to occur at an angle

$$\phi_b = 2(1+\nu)\pi \tag{2.26}$$

Therefore simulations predict at tube lengths less than a micron torsional collapse is found to occur first, while for tubes longer than a micron they are more prone to sideways buckling under torsion followed by flattening.

In simulations where the ends are free to move(28), helical tube collapse is also seen upon torsion as in Figure 2.5(d). However, continued torsional stress in that case caused a series of buckling events where the NT gave up twist for buckling and bending, forming a CNT plectoneme in the process.

Notably, it is the consensus of these different simulations(35)(40)(34) results that NTs behave in a remarkably resilient way. The single walled NTs sustain extreme strain with no signs of brittleness, plasticity, or atomic rearrangement. Their behavior beyond the linear regime of Hooke's law can be well described by a continuum model. At large deformations an abrupt release of energy is accompanied by a switch into a different morphological geometry. The presence of this 'snap-through' buckling of nanotubes is reversible in simulations when the deforming force is removed and represents a type of shape memory which is very interesting in itself.

2.8 Twist, Writhe, and Linking Number

There is a topological property of closed loop molecules (or equivalently molecules that are held fixed at their endpoints as we have just looked at), that takes into account the way that they accommodate the interplay of torsion and bending into their structure.

The structure of the molecule under different twisting forces can be described by something referred to as the linking number.

$$\mathcal{L}k = \mathcal{W}r + \mathcal{T}w \tag{2.27}$$

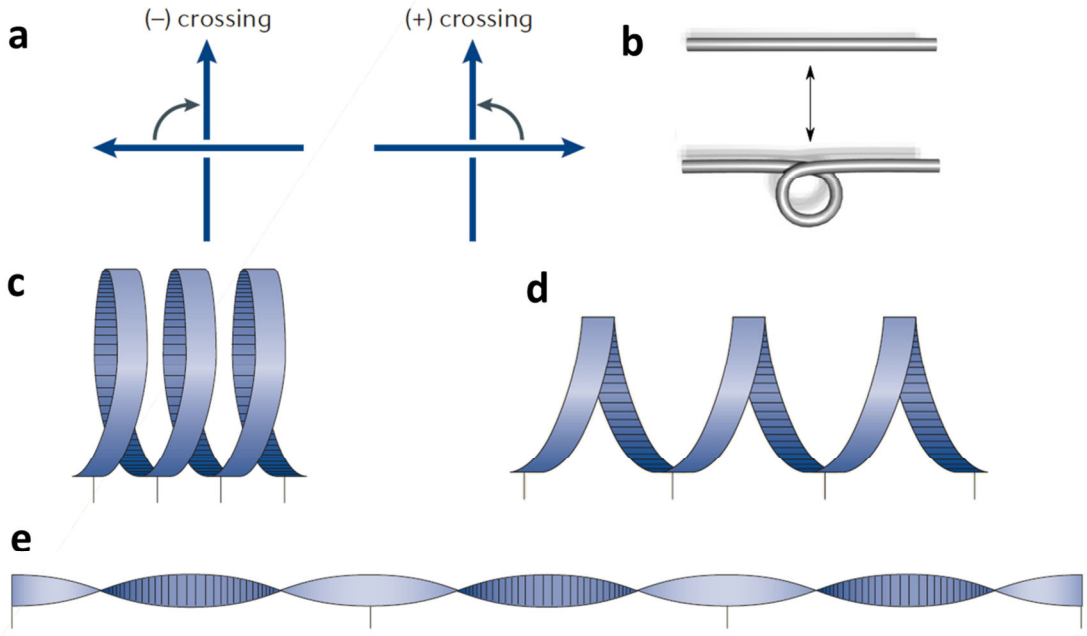

Figure 2.6 Model of polymer with writhe and twist. (a) Shows that the sign of the linking number (number of crossings) depends on the direction of rotation. (b) A linear molecule with linking number changed by 1 by introduction of a single loop. (c-d) Three different states of a molecule modeled as a ribbon with the same linking number, -3. Vertical tick marks are references to the same position of the molecule in all three stages. (c) A coiled state with ~0 twist and a writhe of -3 (d) As the distance between the ends is increased the molecule increases its twist with decreasing writhe, conserving linking number in the process. (e) Fully extended, the writhe (coiling) has been completely converted to twist, (twist = -3, writhe = 0). Image shown in (c-e) are from Reference (41).

Here $\mathcal{W}r$ is the writhe in the molecule described by the number of loops in the molecule over its length. The twist $\mathcal{T}w$ in the molecule is the torsional twist angle distributed equally along the length of the molecule: $\mathcal{T}w = \phi/L$. For a molecule held fixed at both ends linking number is conserved and $\Delta\mathcal{L}k = 0$. This implies the writhe and twist are correlated in that $\Delta\mathcal{W}r = -\Delta\mathcal{T}w$.

An illustration of a molecule under pure writhe which is changed into twist by progressive extension of its ends can be seen in Figure 2.6(c-e). Depending on the forces and the distance between the molecules end points, bending changes to twist and vice versa. Twist can be positive or negative depending on the direction of crossing (the rotational direction). This sign is important when investigating chiral properties of molecules, such as the left handed helix of DNA which manifests itself in experiments by behaving differently at high forces under negative winding than it does for positive winding. This gives us a model to think about the bending and twisting modes occurring in a CNT under torsion, and to how they can be interdependent.

2.9 Conclusion

We have introduced classical beam mechanics theory for the behavior of a thin walled hollow beam clamped at one end with the other end free to move about. This theory is remarkably predictive of observed NT behavior. We have looked at bending, torsional rotation, buckling, and defined language that allows us to go from bean mechanics to molecular theory via the spring constant and the persistence length. Additionally simulations give us an idea of the ways that a NT may absorb bending and torsional stress, as we will investigate more in Chapter 7-9.

While the NT shares many similarities with the classical beams we encounter in our macro scale world, they have a strong distinction. They are tough and resilient in a way that is not observed for other materials. After a buckling event the NT will restore itself back to its original geometry after the force has been released without permanent deformation(27)(35). This is in contrast to many materials that fracture or plastically deform irreversibly upon buckling.

Chapter 3

Aligned Single-Walled NT Growth and Transfer

3.1 Introduction

Since 1998 groups have been able to controllably and reproducibly grow long single-walled carbon nanotubes via catalytic chemical vapor deposition methods (42)(43)(44)(45). However the exact location and orientation of the NTs could not be controlled and device yield depended mostly on the statistics of a NT growing where you wanted and in the direction you desired. Indeed the control of the orientation, position, dimension, structure, and property of SWNTs in the growth process is very important for most of the application of SWNTs(46).

A huge leap in progress was made in 2005 when aligned directional growth of single-walled carbon nanotubes on a-plane sapphire substrates was demonstrated using iron particles as a growth catalyst(47). Soon after in 2006, the Rogers Group demonstrated highly aligned and parallel arrays of CNTs using a similar method on crystalline α-quartz, obtaining higher yield and alignment on the less costly quartz substrates(48)(49). This method was subsequently optimized to produce ultra-high NT density with ultra-long NTs (50). Aligned SWNTs millimeters long are now routinely grown with densities of several to tens of NTs per micron.

In this chapter we will first briefly comment on the mechanisms of growth and alignment for CVD growth on quartz. Then we fully describe the techniques used in this thesis for NT growth and subsequent NT transfer. We discuss the critical points in each step of the process and how we optimize the transfer process depending on the geometry of the device architecture.

Aligned NT growth methods were originally established in the McEuen Lab by Melina Blees. The work on suspended NT transfers was done with Arthur Barnard.

3.2 Aligned Nanotube Growth Theory

The mechanism of CNT growth via CVD methods is a widely studied topic(43)(51). In this method hot gases are flowed over substrates patterned with catalyst nanoparticles, often transition metals such as Fe, Ni and Co. The vapor-liquid-solid mechanism is the method via which carbon nanotubes are produced. A high temperatures (>700°C) the catalytic liquid metal alloy promotes the dissociation of hydrocarbon molecules (vapor) and saturation of carbon atoms in the catalyst metal islands (liquid). The precipitation of carbon (solid) from the saturated metal particles leads to the formation of carbon nanotubes. Hydrogen from the decomposition process and also any carried with the bulk gas phase contributes to the activation and reactivation of the catalytic surface.

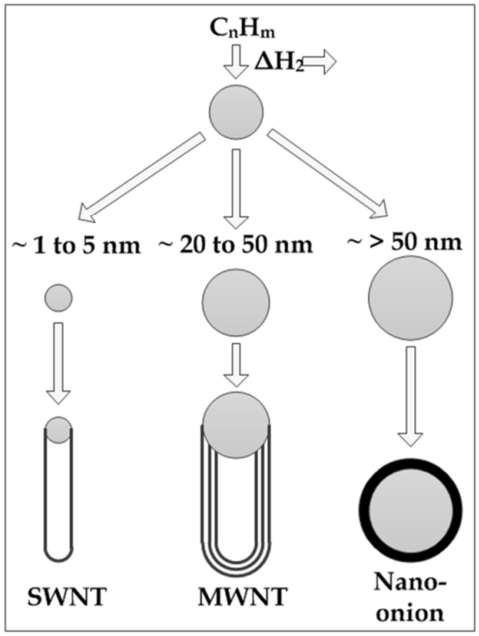

Figure 3.1 Catalyst particle size and CNT growth. The size of the catalyst particle in critical in determining the size and type of NT structures that are grown. We use iron nanoparticles on the order of 1-3 nm and have almost exclusively SWNT growth. Figure from(52)

For the remainder of this chapter we will concentrate on only single wall NT growth on quartz crystalline substrates with Fe catalyst islands < 5 nm. Catalyst particles of this size are known to produce only single walled NTs as shown in Figure 3.1(a). The theorized mechanism of NT growth vary in the literature, but for SWNTs on quartz the accepted mechanism is call "tip growth", where the catalyst particle is pushed along the substrate as the CNT precipitates out from it(50). Meanwhile the highly parallel alignment (< 0.5° deviation) of the nanotubes is due to a surface directed mechanism induced by the crystalline structure of the quartz substrate(48). The carbon shell precipitated on the Fe catalyst particle interacts with the substrate lattice and leads the growth along the direction of crystal alignment. Figure 3.2(a) shows the crystal structure of α-quartz. The square rectangle at the center represents a cut across the y axis misaligned by θ degrees and represents a cut of the wafers that we use in our lab. Figure 3.2(b) shows a schematic of the atomic steps in the cut crystal surface. Evidence suggests the lattice-induced alignment of the NT to the quartz substrate is due to the high surface energy of the atomic steps and edges of the cut quartz(48). From energetics it is reasoned that reactive carbon species would preferentially adsorb and align at these step edge locations(51) thus promoting atomically aligned growth.

3.3 Quartz Substrate Preparation—Catalyst and Anneal

We will now describe the process by which we prepare the quartz for NT growth. These methods are based on procedures used in the Rogers lab(53) and adapted slightly over time to optimize growth for our experimental requirements.

Quartz wafers are easily commercially obtained in standard 100 mm wafer diameters that make them convenient for conventional lithographic patterning. We begin fabrication with a 500 μm thick ST (Stable Temperature) Y-cut quartz substrates (Hoffman Materials). ($\theta = 42° 45"$, Single-side polished.) Growth has been studied by this author on seeded and non-seeded varieties of α-quartz, double sided polished and single sided polished, and for our growth

conditions all performed equivalently yielding similar densities and diameters of NTs. We note the x axis of the crystal runs parallel to the wafer flat, which is perpendicular to the direction of NT growth as shown in Figure 3.2(c).

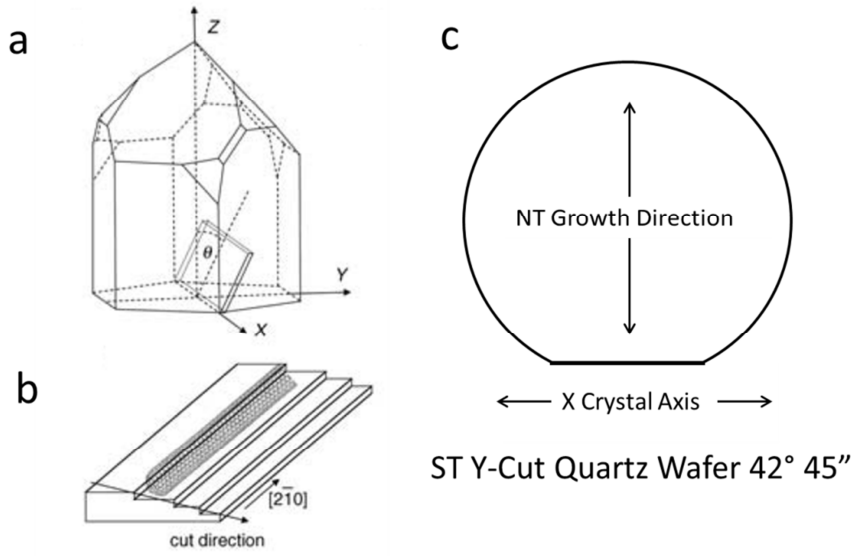

Figure 3.2 Single crystal α-quartz crystal structure. (a) Shows the crystalline axis in right handed α-quartz and the orientation of a piece cut out of this structure at angle θ with respect to the Y crystal axis. (b) The atomic step edges of the crystal cut in this way. The NTs grow preferentially along this edge. (c) A 100 mm Y-cut wafer as ordered from Hoffmann Materials with $\theta = 42° 45"$. The wafer flat runs along the x crystalline axis depicted in (a). NT growth is always perpendicular to this edge. Schematics in (a) and (b) were taken from Reference (52)

We first lithographically pattern stripes into photoresist 5 μm wide and 18mm long perpendicular to the NT growth axis, repeating this row vertically every 50 μm. A 60 second exposure to O_2 plasma etches any residual PR from the catalyst regions. Iron (Fe) is evaporated 2 Angstroms thick at a rate of 0.2 Angstroms/second. It should be understood that the Fe is by no means a 0.2 nm continuous coating over the catalyst regions, but that this number represents a thickness averaged over its area. The Fe coated PR is removed from the chip by sonication in either 55°C Transene1165 or room temperature acetone with the wafer upside down. This is so

the Fe that is lifted off with the PR does not have the opportunity to redeposit on the quartz surface. The wafer is then diced into chips 19.5 mm^2. This dimension allows them to sit nearly in the middle of flow in our 1" diameter quartz growth tube. If smaller than this the chips should be placed on a quartz or ceramic boat to elevate the chips into the central gas flow.

Before NT growth the Fe coated quartz must be properly annealed at high temperatures for three reasons. Firstly α-quartz undergoes a reversible change in crystal structure at 573 °C to form β-quartz. The transformation between α- and β-quartz only involves a comparatively minor rotation of the crystal tetrahedra with respect to one another(54), however, this α to β quartz transition is accompanied by a linear expansion of 0.45%. Therefore one must ramp the temperature of the quartz slowly through this temperature transition. Fast ramping of the temperature can cause the quartz to crack. It has been noted that amount of fracture scales with chip area(55) and we note this to be true in our experiments.

The second reason for annealing is to cause the nucleation of the Fe catalyst into nanoscale islands, necessary to catalyze growth, as was mentioned in section 3.2 Iron must be sparse enough else the nucleated islands are too large for NT growth, or at least SWNT growth. Thirdly, the anneal process is somehow necessary for high alignment of the NTs which we will discuss further.

We anneal our chips at 900°C in a 1" diameter 4 foot long quartz growth tube open to air at both ends. Total anneal process time is 10 hours; this begins with a 1 hour ramp to 520 degrees. Temperature is then ramped slowly from 520°C-620°C going through the α to β transition at 50°C/hour over 2 hours. After the transition temperature has been passed temperature is ramped quickly to 900°C and held there for an additional 6 hours. The furnace is then turned off and allowed to cool slowly back to room temperature over an interval of ~2 hours.

At this point the quartz chip is now fully prepared for NT growth. Interestingly once the chip has been annealed in this manner it does not need to be ramped as slowly through that transition region again. In our experience if the chip does not fracture in the anneal process it won't in further processes. Additionally it has been found that quartz chips annealed even several months

prior would still produce aligned NTs, in contrast to un-annealed chips which do not have high degree of NT alignment. This would imply that the β transition was metastable or otherwise that the annealing served some other role in aligning the growth than just crystal reorganization.

3.4 Nanotube Growth and Results

We now describe our CNT growth process. A schematic of the growth furnace can be seen in Figure 3.3(a). The chip is inserted into the 1" quartz growth tube which is coupled to the gas line at one end and a downstream exhaust line at the other. Methane (CH_4), hydrogen (H_2), and argon (Ar) are all feed gases at different points in the process.

A summary of the growth process is presented here along with a graphical representation of our specific growth steps is seen in Figure 3.3(b). The pre-annealed quartz chip is brought up to 520°C in 30 minutes while in 1 Standard Liter per Minute (SLM) of argon. The α to β transition is passed through in 30 minutes (for a pre-annealed chip). The chip is then brought up to our 875°C growth temperatures. The oxidized iron (oxidized prior in the air anneal) is reduced in pure H_2 for 5 minutes. Methane is then added to the hydrogen at a rate of 1.9 SLM and NT growth begins instantly. Growths stopped after even just 10 seconds of methane flow will already have NTs that span 50 microns. A standard growth involves letting the CH_4 flow for 20 minutes of growth time after which the methane is turned off and the quartz cooled to room temp in 1 SLM argon flow. The chip is not exposed to air until the furnace is below 100°C as this is well below the temperature which oxygen can attack the tubes (~300°C).

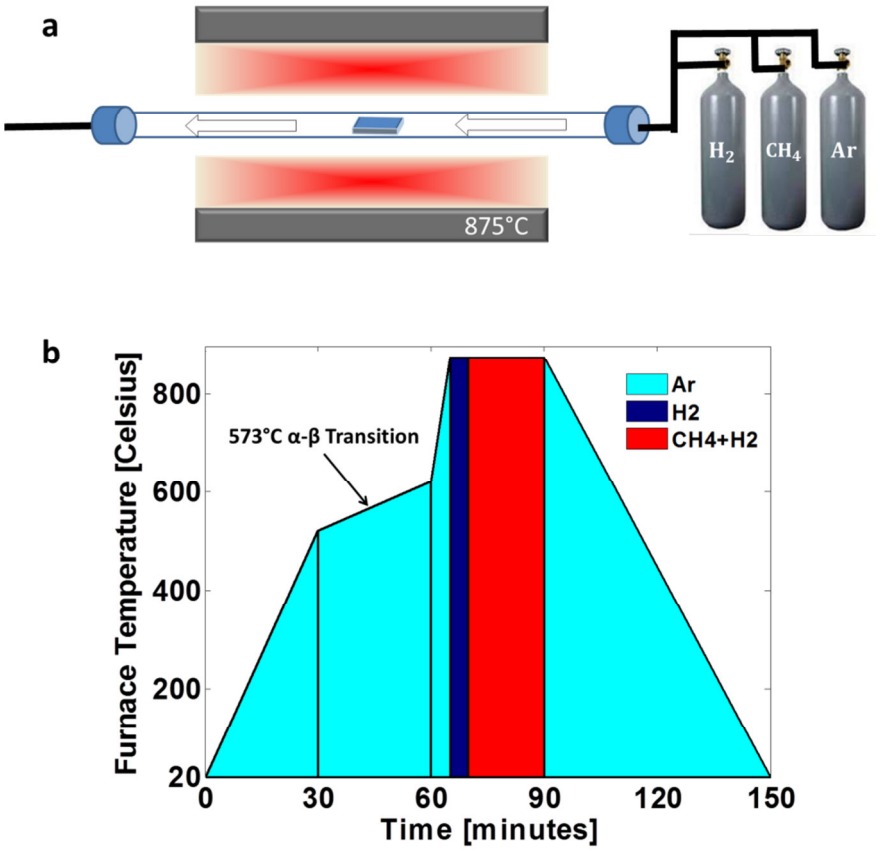

Figure 3.3 Carbon nanotube growth furnace and recipe. (a) A 1" diameter growth tube sits inside a furnace with the 19.5 mm^2 quartz substrate at its center (small square). Flowing a mix of H_2 and CH_4 at 875° over the quartz and iron catalyst results in the growth of highly aligned CNTs. (b) A graph of temperature vs. time for the steps in our standard SWNT growth. Light blue is when only argon was flowing, dark blue is hydrogen only, and red is the growth mixture of methane plus hydrogen.

Results of a typical growth can be seen in the AFM image in Figure 3.4(a). This shows an amplitude image of the AFM date, which is the raw voltage representing the displacement of the AFM tip and a derivative of the height information. Here we see a 10 micron by 30 micron region of NTs that is representative of those used in experiments outlined in this thesis. As shown here we see NT densities of 0.5-3 NTs/μm consistently growing at least the 50 μm distance between catalyst pads. The image in 3.4(b) shows the catalyst region of the same chip.

Though we evaporated only 0.2 nm of material we observe that after annealing and growth the NT catalyst is made up of coagulated islands ranging from 1-5 nm in size. This is not a continuous layer, and many NTs can be seen growing in the catalyzed region, though in a non-oriented manner. The particles that do catalyze growth create NTs that can be seen to find alignment with the substrate within 1 μm of exiting the catalyst region.

Figure 3.4(c) shows a histogram of NT radii as measured off of the height data of image (b)(not shown). This sample shows 0.3 to 1.4 nm radii NTs with an average radius (for this sample) of 0.7 nm. The NTs we have observed with these methods are all single walled as indicated by their diameter and as well as personal communications (Reference Jonathan Alden) from a collaborator who has done extensive TEM imaging on the NTs grown by this recipe. NTs were seen to be up to 4 nm in diameter and all have been observed to be single wall. Our diameter distribution of SWNTs is also consistent with diameter distributions reported from other groups using this method of growth(50)(55).

Figure 3.5 shows SEM images of two growths done using identical methods but Figure 3.5(a) shows growth on an un-annealed quartz substrate while Figure 3.5(b) shows the results of growth on an annealed quartz substrate. We see that the NTs are not aligned when the substrate is not annealed, and that the NTs are highly aligned when the substrate was annealed. This is consistent with observations in prior work(55)(56). The horizontal lines in both images are the catalyst regions and one can see the maze of NT growth that occurs in all directions at the catalyst pad regions.

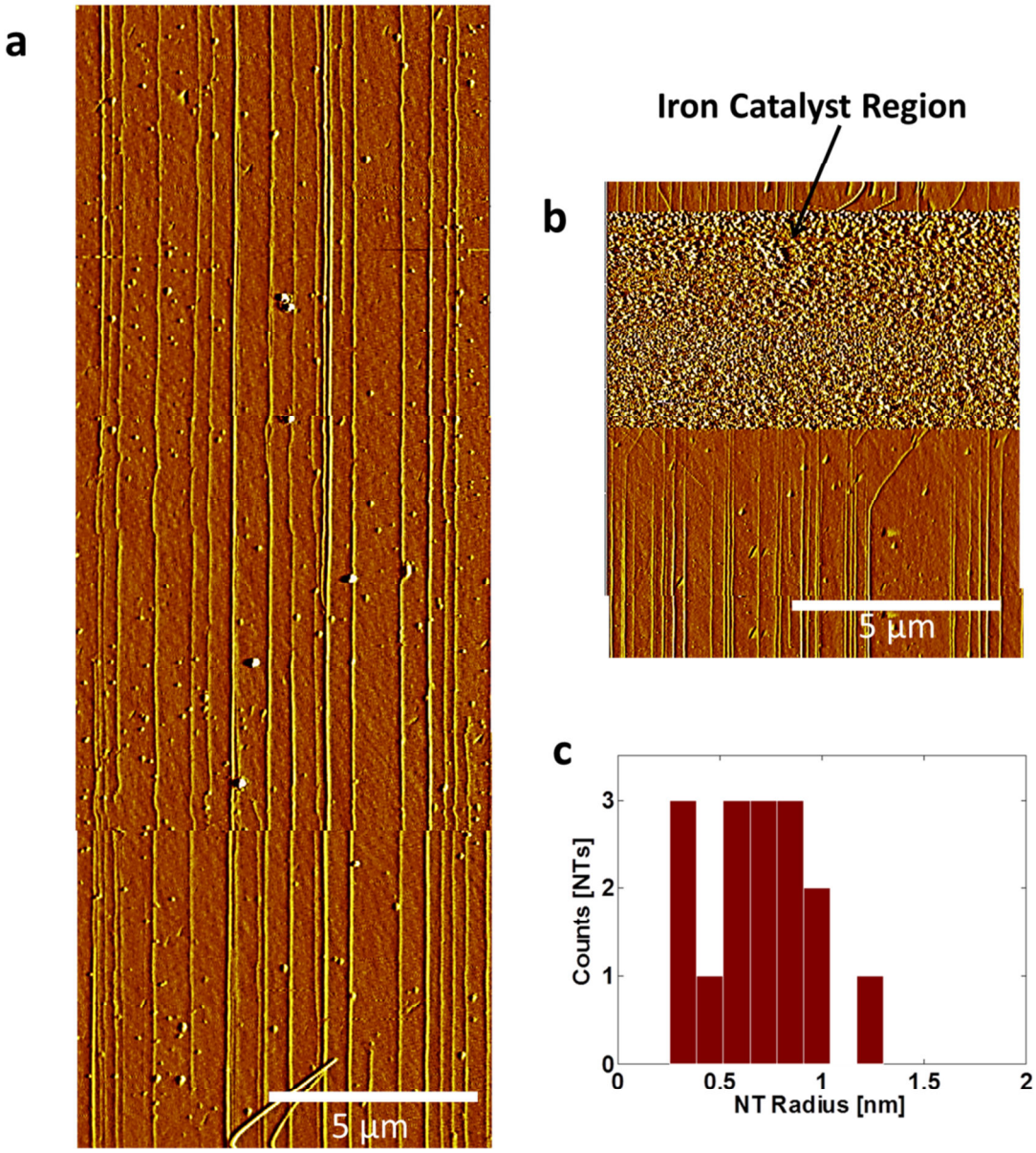

Figure 3.4 AFM of Aligned SWNTs. (a) AFM tapping mode amplitude image. The slow scan direction in these images is top to bottom and the line scan direction is left to right. (b) AFM scan of the Fe catalyst region shows nucleation islands of Fe on nanometer scale. (c) Histogram with the NT diameters as read off the AFM height scan of figure (b). In this particular sample there is a mean NT radius of 0.7nm.

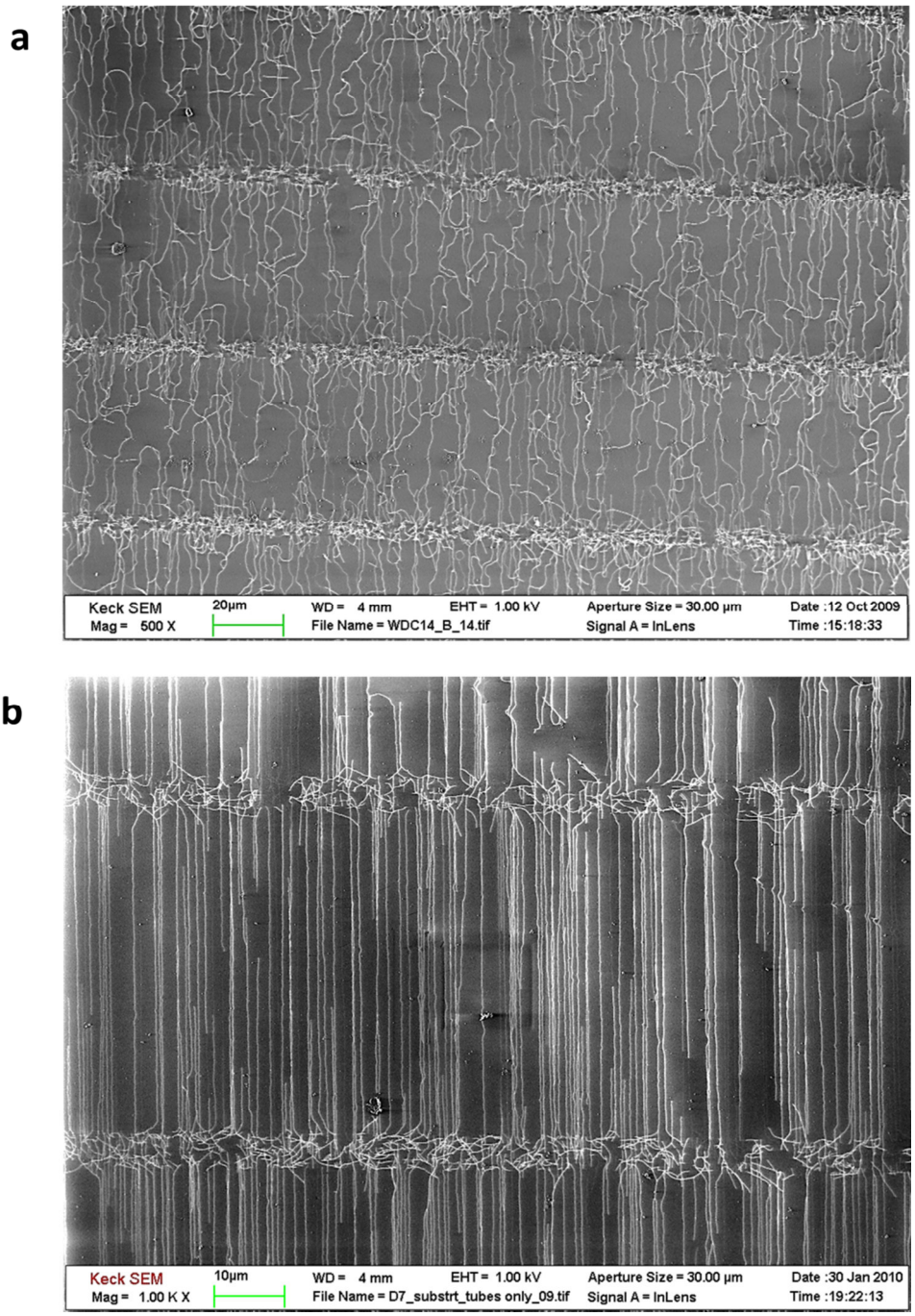

Figure 3.5 SEMs of NT growth. The horizontal lines in all three images are the stripes of Fe catalyst that promote SWNT growth. Distance between horizontal catalyst lines is 50 µm. (a) NT growth on a substrate that was not annealed. The tubes are not aligned well and tubes cross over each other. (b) NT growth on annealed quartz. Alignment of NTs is only attained after quartz is brought through the α-β transition via air annealing.

3.5 Transfer Methods

Integrating aligned NTs into NEMS devices often requires the ability to move the SWNTs from the quartz substrate to a device substrate that is often crystalline silicon or fused silica. It is therefore necessary to develop techniques to transfer the NTs off the quartz onto the receiving substrate of choice. There are a several key considerations – First one needs a transfer medium that is both thick enough that allows the NTs to be manipulated macroscopically (i.e. by tweezers), and rigid enough that it maintains the NT's relative aligned geometry. The material used should bind preferentially to the NTs (and not the quartz) so the NTs can be separated from the quartz substrate. The transfer medium needs to adhere well to the receiving substrate. Lastly, the transfer medium must be able to be removed without damage to the NT or the underlying device. We will see that issues of adhesion and polymer removal are the critical factors in a successful transfer process.

Historically NT transfers have been facilitated a number of ways. One method(57) achieves this transfer by coating the NTs in gold and then polyvinyl alcohol **(**PVA). The transfers in this process were facilitated by moving the NT/gold/PVA conjugate by an elastomer stamp made of Polydimethylsiloxane (PDMS). Another report(58) outlines a similar transfer method using a chrome/gold film and used cross-linked epoxy as the transfer medium. Impressive full wafer scale NT transfers were attained with the use of a gold coating on the NT with thermal release tape as the reinforcing transfer layer. Alternatively, the method of using Poly(methyl methacrylate) (PMMA) as a transfer medium was established with precise transfer results(59).

The techniques and results we now report are protocols arrived at by combining a combination of techniques outlined in the above references with additional modifications that we found were required to get the high yield and cleanliness that our devices required. Three different transfer methods were investigated in our studies. We investigated gold transfers with a PVA mediator layer, and NT/gold transfers with thermal tape. Lastly we describe transfer methods using PMMA.

3.5.1 Gold Transfer Methods

Figure 3.6 outlines the steps of NT transfer facilitated by gold (Au). Gold is a material that is adherent to NTs and which is less adherent to quartz. To pick up the aligned tubes, a 100 nm layer of Au was first deposited on the nanotubes/quartz by electron beam evaporation as shown in Figure 3.6(b). This layer is soft and not able to be manipulated on its own; therefore a polymer intermediate is used to reinforce it.

Liquid PVA solution (prepared by dissolving 100% hydrolyzed PVA into water) is a material that serves as a good transfer medium. A solution of 1% w/v PVA is pipetted on top of the gold surface of the quartz chip as in Figure 3.6(c). About 1μL of solution for every square millimeter of surface provides adequate coverage. The quartz chip with Au and PVA is then baked on a hotplate at 70°C for 20-30 minutes to harden the PVA and then allowed to cool. A sharp razor or X-Acto knife is used to cut the gold and PVA into small ~5mm^2 square regions directly on the quartz chip. Physically lifting and peeling the PVA with tweezers is enough to release the NT/Au/PVA conjugate from the quartz surface as illustrated in figure 3.6(d). This is then placed NT/Au side down onto the receiving substrate. Heating briefly on a 70°C hotplate for 1-2 minutes helps the PVA/NTs to relax down and adhere onto the device surface. The PVA is then dissolved away in 3 85°C water baths to solubilize the PVA in successively cleaner baths of DI. Care is taken so the gold is not disturbed during fluid transfers. After PVA removal the gold still remains on the device surface on top of the NTs. This is further cleaned by an 30 second O_2 plasma RIE etch to remove residual PVA then the Au is etched away in Transene Gold TFA Etchant.

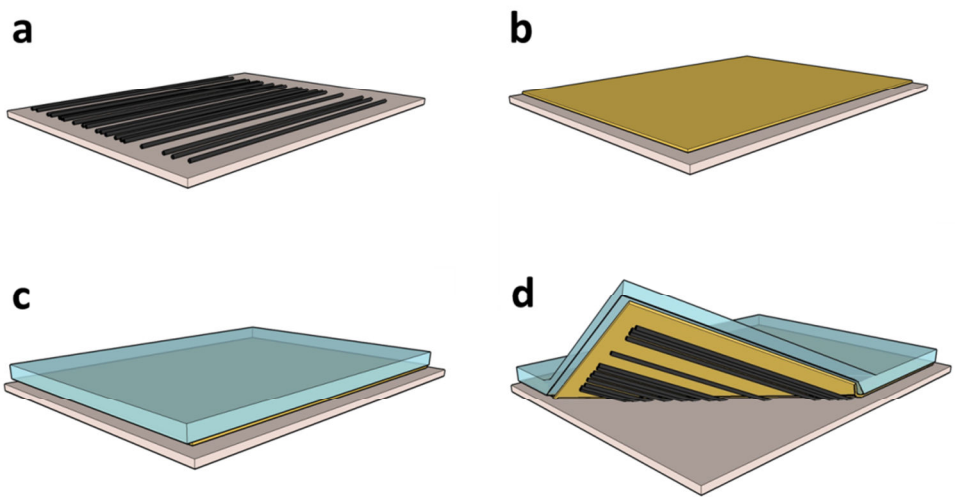

Figure 3.6 Nanotube transfer using gold and PVA. (a) Bare NTs on Quartz substrate. (b) Gold is evaporated on top of the NTs (100 nm) (c) Liquid PVA is solidified on top of the gold as a reinforcement layer. (d) The NT/Gold/PVA layers can be peeled up simply using tweezers. The next step is to place it on a receiving substrate (not shown here). Figures from Reference (53).

Another way to transfer gold coated NTs is with Nitto Denko thermal release tape as is described in (55). This is a semi-rigid tape that is designed for the semiconductor industry for the transfer of device structures. It can be obtained in 8 1/2" X 11" sheets. We cut a piece the size of the area of NTs that we want to transfer plus make it a bit longer so as to hold it like a handle (i.e.: 5 mm X 15 mm), This is particularly useful for aligning to the receiving substrate. Simply pressing the tape against the gold and peeling up brings the Au and NTs off the quartz substrate. The tape is then positioned over the receiving device substrate and pressure is applied to make certain the Au is full in contact with the receiving substrate. This tape is then released from the gold by heating the device and tape on a hotplate at 90°C for 30 seconds. The mechanism that causes the tape to release with heat is designed into the adhesive that contains microspheres that swell when heated. This serves to effectively push the tape away from the gold surface that it was previously adhered to. If the NTs and gold are well adhered to the device we find the tape will release completely leaving the gold adhered to the device substrate. If it is not adhered well

to the surface the tape will release but with the gold still be attached to the tape and not on the device substrate. In this force competition the more adhesive surface wins.

It is important to note that thermal tape does leave behind a residue that O_2 plasma does not effectively remove. The most consistent way we removed this contaminant was by argon ion milling at 500 Amperes for 45 seconds. Ion milling is not discriminate when it etches the surface, and care must be taken so as to not etch completely through the gold and damage the underlying CNTs. Alternatively one could use piranha as a cleaning method.

The gold is very sensitive to electrostatic charge and to the surface preparation and cleaning of the receiving device substrate. We have found that high energy surfaces could be reduced in a 500°C H_2 2-4 hour anneal that would then reduce the oxidized surface and facilitate transfers. Another method to help promote gold adhesion was using an ionizing fan (such as made by 3M) aimed at the receiving substrate before making the transfer. Lastly one cannot underestimate the power of water getting in the way of adhesion of two surfaces at this scale. A good remedy for less compliant devices is to bake the substrates in vacuum while heating at 150°C for 8-12 hours and then remove the devices and immediately transfer NTs to the surface. The combination of heat and vacuum drives off all of the water on the surface. HDMS vapor prime (a treatment that promotes hydrophobicity for photoresist adhesion) and Omnicoat (an adhesion promoter for SU-8) were also used in these this thesis to facilitate transfer adhesion success.

In conclusion of the topic on gold transfers, we will comment that when the methods of thermal tape transfer worked, (i.e. adhered to the receiving substrate), it was by far the more preferred method. Overall it required much less time, allowed more accurate placement of the NTs on the receiving substrate, and was a dry transfer method that did not require fluid baths to solvate the polymer medium post transfer.

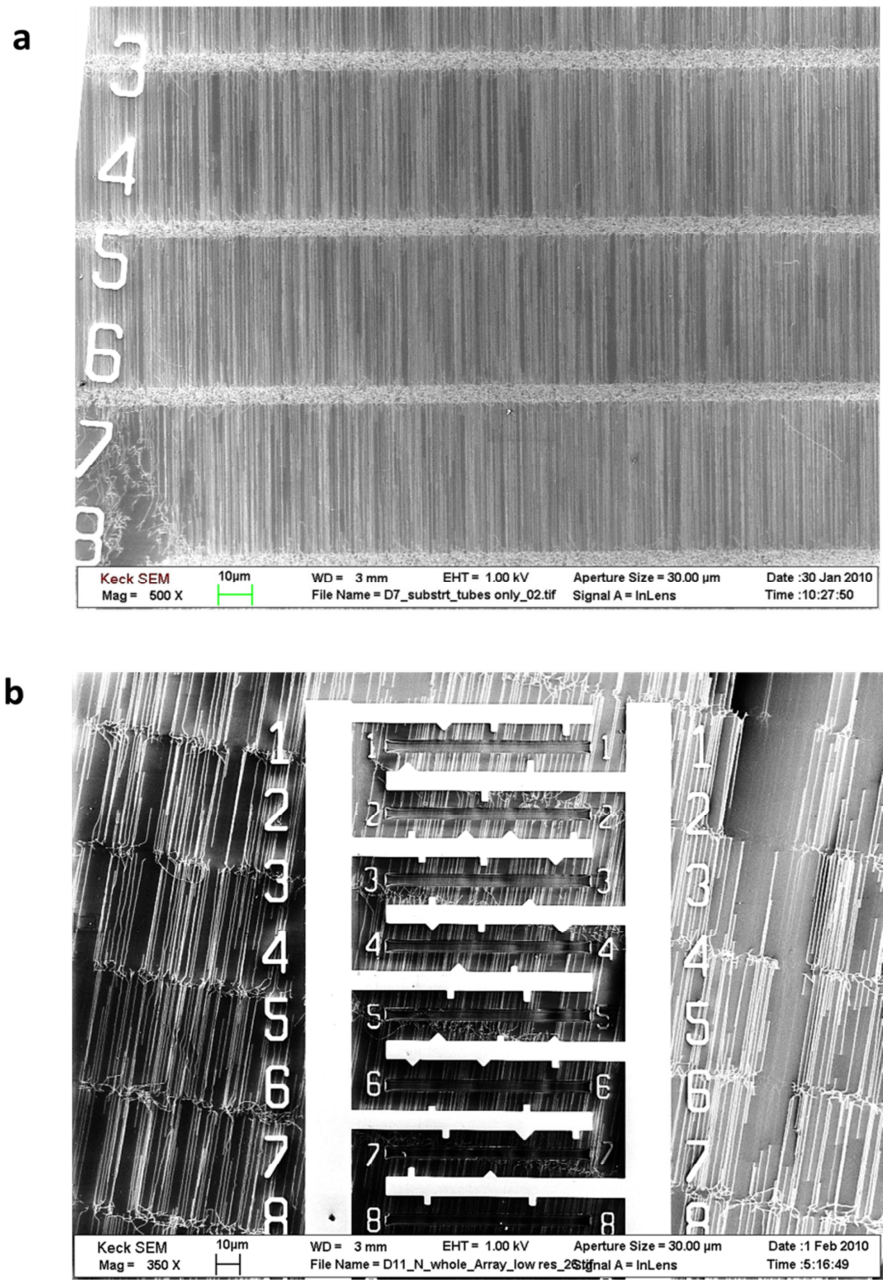

Figure 3.7 Transferred NTs transferred via gold on a variety of device substrates. (a) Carbon NTs transferred to a planar fused silica surface are seen as the dense vertical lines. We see that The NTs maintain their original high alignment with respect to each other. The horizontal rows every 50 µm are the regions of iron catalyst that transferred with the NTs. (b) Shows a transfer to a device with electrical contacts (bright white horizontal and vertical bars) and trenches (dark regions between horizontal electrodes). Close up images of the suspended regions of the device can be seen in Figure 3.8.

3.5.2 Transfers Using PMMA

PMMA transfers do not involve gold and in general the advantage of this method is that PMMA can be made to adhere to most any substrate. However this process requires manipulating the PMMA/NT film onto the device from a water bath and PMMA can sometimes be stubborn to remove, even though in theory it is solubilized by standard organic solvents.

We have followed many of the steps developed in reference (59) and (60) with some modifications as we now describe. We use 4% PMMA (495_{MW}) spun directly onto the quartz NT chip at 4000 RPM for 45 seconds. This forms a 50-100 nm thick coating over the NTs. The PMMA is not baked as conventionally done. The PMMA is then scored using a 5 μm diameter tip tungsten probe attached to a manipulator. This scoring allows the release chemistry to get to and etch away at the PMMA/quartz interface faster, and also gave us an opportunity to make symmetry breaking patterns in the PMMA. We used a rectangular design with a symmetry breaking tab cut in one corner to tell the orientation of the tubes and the PMMA layer with respect to the device substrate. Additionally we used the probe to scrape away the PMMA around the edge of the chip, about 1mm in on all sides. This step is important otherwise the PMMA tends to get caught in the jagged edges of the quartz left by the dicing saw, preventing release.

The quartz chip with scored PMMA is then placed into 1 molar potassium hydroxide (KOH) at room temperature. After just 1 hour the PMMA can be seen to be released from the chip in most regions, but is still loosely attached to the quartz. We have found that just by gently transferring the quartz chip to water by inserting the chip at a ~30° angle gently through the air—water interface causes the PMMA to lift fully away from the quartz substrate. How the water effectively intercalates between the PMMA/NTs and the quartz in that step is not well understood, but it is convenient because then one is then left to scoop the PMMA out of water instead of KOH. It is noted here that without scoring the PMMA that it can take 12-24 hours for the room temperature KOH to etch under the same unscored region.

The PMMA/NT patches float on the water. They are transferred to the devices via a thin copper wire loop that is made about 5 mm in diameter (a technique borrowed from the transmission electron microscope community which uses similar to loops to transfers thin samples to TEM grids). When scooped through the air-water interface the water will form a film over the loop due to surface tension effects of the water. PMMA can be lifted up out of the water with the loop with the water film as a support. The loop is positioned on the device and the water is wicked away gently (at a low rate) with a rolled up Kim-Wipe, letting the PMMA settle onto the receiving substrate. The device is further allowed to dry for 12 hours in air at room temperature, allowing the NTs to adhere to the receiving device substrate.

The removal of PMMA was done with large baths of Dichloromethane (DCM). The best results were obtained when the device substrates were put in a holder upside down over a stirring bar at 300 RPM and the baths were frequently changed for clean DCM. Baking the PMMA in air can also facilitate removal as described in reference (59) may be desirable of one wants a dry removal process. However, the temperatures that one must bake the PMMA at for effective removal is critically close to the temperature that NTs start to get attacked by oxygen radicals. An effective removal temperature was found to be 300°C but SEMs indicated that some NTs were attacked as indicated by an apparent reduced NT density of several assessed chips. Therefore in our work we used DCM for bulk PMMA removal followed by an air anneal at a gentler 250°C for 2 hours to remove residual PMMA.

3.6 Nanotube Transfers for Suspended Geometries

We now look at the results of transferring aligned NTs to receiving substrates that have trenches over which the NTs are suspended, as is the case for some of our experiments. In these cases we transferred NTs via gold and thermal tape to device substrates with 3 μm deep trenches of widths 2 μm to 15 μm wide etched between metal electrical contacts.

Successfully suspended NT geometries can be seen in the device SEM images in Figure 3.8(a-c), which are close up images taken of the suspended regions of the device shown previously in Figure 3.7(b). He we see aligned and suspended devices over 4,7,10 and 15 micron wide trenches. (The devices shown here were used in cell experiments and will be further described and illustrated in Chapter 4.3.)

Suspended CNTs are very susceptible to damage in fabrication in particular when the device transitions from liquid to air and also when it is transferred from one fluid to another fluid with a significantly different surface tension or viscosity. Additionally the trenches in suspended geometries seem to be aggregation points for debris during the drying process and as such resulted in a concentration of debris on the suspended NT regions, precisely the region we would like to be pristine. Therefore these devices required further cleaning with piranha (a mixture of hydrogen peroxide mixed with sulfuric acid) after the NT transfer.

Our results in achieving clean suspended geometries were obtained by etching the gold and then the device was put into DI as is standard. To transition from DI to piranha, (which has a high surface tension due to the sulfuric acid), we made 3 baths of 6:1, 5:1, and 4:1 DI:H_2SO_4 with the 4th bath being 3:1 H_2O_2:H_2SO_4—our piranha mixture. Sulfuric acid itself does not damage NTs, while piranha (with its added peroxide) can. By moving into and out of increasing concentration sulfuric acid (30 seconds per bath) the NTs were able to meet more subtle changes in surface tension and thus remain suspended. A 60 second cleaning in the piranha bath removed any polymer debris. It should also be noted that sulfuric acid and piranha etch iron rapidly. We have observed this as being effective in removing catalyst that gets transferred with the NTs.

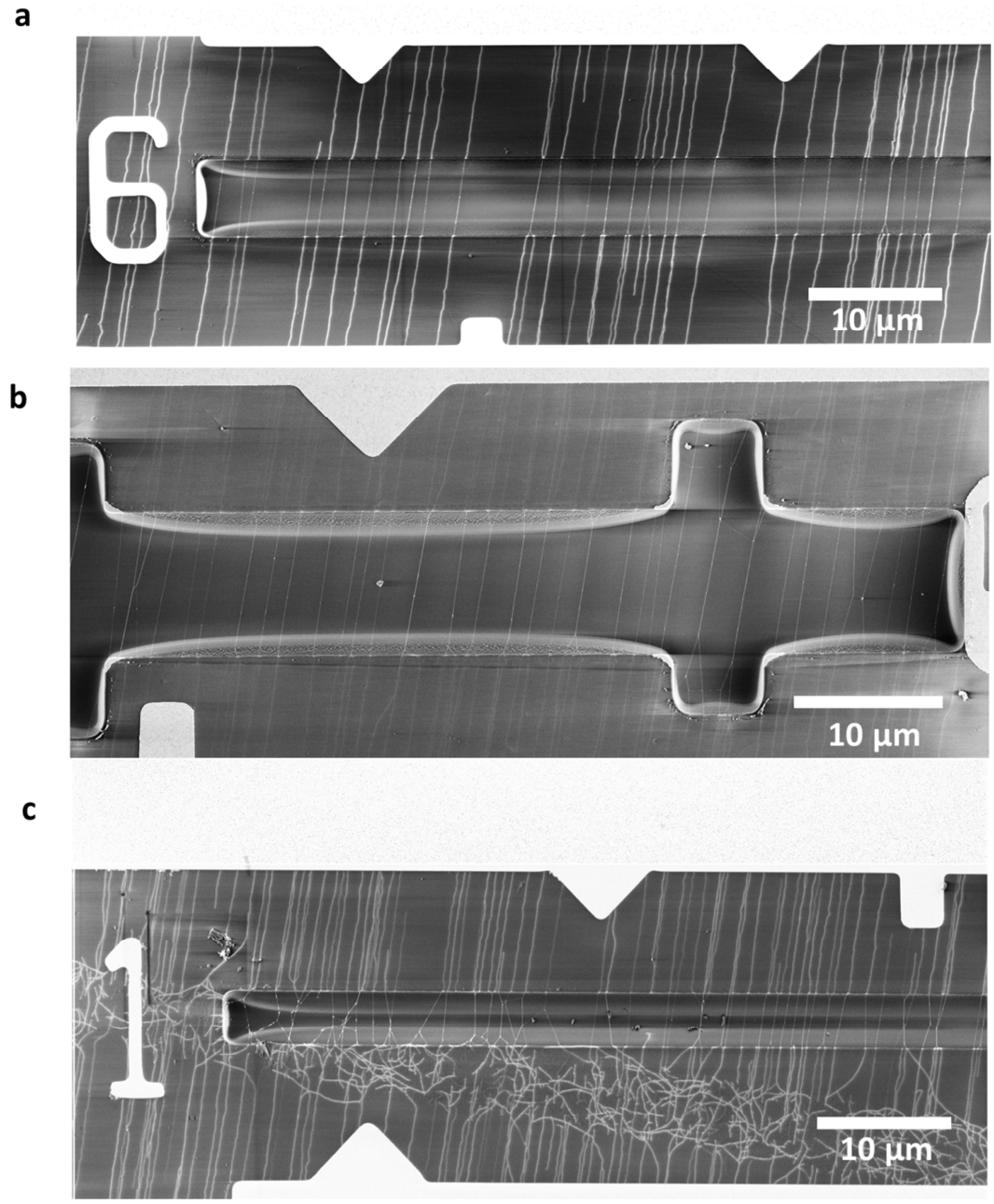

Figure 3.8 SEM Images of Aligned SWNT transferred over electrically contacted trenches. The trenches are the horizontal slots that can be seen in each image. The thin approximately vertical lines over the 2-15 µm wide trenches are aligned SWNTs that were transferred with Au and thermal tape. The trenches are 3 µm deep. (c) We see the randomly oriented NTs in the catalyst region. The region is absent of iron catalyst as it we eaten by the piranha.

Suspended devices described in thesis were always critical point dried. In this process the devices are transitioned from water into baths of successively increasing concentrations of MeOH. As in the case of piranha, MeOH has a surface tension much different than water and such gradual changes are necessary to maintain suspended devices. In the critical point dryer the MeOH immersion fluid MeOH is replaced by liquid CO_2. By increasing temperature and pressure the CO_2 passes the critical region where the distinction between gas and liquid ceases to exist. The temperature and pressure in then reduced in a way without crossing the boundary from liquid to gas. Thus the CO_2 is prevented from crossing the liquid-gas interface during drying and reduces the occurrence of surface stiction.

We initially thought that PMMA would be an ideal method to produce dry suspended devices in air. However, removing this polymer without the supporting substrate in the case of trying to suspend NTs did not work for us. The PMMA goes away during heating by dissolving—thinned suspended regions are eaten through first and opens holes in the PMMA. This polymer has an elastic quality and without a restricting substrate the PMMA pulls the NTs with it as it recedes. The result was that devices were stuck down to the sidewalls or the suspended region was torn off. We have also tried gentle removal of the PMMA using a room temperature acetone vapor removal method with similar results. We conclude that PMMA is not a rigid enough medium to hold the alignment of suspended NTs and only consider this transfer method when the NTs are fully supported along their length via a continuous substrate.

3.7 Conclusions

We have shown how we grow and transfer highly parallel arrays of aligned SWNTs on both silicon and fused silica substrates in planar and suspended geometries that incorporate electrodes and trenches. NT transfer is the fabrication step most likely to fail, and then for ambiguous reasons. The best approach is to find something that works and stick with it until it doesn't, and then debug methodically. We have also discussed several different materials we have used as a

transfer medium, and discovered that different transfer techniques are better suited than others depending on the device geometry at the time of NT transfer. We have reviewed some ways we found useful to promote adhesion of gold transfers if transfer yield is low as well as considerations for stubborn polymer removal including piranha.

Having the ability to grow NTs in known orientations has opened up a whole new world in parallel device design. NEMS research will be enhanced as we develop facile ways to build suspended SWNT geometries in both water and air. Work is ongoing in the world of aligned NT growth(51)(52)(56). In particular it would be advantageous to have a way to grow only semiconducting or metallic NTs, or even predetermine the chirality and hence radius of the NT by modifying catalyst preparation.

In the chapters that follow we will see the range of forms these SWNT NEMS can take and the systems they can be used to study.

Chapter 4

Cell Interactions with Suspended Carbon Nanotubes

4.1 Introduction

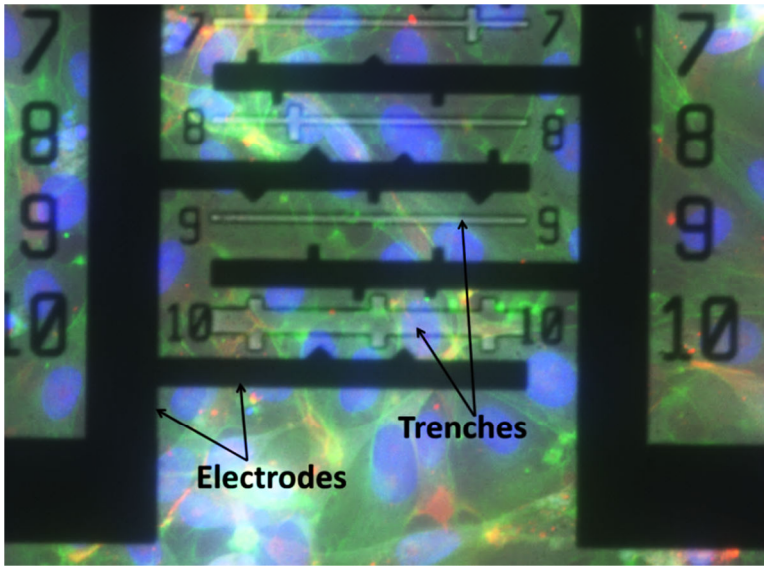

Figure 4.1 Cells grown on a CNT device chip. The dark vertical and horizontal bars are the electrodes and the colored regions represent specific organelles of the cells grown on the chip as imaged by confocal fluorescence microscopy. Notably the blue region corresponds to a cell nucleus and the green is the actin cytoskeleton. The trenches can be seen to be the narrow horizontal rectangles between the numbers, and are the regions where the NT is suspended over the substrate. It is these suspended regions that we expect to see cell-NT interactions.

In this chapter we investigate the interaction of living cells with electrically contacted and suspended CNTs. Our interest is to see if the cells interact with the CNTs, and if so, observe how they do so. An image of the experiment can be seen in Figure 4.1 which is a fluorescent microscopy image taken on an inverted confocal microscope. The dark vertical and horizontal bars are the electrodes, and the thin rectangles next to the numbers are the trenches over which NTs are suspended. The colored areas of the picture are features of the cells grown on the CNT

substrates as seen by fluorescent confocal microscopy. In this image blue represents the cell nucleus and green is the actin cytoskeleton of the cell. We will further describe this device and details of the cell experiments in sections to follow.

We will show results of live Human Umbilical Vascular Endothelial Cells (HUVECs) grown on substrates with suspended CNTs. These cells are seen to preferentially interact with the CNTs in surprising ways. We have looked at cell-CNT interactions using a unique combination of confocal fluorescence imaging and CNT photocurrent microscopy. We show image analysis that reveals the positional relationship between the NTs and the cell proteins on the Lamellipodium, the advancing foot of the cell. Additionally we look at SEMs of the cells after such experiments are done and learn even more about both the NTs and the behavior of the cells that are on them. The future direction of this framework for electro-mechanical cell studies will be discussed.

4.2 Cell Motility

To begin to picture how a moving living cell might interact with a NT that it encounters we first take a look at cell motility in general without the presence of a NT. The basic theory of cell motility described here is further detailed in reference (61) and shown in Figure 4.2 from the same reference. For our purposes we are interested in the mechanism by which a cell propels itself forward. The cytoskeleton is made up of actin which is a rigid linear molecule that organizes to push the leading edge of the cell membrane forward. This leading edge is called the lamellipodia and is a characteristic feature of motile cells. These are believed to be the actual feet of the cell via which the cell pulls itself forward during the process of cell migration. Within the lamellipodia are protrusions of actin "micro-spikes" which extend beyond the lamellipodium and are also called filopodia(62). Filopodia form the focal adhesions with the substrate, aggregating regions of membrane dense with proteins that link the cell to the surface it is moving over. Filopodia are additionally thought to be involved in sensation of chemical and mechanical cues which result in changes in the direction cell locomotion.

The regions of the focal adhesions in endothelial cells contain a dense region of actin filaments cross-linked into bundles by actin-binding proteins. In addition to actin, many other proteins appear in concentration at these points, such as CD31 which is a single-chain transmembrane glycoprotein that is highly expressed in endothelial cells, both at their junctures and at cell substrate adhesion points(63).

In The experiments that follow we want to understand how cell motility is affected by the presence of CNTs. One way we will accomplish this is by staining the CD31 proteins (along with other parts of the cell) with a fluorophore that allows us to track the position of the cell lamellipodia and understand cell—NT interactions in a new way.

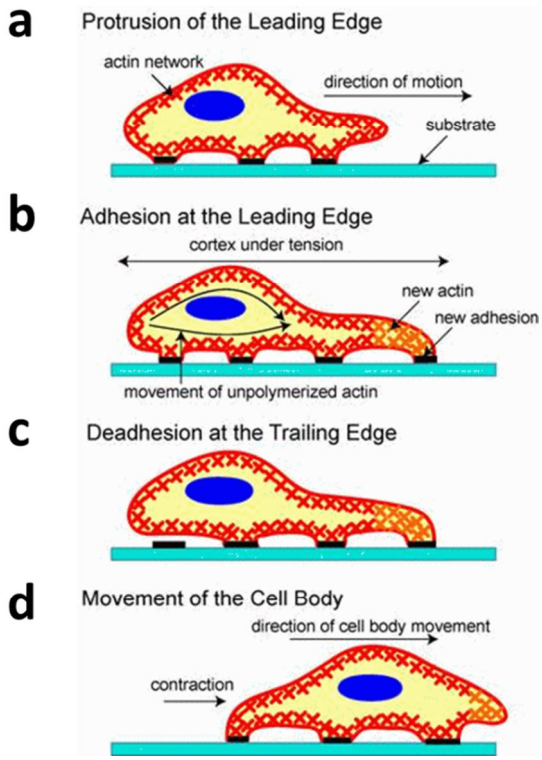

Figure 4.2 The general understanding of cell motility. The cell propels itself forward by means of extending its actin cytoskeleton network forward. The leading edge is called the lamellipodia and is essentially the cell foot which forms an adhesion with the substrate via proteins including CD31. Figure from reference (61).

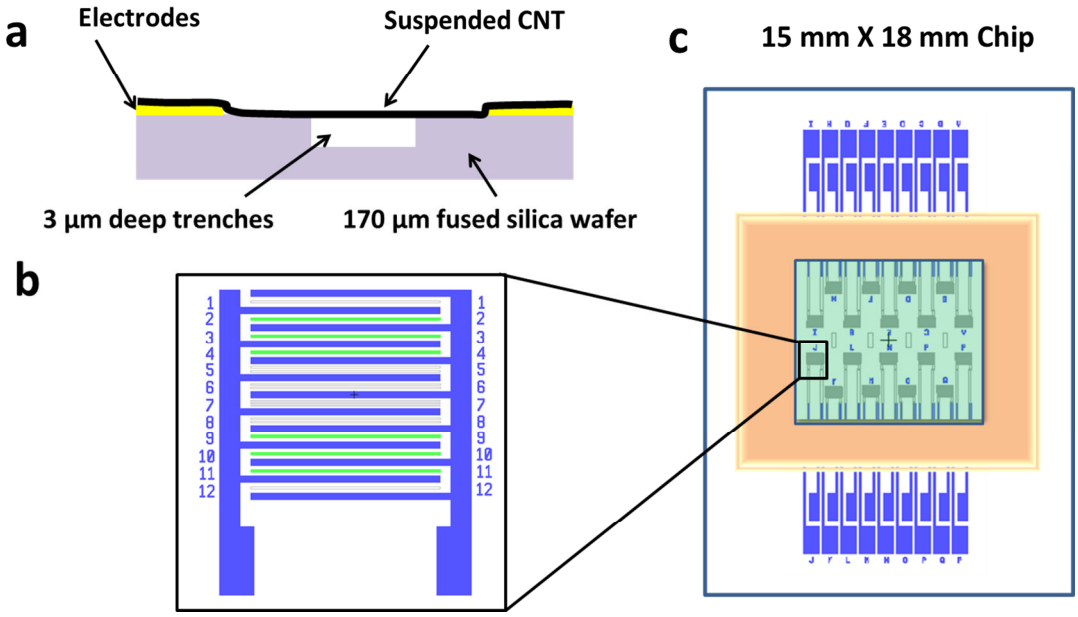

Figure 4.3 Schematic of suspended CNT device geometry with electrodes and trenches. (a) A cross section of the device showing an electrically contacted CNT suspended over a trench etched into the substrate. (b) The interdigitated electrode array utilized in these experiments, electrically contacting multiple rows of devices by one source drain electrode pair. (c) Finished device chip incorporating 18 arrays with a PDMS gasket containing fluid to the device region (orange).

4.3 Suspended SWCNT-FET Device Fabrication

The schematic in Figure 4.3(a) shows a detailed cross section of the device. The starting substrate is a transparent 170 µm fused silica wafer, which is optimal for the high numerical aperture objectives used in inverted microscopy. The fused silica is lithographically patterned with photoresist defining the trenches and the surface is etched in these regions 3 µm deep via RIE CHF_3/O_2 plasma. Trenches were varied from 1µm to 7 µm width. Electrodes were then defined according to the pattern seen in Figure 4.3(b) which illustrates interdigitated electrode arrays that allow electrical contact to multiple (on order of 100's) of NTs in the circuit by a single pair of source-drain electrode contacts. Electrodes were made from Ti/Pt (2 nm/ 40 nm) and were deposited by electron beam evaporation. Lastly the NTs were transferred via gold tape and

subsequently cleaned with piranha and critical point dried, as per the protocol outlined in Chapter 3.6 for suspended NT geometries.

The completed and suspended CNT devices can be seen in the SEM images in Figure 4.4. We see both a large area image of a whole array after the NT transfer. Figure 4.4(b) shows a close up scanning electron image of the cleaned and suspended NTs.

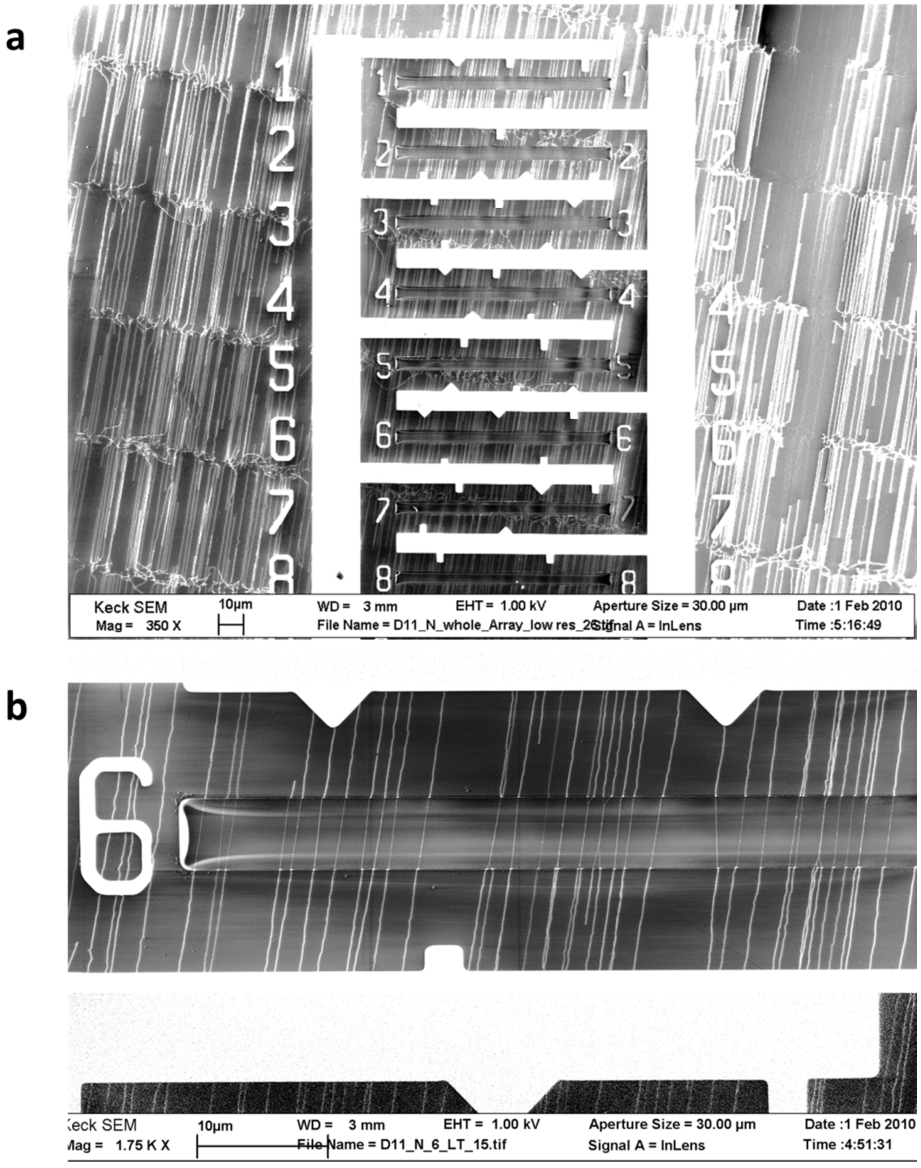

Figure 4.4 SEM images of suspended CNT devices. Here the bright vertical and horizontal regions are the electrode contacts. The slightly tilted white vertical lines are transferred CNTs.

(a) A device array showing 8 rows of suspended NT devices. (b) Close up image of the devices in (a). Nanotubes show up as bright white lines on the insulating fused silica substrate. The suspended regions appear as the fainter thin taught lines over the trench region.

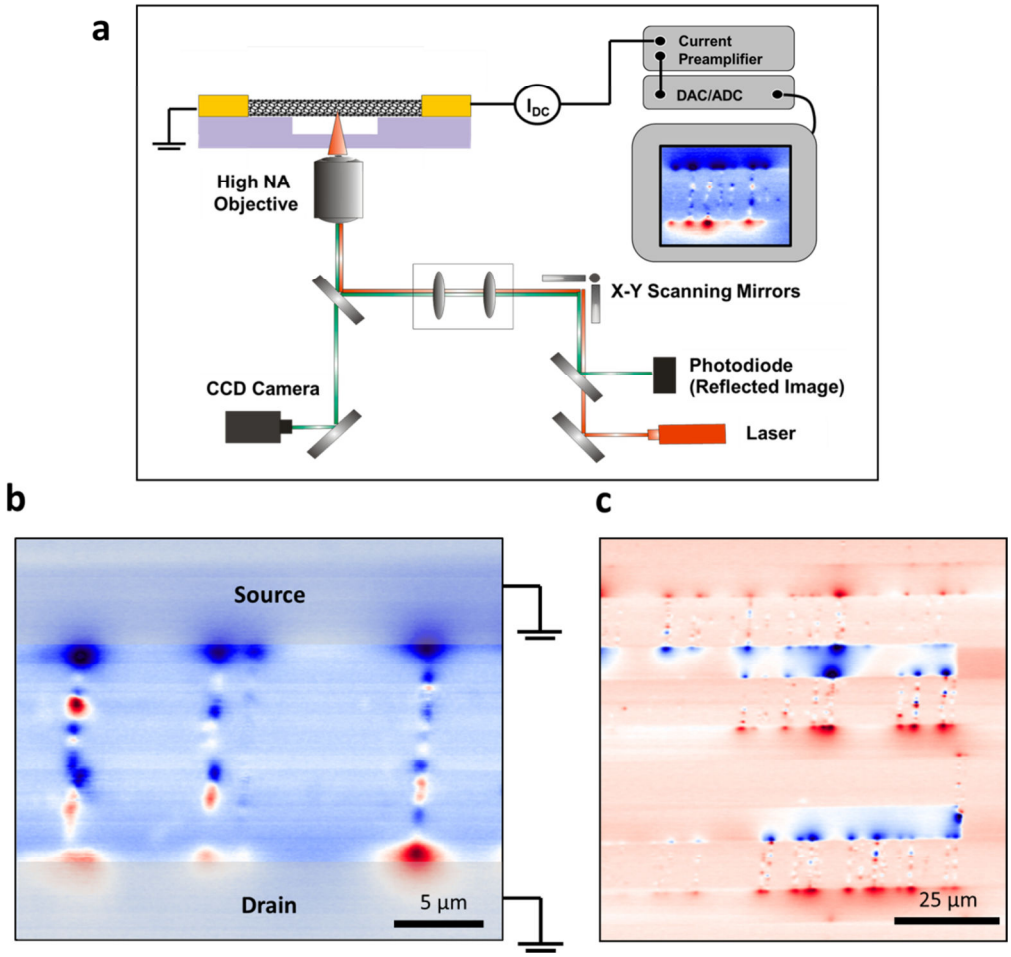

Figure 4.5 Photocurrent microscopy setup and PC images. (a) The sample is illuminated by a diffraction limited spot from a 785 nm wavelength laser. This spot is raster scanned across the sample with piezo controlled mirrors. A photodetector records the reflected light image from the sample. Meanwhile external electronics measure the magnitude of the photocurrent signal as a function of position. (b) PC imaging of a large region ~ 125 um^2 using a 10X objective. Red spots are regions of positive current and blue corresponds to negative current. The NTs are oriented vertically and can be seen as the red and blue spots between the horizontal contacts. The very dark red and blue spots represent points where the NT contacts the electrode. The magnitude of the current is 100's of picoamperes for a 10 mW incident laser power.

4.4 Photocurrent (PC) Measurement: Setup and Device Images

We use the photovoltaic properties of CNTs (as described in Chapter 1.5) as a means of observing the NT location while working in solutions which is a non-invasive and quick way to get a measurement of the positions of the NTs that make up the sample.

A schematic of our optoelectronic imaging system is shown in Figure 4.5(a). A single beam is formed by focusing a continuous-wave, near-infrared laser (785 nm) to a diffraction-limited spot of ~0.7 μm. through a 40X 0.6 NA objective. The laser beam was raster scanned over the electrically contacted CNT sample with piezo-controlled mirrors that have sub-nanometer-scale spatial resolution. The CNTs are connected to a source and drain electrodes that are both connected to ground.

Figure 4.5(b-c) shows the photocurrent map of one of our suspended NT device regions, where positive and negative photocurrent can be seen as red and blue spots respectively. The NTs run vertically and are recognized as dotted regions in the picture. The connecting electrodes are horizontal and are overlaid with a grey shaded region showing their location in 4.5(b). The especially high intensity red and blue spots correspond to the points the CNTs contact the electrodes. The photocurrent image seen in (c) was collected with a low 0.3NA 10X objective which allows a large area view. In the course of a 1 minute scan we can image 10's to 100's of semiconducting devices in one image, thus telling the exact location of electrically contacted NTs on the device chip.

4.5 Cell Experiments with HUVECs

We now describe how the device chip was seeded with cells and then prepared for confocal fluorescence imaging. A completed device was first submerged in ETOH for 8 hours to be sterilized. The chip is taken out of the ETOH and with a minimal amount of fluid over just the center of the chip, (so the suspended NTs remained wet), a PDMS gasket was placed over the device region as was seen in Figure 4.3(c). We could not seal the PDMS to the device

irreversibly as is customarily done, as this process requires O_2 plasma which damages NTs. However, the presence of the PDMS gasket was still effective in corralling the fluid and the cells within it. The ETOH was then exchanged for cell media by micro-pipette fluid aspiration of the ETOH and replacement with growth medium.

HUVEC cells were trypsinized from their culture flask and suspended in cell growth media. Media was removed from the NT device chip and the cell mixture was added to the PDMS well. The cell seeded NT device was then incubated at 37° C for 6 hours total. Phase microscopy imaging at 2 hours showed cells had already attached to the device substrate. The cells were allowed to grow and move for an additional 4 hours. At this time the cells were fixed in situ with 3.7% formaldehyde, washed with PBS, and the cells were stained for CD31, α-Smooth muscle actin, and DAPI was used to stain the cell nucleus. The fixed cells remained in a PBS buffer throughout confocal and photocurrent imaging.

Confocal fluorescent imaging was performed using a Zeiss 510 confocal microscope. Images were collected via a 63X oil immersion objective. Image stacks 15 μm high were taken using three color channels, one for each of the dyes the cells are stained with.

We can see illustrations of a 3-D image reconstruction of the confocal image stack in Figure 4.6(a-b). Here we are looking specifically at the color channel associated with the CD31 transmembrane proteins as these best define the cell boundary. In this type of microscopy we are looking from the bottom up so the image we see is between the electrodes (the bright stripes in Figure 4.6(b). Therefore the cells bodies can only be seen in the regions between the electrodes as the bright greenish regions. We note the narrow protrusions (some are indicated by arrows) that extend from the cell body into the trench centered between the electrodes. These are the regions we are interested in to see if there are NT interactions.

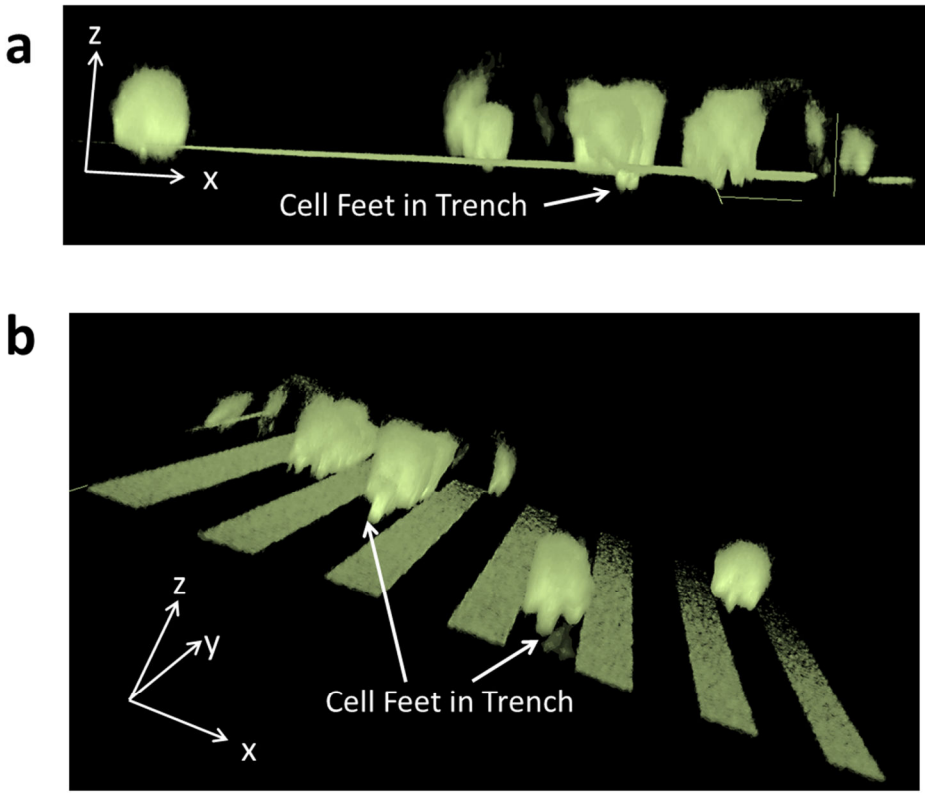

Figure 4.6 Image reconstruction of confocal microscopy image Z-stacks. Image shown ant an angle to better show features. (a) The cells pointed out can be seen to enter a 3 μm wide trench. (b) A different region of cells that enter the trenched regions.

4.6 Evidence that HUVECs Initially Step over CNTs

A closer look of the cell in the trench regions usually revealed the cells flat on the trench floor represented by a uniform fluorescence of the CD31 proteins as can be seen in Figure 4.7(a-b), where we see first the top down view and then (b) see the vertical slice through Z at the location of the white dotted line in (a) where the green represents the cell membrane and note only faint fluorescence. However, there are times when we see the cell in the trench with irregularities in their membrane features such as in Figure 4.7(c-d). Again we see the top view and then the vertical projection along X taken at the white dotted line. Additionally we see increased fluorophore intensity in the regions of cell membrane irregularity.

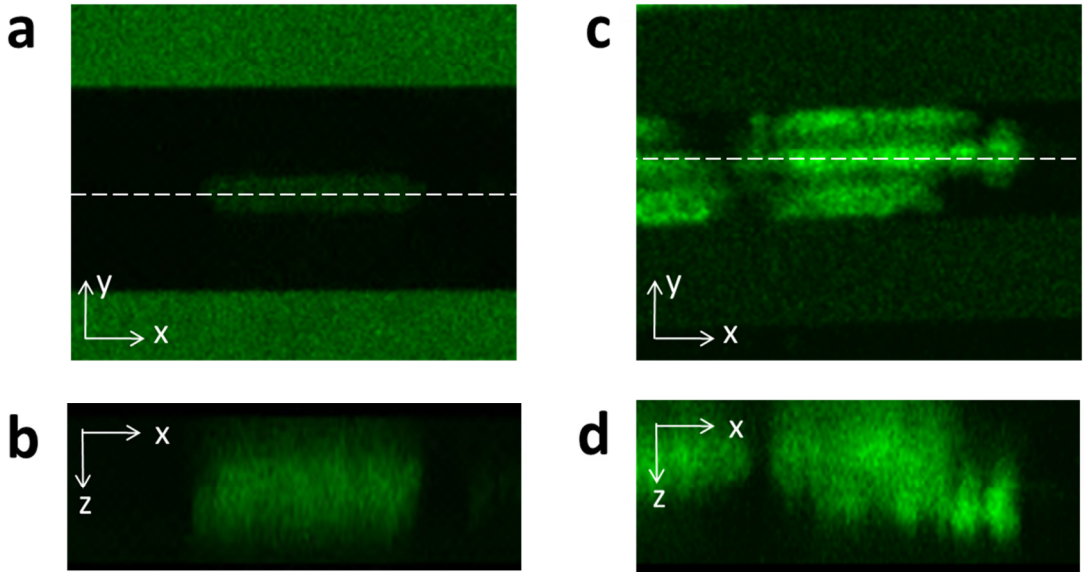

Figure 4.7 Profile of a cell in a trench. (a) Top view of cell in a trench. (b) Vertical slice through an image stack along the white dotted line in (a) through the center of the trench. We see uniform fluorescence. (c) Top view of another region where a cell exhibits different behavior. Firstly we see regions of high fluorescence in the trench region. Second, a cut through the image stack along the middle of the trench shows a non-uniform appearance of the part of the cell in the trench. This region is further explored in Figure 4.8

We now further investigate the regions shown in in Figure 4.7(c-d) of our device using photocurrent microscopy to image the region of interest. By comparing these photocurrent images with the confocal fluorescent light microscopy images we can tell where the cell is with relation to the NTs.

The results of the PC/fluorescence analysis can be seen in Figure 4.8, where the white box in the figures denoted the region of interest ROI where the cells are in the trench. Figure 4.8(a) shows a fluorescence image of the cells membrane tagged for CD31 and the fluorescence image in Figure 4.8(b) shows the actin as red and the cell nucleus in blue. We note the high concentration of actin in the ROI. The photocurrent map of that region can be seen in Figure 4.8(c). Here we see several NTs at the location the cell enters the trench. By overlaying the two images (and illustrating current purely shown in red) we can see that the regions that correspond

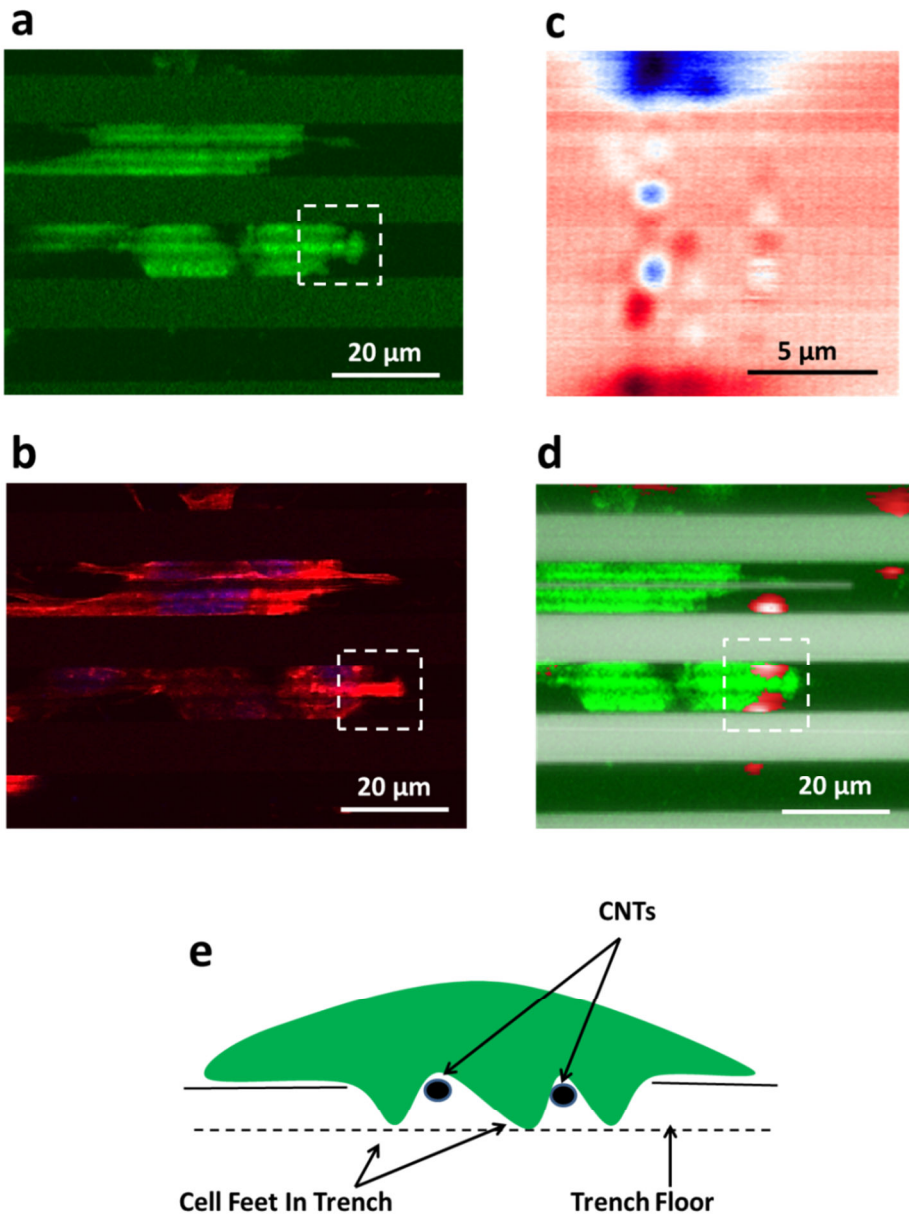

Figure 4.8 Photocurrent and fluorescence imaging of a cell interaction region. (a) Fluorescence image with the white box outlining the region of interest where the cell enters the trench showing the CD31 membrane proteins. (b) Same region as (a) but corresponding to the red actin stained filaments. (c) Photocurrent microscopy verses position for the region of interest in (a) and (b). (d) An overlay of the PC image shown in red with the cell image in (a) shows high intensity fluorescence on either side and in between the NT regions, indicating the cell is interacting with the NTs by stepping over the NTs as depicted by the side view figure in (e) which shows vertical cut through a trench, where green represents the cell, the dotted line represents the trench floor and the solid line the substrate surface.

to high densities of CD31 occur on either side of and in between the NTs. We associate the high levels of fluorescence intensity to the high concentration of CD31 at the point where the cell lamellipodia or feet extend out and attach to the next region of surface. It is apparent in this particular case the cell is stepping over the NTs on their way into the trench.

It could be that we caught the cell mid stride when we fixed the cells, and that further time would have allowed the cell to further integrate the NT within its structure. To further elucidate this we have tried such experiments with live cells on a device substrate (as opposed to fixed and cross-linked with the surface) and conducted photocurrent microscopy experiments. In these experiments the cells very quickly balled up a de-adhered from the surface due to the intense energy of the laser. We found similar results when subjecting live cells due to the lasers used for confocal microscopy. At these wavelengths the cell absorbs a great deal of the incident photon energy as heat and a living system does not tolerate such changes well. Until we can do dynamical studies it may be necessary to do a time sequence with several device chips fixed at different hours of incubation to try to understand cell/NT dynamics.

4.7 Scanning Electron Microscopy Preparation and Results

To further investigate cell-NT interactions we used SEM imaging. To prepare the chip for imaging the PDMS gasket was removed and the chip with cells and NTs were dehydrated by transitioned through 5 baths containing 10%, 30%, 50%, 70% and 90% ethanol with respect to buffer solution. The chip was allowed to soak in each bath for 10 minutes to allow the ETOH to permeate into the cells. Finally the chip was soaked in 100% ETOH and then critical point dried to preserve the delicate cell structures and the suspended NTs.. We note that usually biological samples are further coated with a metal or carbon to make the sample conductive prior to SEM, in general depositing a nanometer or more of material. We intentionally avoided this step as this deposition

layer is on the order of thickness of the features we want to resolve and we do not want to bury the NTs in a film.

We see in Figure 4.9 SEM images taken after the cells were dried. Figures 4.9(a) is a large area scan showing two cells growing over trenches. NT run vertically over the horizontal trenches. In Figures 4.9(b) we see a close up of a cell lamellipodia entering a trench, pulling against the NTs it encounters in its path. It is remarkable how much the NTs clearly stretch. Tracing the CNTs to their anchor points on the substrate and a bit of simple geometry shows that NTs in this sample were significantly stretched by the motile cells. These particular NTs did not give a photocurrent signal after the cell experiment and we assume that many of the NTs were electrically damaged due to the mechanical deformation and could even be broken inside of the cell or cell membrane.

Figure 4.9(c) shows another cell growing over several trench regions. We note here that the filopodia seem to be reaching out attaching to CNTs it encounters. We see a close up of this same image in Figure 4.10(a). We note that the NTs are stretched by the cell at several cell—NT attachment points. Likewise 4.10(b) shows a filopodia extension attaching to NTs in the trench. In this image we note that some of the NTs that the cell appears to have surrounded still show up in electron microscopy, (noted by the arrows), presumably indicating the NTs are close to the surface of the cell in those regions.

Uncharacteristically, during SEM imaging the cell-stretched NTs would be seen to break in the imaging electron beam. We note the accelerating voltage was at a 1 keV--a low accelerating voltage. We have never observed breaking of non-tensioned NTs due to effects of the electron beam when doing device characterization at these accelerating voltages, even after repeated imaging of the same section. Whether this is strictly due to the tension in the tube is it is stretched by the cell or the result of the device history of being in various fluids (such as cell media, cell fixation and staining protocols and SEM preparation) is unknown.

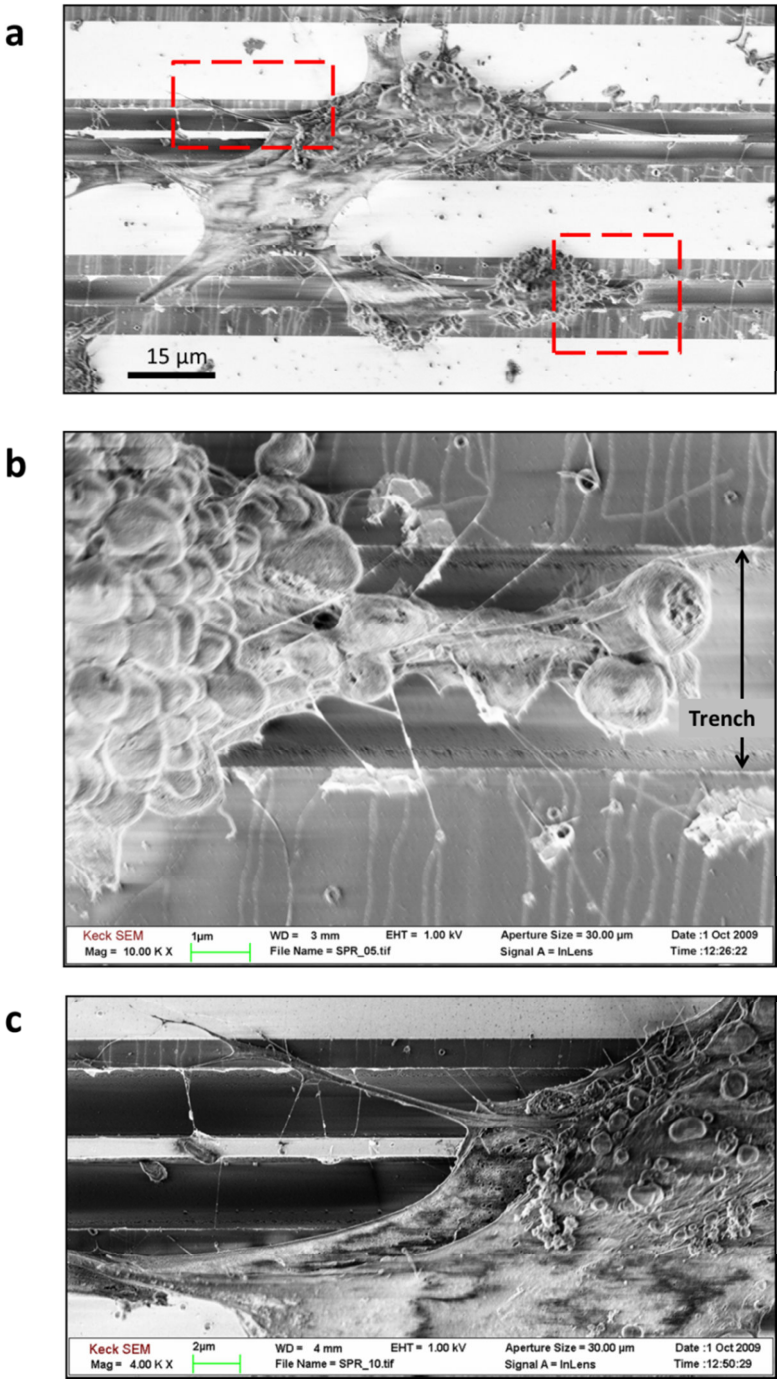

Figure 4.9 SEM images of cells over trenched with suspended CNTs. (a) Overview of device region with cell (dark bodies). White horizontal bars are the electrodes. Red boxes note the close up images shown in (b) and (c). (b) Cell Lamellipodia in a trench. We see the cell pulls on the NTs as it moves forward in the trench, incorporating the NTs into its membrane. (c) We see the spikey filopodia extending beyond the cell edge, interacting with several NTs. A close up image of this region can be seen in Figure 4.10(a).

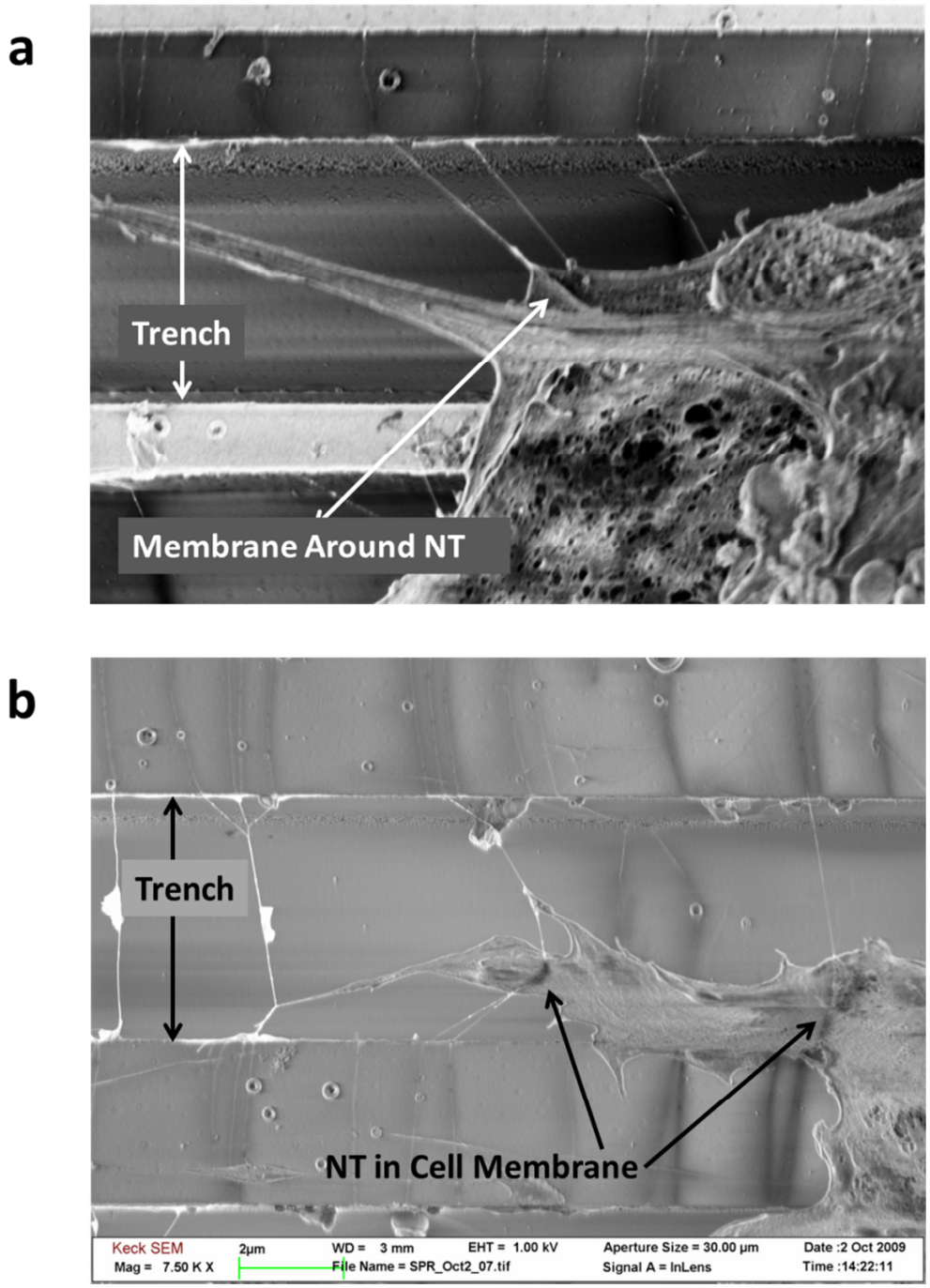

Figure 4.10 Close up images of cell filopodia attaching the CNTs. The scale is the same in both images. (a) Cell membrane seems to wick along the NT, in an apparent wetting type behavior. (b) Cell filopodia extend out and seem to preferentially attach to the NTs. In this image the cell is extending over the trench but not in it. In some regions where the cell has incorporated the NT the NT can still be seen as noted by the black arrows.

4.8 Conclusions and Comparison with Related Research

From our imaging studies we see that the cell is very sensitive to the presence of the NTs, and will respond to them in some occasions by stepping over the NTs, or alternately by attaching to and pulling on the NTs as the cell tractions forward. Our SEM imaging showed that the filopodia of the cells seem to interact preferentially with the NTs, attaching to and pulling them as the cells migrated forward, appearing to incorporate the NT into their cell membrane as it moved along. In other regions the cell could be seen over the NT but not apparent in the SEM, indicating perhaps the NT was integrated deeper within the cell interior or alternately under the cell protrusion.

We see three potential ways the cell can integrate the NT as seen in Figure 4.11. In the first the NT is cell wraps around the NT but does not integrate it into its membrane. In the second case the cell does incorporate the NT in the region of the membrane between the lipid bilayers, or lastly the NT is engulfed by the cell and pulled into the cell cytoplasm. As the cell is able to hold and pull on the NT we can assume that some part of the membrane or intracellular components such as actin networks have an effective grip on the NT, leading to (b) or (c) being the likely candidates.

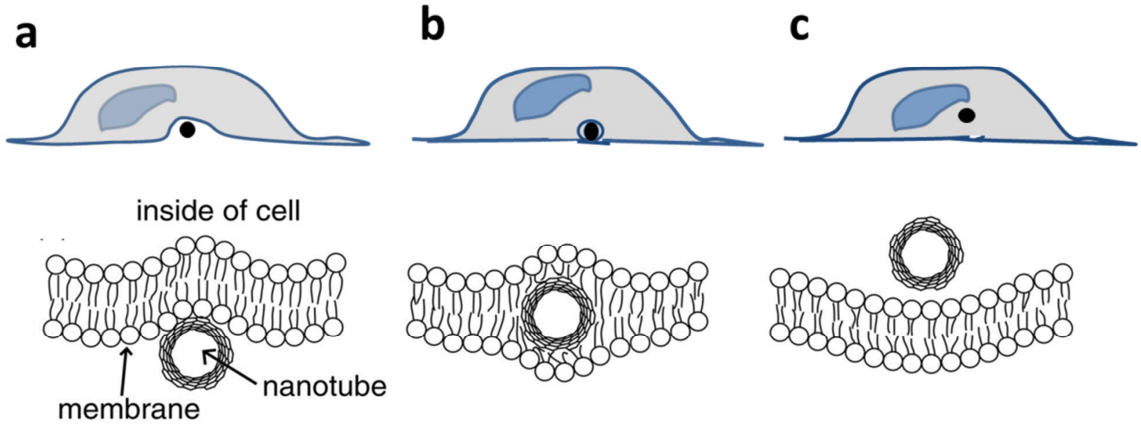

Figure 4.11 Schematic of three different NT/cell membrane geometries. (a) The cell can wrap itself around the NT, but the NT remains at the exterior of the cell. (b) The NT is incorporated into the lipid membrane leaflets. (c) The NT is totally engulfed by the cell, where at least some part of the NT is in the intercellular cytoplasm.

A similar study of suspended CNT/cell interactions on a conceptually similar trenched substrate was reported this year in reference (64). This study involved highly metastatic cancer cells which also have a propensity to grow into the trenches. There are some striking differences in the results seen. In this case their SEM analysis did not indicate a tensioning of the NTs due to cell motility. Instead the cell seemed to simply engulf the NT while the NT ends were reportedly outside the cell body. With high energy SEM (7 keV) they were able to resolve the NT inside the cell but lower accelerating voltages did not reveal the NT. Based on this they conclude the NT must be deeper below the membrane inside the cell. By using a focused ion beam (FIB) they cut cross sections of the trench region containing the NT and imaged the results using SEM. From these results they are able to verify that the cell is indeed in the trench in the region of the NT. It is noted that the NT was not directly observed in the electron images of the FIB slices, as this would require resolving the end on view of the NT inside the cell body with contrast that distinguishes it from the cell interior, the proverbial nano-needle in a haystack.

4.9 Future Directions

The devices described above are an ideal substrate for continued studies of live cell interactions. We do not know of any studies that report the unique combination of fluorescence confocal microscopy and photocurrent microscopy as we have done here. Further experiments with HUVECs are certainly warranted, especially in response to their apparent affinity for CNTs. From the vantage point of studying cellular behavior it would be interesting to see changes in cell morphology could be induced by polarizing the cells during incubation with an electrical potential across the CNT devices. In the particular case of the HUVEC cells, it would be interesting to see if the NTs could be catalysts to trigger the process of vacuole formation, a necessary step in angiogenesis.

Additionally we could observe and measure biased filopodia search or even migration towards a chemical gradient stimuli.

These results were both illuminating and exciting to observe. However, this platform does not give us a direct way to measure forces or understand the real time dynamics of how a cell integrates a NT into its structure. In particular we are left with our curiosity piqued and many new and unanswered questions. How do CNTs penetrate through a cell? Are CNTs exposed to cytoplasm or covered by a layer of surfactant like lipid? What is the CNTs interaction with the cytoskeleton? Do CNTs fuse with membrane?

In order to answer these questions a different approach needs to be taken. We would like to be able to study NT interactions with biological samples and make direct measurements of the forces acting on the NTs during the interaction. We would also like to better understand how a cell incorporates a NT into its structure.

Thus what we seek is a method to implement hold and manipulate a CNT such that we can exert forces, measure forces, and simultaneously watch the response of the NT. The initial steps in the development of this experimental framework is described in the remaining chapters of this thesis.

Chapter 5

Parallel Arrays of SWNT Cantilevers

5.1 Introduction

As Discussed in Chapter 1 the idea of making a SWNT probes and cantilevers (such as CNT AFM tips) is not new(27)(65), however such methods have yet to be developed so that high throughput of such cantilevered devices can be realized(16).

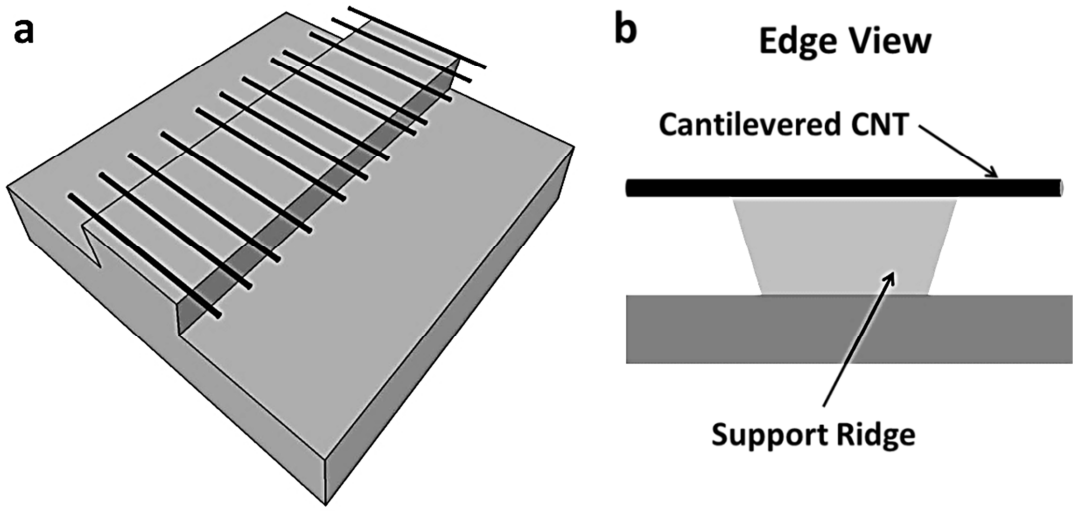

Figure 5.1 (a) Concept schematic of aligned CNT cantilevers. (b) The side view shows a support ridge that has an undercut profile to minimize VDW attraction between the overhanging NT and the sidewalls.

We present results of the first known fabrication of highly aligned arrays of SWNT cantilevers shown schematically in Figure 5.1. This project was largely motivated as a proof of concept experiment showing that aligned SWNTs could be made to protrude off a ridge in a cantilevered geometry without stiction to the sidewalls and thereby could be further utilized as probes with potentially high throughput fabrication.

In this chapter we outline how we fabricated the cantilevered devices. We show a novel striped "corrugated" substrate which was critical to the success of the design. We use SEM imaging techniques to confirm we have achieved a suspended geometry. We conclude with future directions and next steps required to realize NT poker/probes. This work was done with (then Cornell undergraduate) Alexander Ruyack.

5.2 Cantilever Device Design and Fabrication

In this section we will outline the lithography steps diagramed in Figure 5.2. We begin with a 500 μm thick single crystal Si (gray) wafer and deposit 1μm SiO_2 via CVD over the entire wafer 5.2(a) (green). This acts as the release layer. The SiO_2 is patterned with rows of SPR-220 3.0 photoresist (PR) (pink) 15 μm microns wide. The oxide is then etched completely from those rows via CHF_3/O_2 RIE Plasma etching 5.2(b). We note that the side walls have slightly sloping geometry such that the oxide trench width is widest at the top of the trench and gets narrower the deeper into the substrate one measures. This has both positive and negative ramifications for our process and we will revisit this point. An O_2 Plasma is used to remove the fluorine hardened PR. Next a 1.2 micron conformal layer of polycrystalline silicon is deposited via CVD at 200°C so as to be a low stress film. This completely fills in the SiO2 trenches plus an additional ~ 200 nm. At this point we have the geometry depicted in figure 5.2(c).

We use chemical mechanical polishing (CMP) to planarize our substrate surface. We chose Cabot SemiSperse SS12 slurry designed for silicon oxide polishing which is based on KOH chemistry and contains 100 nm scale silicon oxide abrasive particles in a colloidal suspension. Polishing was continued until the SiO_2 layer was reached and then the wafer was rinsed clean. The resultant substrate of alternating rows of Si and SiO2 is shown in 5.2(d).

Gold was sputtered over the device to 5 nm thick to promote adhesion of NTs. NTs were then transferred via gold thermal tape methods described in Chapter 2 and oriented so as to be perpendicular to the rows of oxide as in Figure 5.2(e). The thermal tape residue was removed by

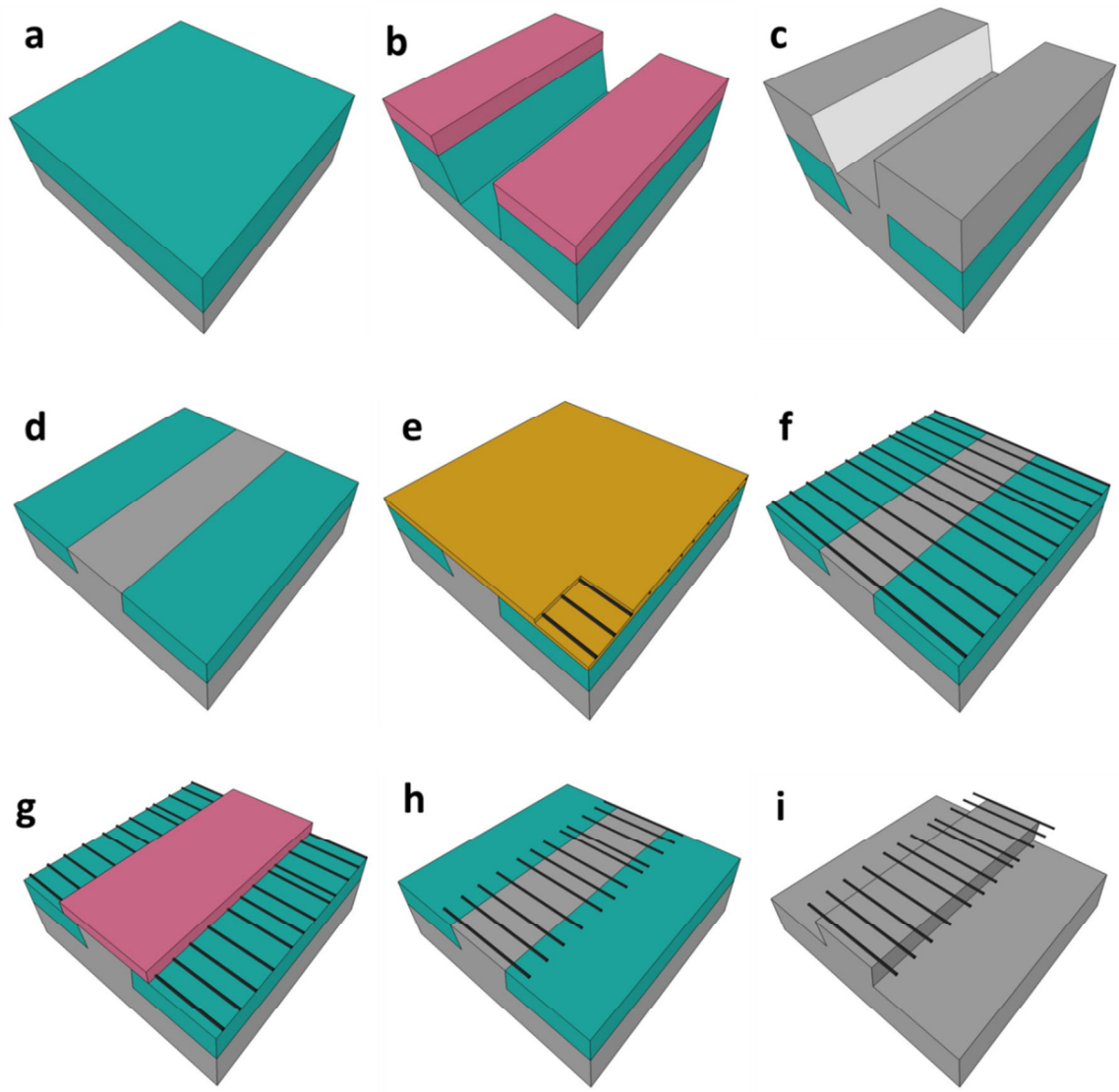

Figure 5.2 Lithography steps in making aligned SWNT cantilevers. 1 μm SiO_2 (green) is deposited onto a Si substrate (gray) via CVD. Photoresist (pink) is patterned and the SiO_2 is etched in rows every 15 μm wide. Photoresist is removed and 1.2 μm low stress poly-Silicon is deposited via CVD which completely fills the trenches as in figure (c). (d) The surface is planarized via chemical mechanical polishing. (e) NTs are transferred with gold via thermal tape. (f) The gold is milled clean and then etched away. (g) Photoresist defines the lengths of the cantilevers (pink). (h) O2 plasma etches the NTs away in non-device regions. (i) Lastly the supporting SiO2 is etched 700nm in 30:1 BOE. The device is immediately moved to MeOH and then critical point dried. (i) Completed arrays of cantilevers.

ion milling. The gold was then removed with Transene Gold-TFA etchant and the device was cleaned in water. SPR-700 1.2 was used to pattern protected cantilever regions, and open regions of the PR were exposed to O2 plasma which etched the NTs to length as seen in Figure 5.2(h). We removed any photolithography residue in piranha (3:1 H_2O_2:H_2SO_4) followed with AFM imaging to show the surface cleanliness and integrity of the CNTs. These images are seen in Figure 5.3 and show the planarized surface at the Si-SiO_2 boundary. NTs can be seen patterned to length over the SiO_2 layer (white dashed line) which serves to support the NTs (black dashed lines) while they go through fabrication.

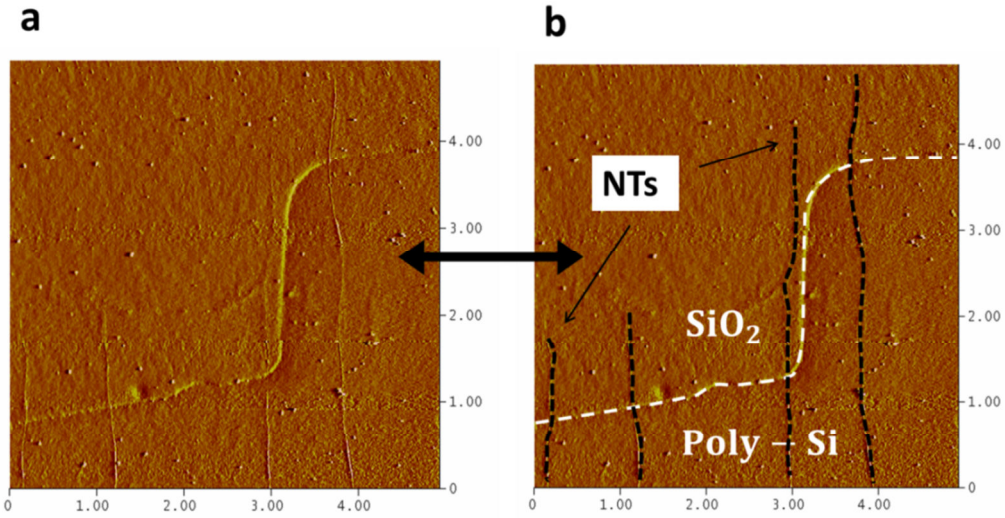

Figure 5.3 Atomic force microscopy of planarized corrugated Sio2/Si substrate with transferred and patterned aligned NTs. (a) NTs overhang a planarized silicon region onto a SiO_2 region. Both (a) and (b) are the same image AFM image. Right has an annotated overlay of region properties. The Si and SiO2 are at the same height and transferred NTs are able to be patterned to length.

Lastly we etched away the supporting SiO_2 in 30:1 buffered oxide etch (Buffer:49%HF) for 12 minutes. This is a relatively weak HF solution was useful to control the rate as CVD oxide was found to etch 5 times faster than thermal oxide. 700 nm of oxide was removed from the trenches leaving ~200 nm SiO_2 to provide imaging contrast for the SEM. The sample was transferred from BOE into water and then into increasingly concentrated MeOH (MeOH:DI in

percent volume ratios of 25:75, 50:50, 75:25) so as to change the surface tensions felt by the NT device by only small amounts from bath to bath. The MeOH was removed via critical point drying. The resultant devices can be seen schematically in Figure 5.2(i) and in SEM images in Figure 5.4 that we will describe below.

5.3 Results: SEM Imaging of SWNT Cantilevers

In order to verify that NTs are completely suspended we image the chip both at normal incidence and at a 60° angle with respect to the surface normal. The device chips were first fractured through a region which had successful transfer of CNTs and mounted in the SEM such that overhanging NT cantilevers could be seen on edge.

Figure 5.4 (a) shows a SEM image of a 280 nm SWNT extending rigidly over the edge of the p-Si ridge, showing the success of this method. The height from the top of the ridge to the SiO_2 floor is 700 nm. This NT was subsequently AFM imaged and found to be 0.7 nm in diameter. Figure 5.4 (b) shows a different region where four 75 nm cantilevered SWNTs in a row illustrating the parallel manner in which these devices are fabricated. Conversely Figure 5.4 (c) shows a cross section of a non-cantilevered SWNT ~1.5 μm long stuck down to the floor of the SiO_2 trench at its tip. We observe that all NTs longer than the trench depth (700 nm) are stuck down to the substrate in this manner. In general – we observe suspended SWNT cantilevers 75-700 nm in length extending rigidly off the p-Si ridges for their length with no perceptible change in height over its length.

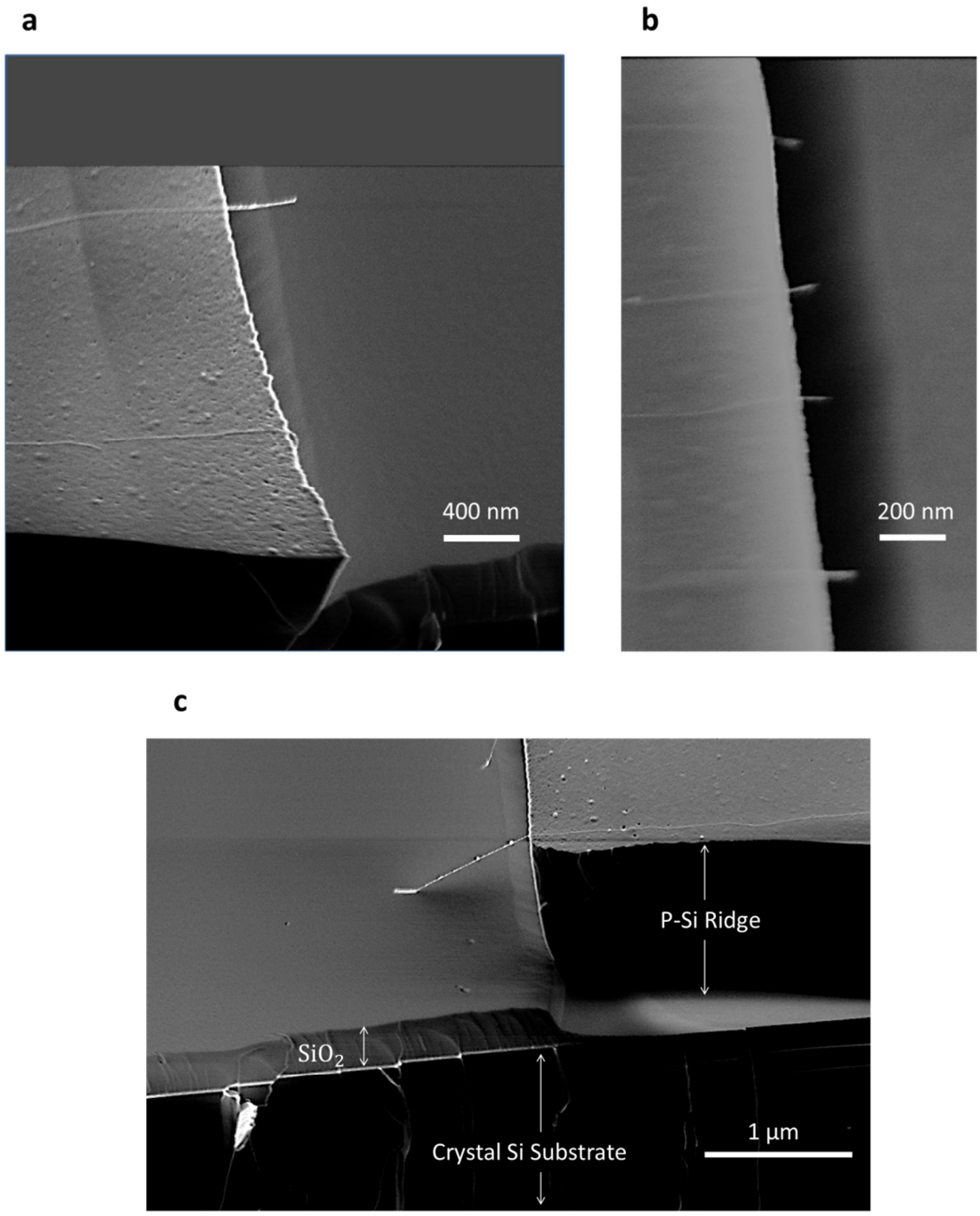

Figure 5.4 Scanning electron microscopy images of SWNT cantilevers after they are critical point dried. Image (a) shows a NT 280nm long clearly extending rigidly from the p-Si ridge. Note the angled geometry where the ridge has a slightly backward slope. Image (b) is a top view showing four 75 nm long SWNT cantilevers. When devices are longer than the distance to the base of the trench (~700nm in this case), the devices stick to the trench floor, and shown in figure (c). In this end on view we clearly see the Layers of the device, from the single crystal Si substrate to ~200 nm of SiO2 at the bottom of the trench and the supporting p-Si ridge.

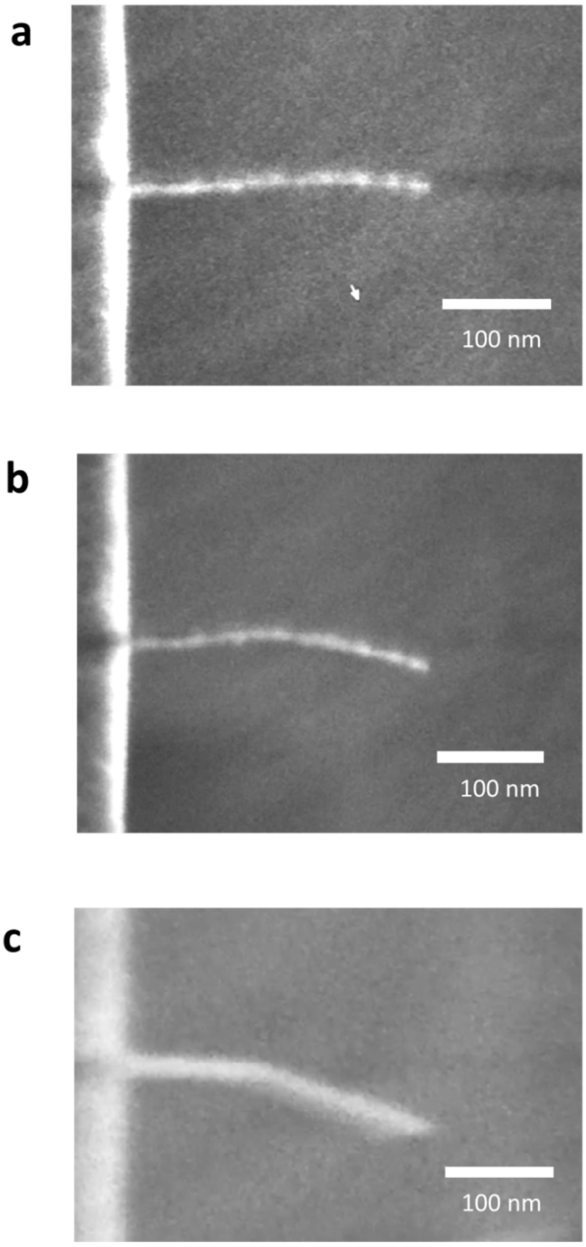

Figure 5.5 Single-walled CNT cantilever moving in an SEM. (a) A 280 nm SWNT cantilever extending from the left side of the image which shows the edge of the Si ridge the NT extends from. The NT is observed to fluctuate along its length. The NT fluctuated between the positions shown in (a) and (b) which is a tip displacement of ~25 nm. After several minutes of imaging the NT was visibly thickened from the electron beam and the NT became more rigid and finally remained in this bent shape as seen in (c).

We have recorded video of NTs 280 nm and 400 nm long fluctuating along their entire length as they are deflected in the SEM electron beam. Image frames from one video can be seen in Figure 5.4(a-b) which shows two positions of the fluctuating NT. (This happens to be the same NT as in Figure 5.3(a).) The change in position between figures (a) and (b) shows a tip displacement of ~30 nm when the sample is imaged with the electron beam raster scanning parallel to the long axis of the NT. NTs are seen to fluctuate at even greater amplitude when the beam is scanned perpendicular to the NT axis. We note that for this NT of radius ~ 0.35 nm and length of 280 nm thermal fluctuations are predicted to be ~12 nm.

The NTs that were imaged for a long period of time (several minutes) were observed to become thicker and rigid over time. Figure 5.4(c) shows the NT cantilever after several minutes of imaging. It is visibly thickened and was by that point rigid in the electron beam. This is an unfortunate but expected result known to be caused by electron beam induced deposition (EBID). In this process carbon species present on the sample surface and in the vacuum system interact with the electron beam, crosslink, and form physical structures on the sample. This process makes direct measurements of NT cantilever properties via SEM prone to error though SEM measurements have been reported by (66) on earlier NT NEM systems. The NTs were also observed to curl as they became thicker, which is attributed to the tensioning forces felt by the NT from the deposited carbon film, possibly due to a thicker deposition on one side of the NT vs. the other.

In order to attain high quality images it was necessary to operate the SEM at a short working distance (1-2 mm) to correct stigmation to the high degree necessary to resolve the CNT cantilevers. To acquire non-contaminated device images we found a place close to where we wanted to image and corrected image acquisition properties there, and then moved to the region of interest and quickly imaged the NT.

5.4 From Cantilever to SWNT probe

We now discuss the platform that we envision for future cantilevered NT probes that can be used in liquid or in air. We begin with the cantilever platform and propose with further fabrication the ridges could be made into cubes as seen in Figure 5.6. If an intermediate release layer was deposited at the beginning of the fabrication process (shown as blue), then the SWNT probes could be later separated from the substrate as shown in 5.6(b) (not to scale). One would then ideally be able to select a NT device with appropriate length for the given experiment and manipulate it (using for example an optical trap) remotely from the macroscopic world.

Realizing a probe via this sort of geometry is still the focus of ongoing work. In the meantime, , we have found a way to harness NTs by a magnetic field, as will be the focus of Chapters 7, 8 and 9, where we use magnetic handles to observe and manipulate individual NTs.

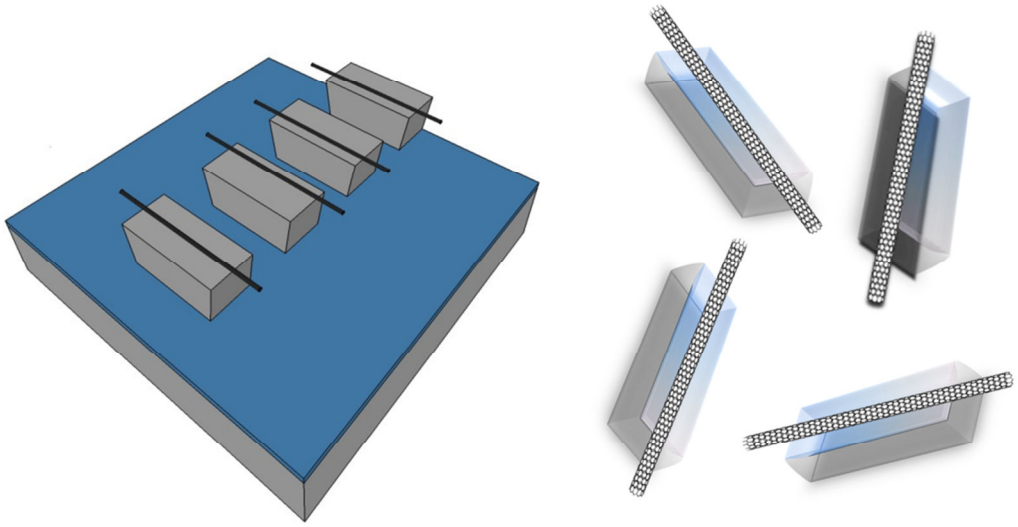

Figure 5.6 Future direction—SWNT probes. Individual CNT probes could be made much the same as cantilevers, but built upon a release layer (blue) with the supporting ridge further etched into cubes. When released from the substrate each of those cubes would become a handle to the CNT poker which could be manipulated remotely, for instance, by an optical or magnetic trap.

5.5 Conclusions

We have developed a method to create highly parallel arrays of aligned SWNT cantilevers up to 700nm in length with densities of over 1 cantilever per micron. From our analysis of the persistence length of the NTs given in Chapter 1 it is most likely that longer NTs up to several microns long would be fully rigidly suspended if the trench that they are over were to be deeper than the NT was long. At the < 1μm size scale between the NT and the trench floor, Electrostatic, van der Waals and hydrogen bonding become significant and one must take care to prevent the NTs from sticking to the surface due to stiction forces.

This striped Si/SiO_2 surface is ideal for patterning overhanging cantilevered devices to various lengths. Additionally, the sloped sidewall geometry gives the Si ridges an undercut that is advantageous for suspending CNT devices as there is less probability that the NT would bend the > 90 degrees to stick to the sidewalls. The ability to make cantilevers from aligned NT growth offers possibilities to do length dependent measurements of SWNT cantilevers where statistics can be acquired because the cantilevered devices can be made highly in parallel.

Chapter 6

Magnetic and Optical Trapping: Techniques and Analysis

6.1 Introduction

We would like to me able to manipulate and exert forces on and with CNTs on the scale of fN-nN. We would also like to have nanometer precision and remote operation of the device from the macroscopic world. Finally, we need a way to optically resolve the motion of the NT. So we are seeking a force actuator, a force detector, and a way to optically observe the behavior of the NT.

We find our answer in the biophysical community in the form of optical and magnetic tweezers. These are two of the most sensitive direct force measurement schemes that have been used to elucidate the properties of single biomolecules and other long chain polymers. These methods are considered non-contact; the molecule is manipulated with electric fields from lasers and magnetic fields from magnets that act on micron scale particles which are tagged to the molecule of interest. Additionally these particles provide optical contrast, and their motion can be recorded by camera or photodiode detector. These experiments are optimally conducted with the sample in solution, and are most often integrated into inverted microscope setups, hence their favor for use in biological experiments. In this chapter we will look briefly at the fundamental principles of both optical and magnetic tweezers and how they are used to elucidate the mechanics of many long chain biomolecules and polymers such as DNA. We will discuss the strengths and fundamental limitations of the systems. We then look at the data analysis techniques typically used in tweezer methods, deriving force spectroscopy analysis techniques and theory by which we can extract system information from the frequency domain.

This chapter provides the background and framework we need understand our device platform and data analysis techniques that are employed in chapters 7-9, where we introduce single walled CNTs as the tethered polymers of interest.

6.2 Magnetic Tweezers

Magnetic Trapping has been used since 1950 in biological studies of cells(67) and more recently extensively in the study of individual molecules such as DNA(68) and other long polymers(69). Magnetic tweezers have been used to exert and measure forces from 10's of fNs to 10 nN(70). This is a large range spanning 5 orders of magnitude and this large range of forces is unique to magnetic tweezer systems. The magnets used are either permanent magnets or electromagnets. In a standard experiment the molecule of interest is chemically attached on one end to a transparent substrate and its other end is chemically attached to a micron scale polymer sphere embedded with a paramagnetic material.

The reaction of a magnetic particle with magnetic moment μ in an external magnetic field B is dictated by the energy

$$U_{mag} = -(\mu \cdot B) = -\mu B \cos\theta \tag{6.1}$$

Therefore, to minimize its energy, the particle will try to align its magnetic moment with the magnet field. Meanwhile the particle experiences a force that is proportional to the gradient of the magnetic field. In the particular case when the magnetic moment is not a function of B, the magnetic force is given by

$$F_{mag} = -\nabla U = (\mu \cdot \nabla B) \tag{6.2}$$

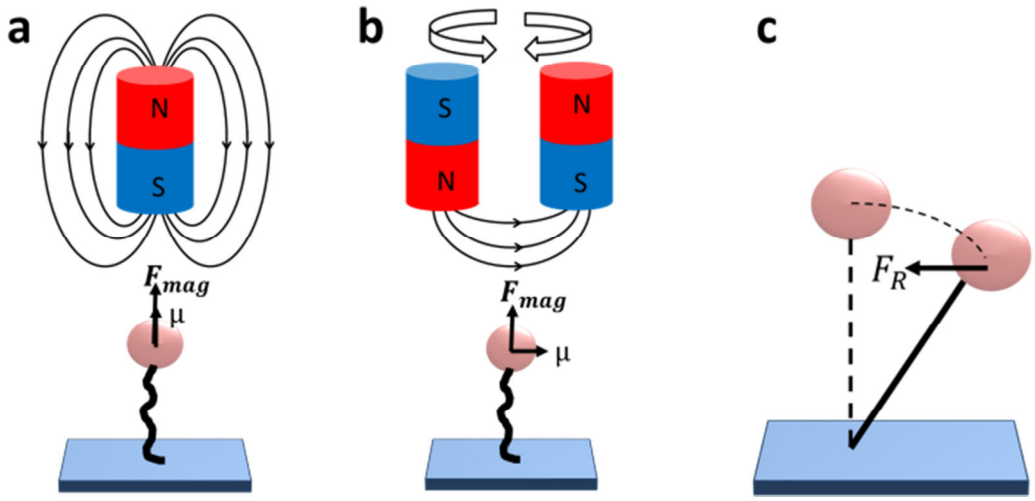

Figure 6.1 Magnetic tweezer geometry and measurement. All images show a magnetic particle attached to a long molecule (black line) which is anchored to the coverslip (blue). (a) Single magnet geometry—the magnetic moment and the gradient force align. (b) Two-magnet geometry—The magnetic moment aligns to the field parallel to the surface. The force, however, is perpendicular to this. Rotating magnets about the vertical axis twists the molecule. (c) The magnetic particle feels a pendulum-like restoring force $F_R = -k\Delta x$ from the magnetic trap when the object is displaced Δx from its equilibrium position.

The single magnet geometry shown in Figure 6.1(a) shows a tethered molecule (squiggly black line) attached between a coverslip and a magnetic bead, tensioned vertically by the magnetic field. The maximum field gradient and the magnetic field in this case both point in the same direction, as can be seen by the vectors drawn on the particle. This geometry is good for exerting strictly tensioning forces.

Twisting of molecules is accomplished with a two-magnet geometry as seen if Figure 6.1(b) with north and south poles arranged opposing each other. Here the magnetic field direction is parallel to the X-Y plane however the field gradient still creates a vertical upward force. By rotating the magnets in unison about the vertical axis, the magnetic field direction is also rotated under and this twists the tethered molecule.

The energy landscape created by the magnetic field is modeled as a harmonic oscillator potential with a linear restoring force for displacements not far from equilibrium. We expect

that if anything displaces the particle from equilibrium that the magnet provides a restoring force, F_R analogous to a simple pendulum as illustrated in Figure 6.1(c), and represented by the familiar form

$$F_R = -k_{eff}\Delta x = \frac{F_{mag}}{L}\Delta x \tag{6.3}$$

Therefore if one has a calibrated magnetic trap, they know the spring constant k_{eff}, of their magnetic system. Force detection is done by measuring optically how far the magnetic particle is displaced and calculating F_R.

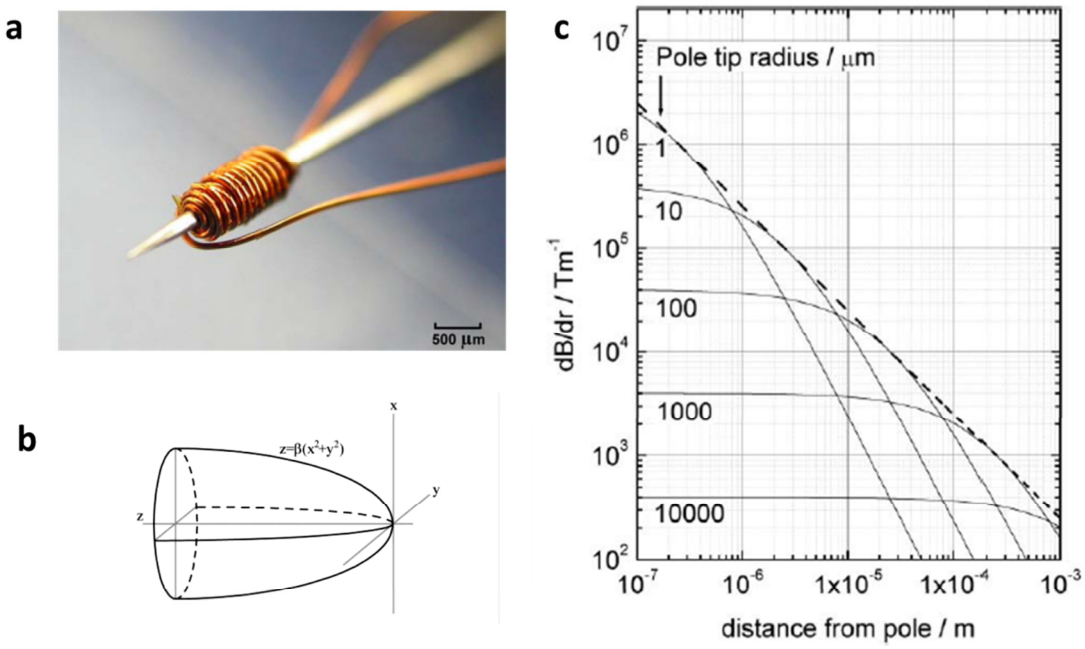

Figure 6.2 Needle like tip geometry for high magnetic field gradients. (a) Sharpened magnetic core is made into an electromagnet. (b) Model of the parabolic tip geometry used for the graph in (c). (c) Graph of magnetic field gradient for micron scale tip radii (from reference (71)). The magnetic field gradient falls off very sharply once leaving the local proximity of the probe tip, however local field gradients are quite large close to the tip and can evoke strong localized forces.

6.2.1 High Gradient Magnetic Fields for High Forces

One of the techniques used to create high forces (which we will utilize ourselves in Chapter 7) uses an electromagnet with needle-like probe geometry as has been utilized in previous experiments(71) (72). An illustration of one such configuration can be seen in Figure 6.2(a). The sharpened point serves to shape the magnetic field lines, with a sharply converging magnetic field at the point. This increases the magnetic field gradient steeply, specifically close to the tip.

The performance of electromagnets such has been calculated by modeling the system as a parabolic tip with magnetization M along the probe axis, z. It has been shown as one moves away from the tip along the z axis, the gradient of the field falls off as:

$$\nabla B = \frac{\mu_0 M_m}{4z} \tag{6.4}$$

We can see in Figure 6.2(c) a graph taken from reference (71) which shows the magnetic field gradient of a sharp parabolic tip at various radii as a function of distance from the tip as calculated using Eqn. (6.4). We see for instance that for a 10 micron tip the gradient falls off by more than three orders of magnitude when at a distance 100 microns from the tip.

6.2.2 Classic Single Molecule Magnetic Twisting Experiment

DNA is a molecule that is so well characterized by techniques of magnetic trapping that it is now used as an independent calibration device. A classic twisting measurement to measure the twist required for plectoneme formation in DNA is conducted using the two magnet twisting geometry. An illustration of such an experiment can be seen in Figure 6.3(a). The DNA coils at a certain threshold force, in lieu of twisting more. This creation of loops pulls the bead closer to the device surface. This displacement has been measured as a function of turns for two different forces as seen in Figure 6.3(b).

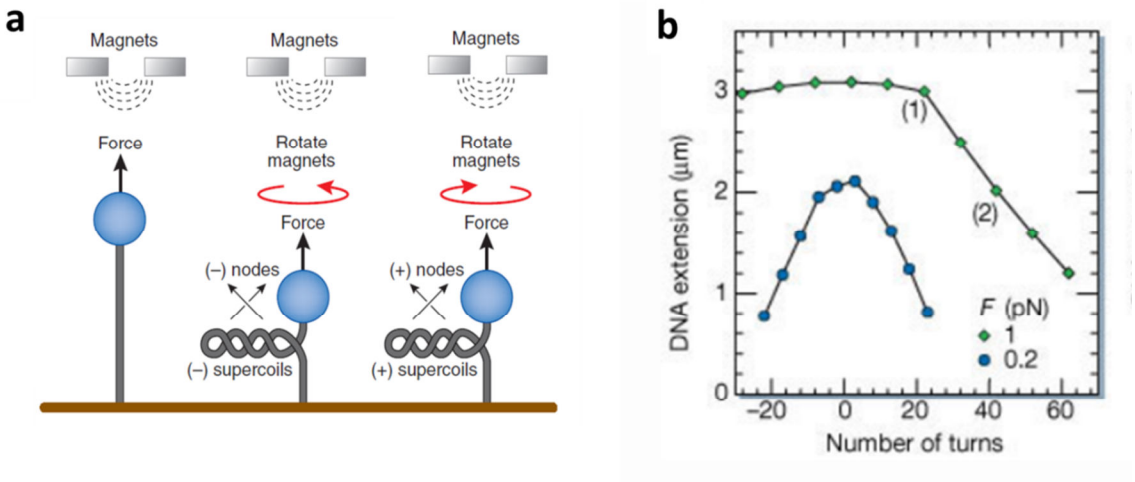

Figure 6.3 Molecules are stretched and twisted in magnetic tweezers. Under sufficient torsional strain, a twisted DNA molecule buckles to form plectonemes, shortening the measured extension. (b) Extension as a function of turns introduced into the molecule remains nearly constant until the buckling transition is reached, after which the molecule contracts. Figure from Reference (68).

An advantageous feature of magnetic trapping is that it is a constant force device(73) as long as the position of the magnets and current is fixed. Since the magnetic trap is a constant attractive potential this method necessarily requires that the studied molecule be tethered, to a substrate for instance—untethered, the particles would simply collect at the magnet. A magnetic trap can be used to exert forces in a particular direction—however, it does not have the ability to independently manipulate a particle in 3-D without the implementation of complex geometries involving a minimum of three electromagnetic poles(71).

6.3 Optical Tweezers

A gradient force optical trap allows a single laser beam to hold and manipulate dielectric particles in three dimensions with sizes hundreds of nanometers to several microns in diameter. It has been reported(74) that optical traps can make force measurements with sensitivity on the order of 10 fN with sub-nanometer resolution particle tracking techniques and can exert about 100 pN of force with 1 watt of focused laser power. Additionally, with birefringent particles and circularly polarized light one can twist molecules with optical traps as well.

In a classical configuration, a laser beam is directed into a standard inverted microscope and passed through an objective with a high numerical aperture. This light is focused onto a dielectric particle with an index of refraction greater than the aqueous medium surrounding it, as illustrated in Figure 6.3(a). The impinging light is bent at the interface of the sphere as can be seen in the ray optics diagram of Figure 6.3(b). Forces arising from momentum conservation restore the bead back toward the focus, thus trapping the particle.

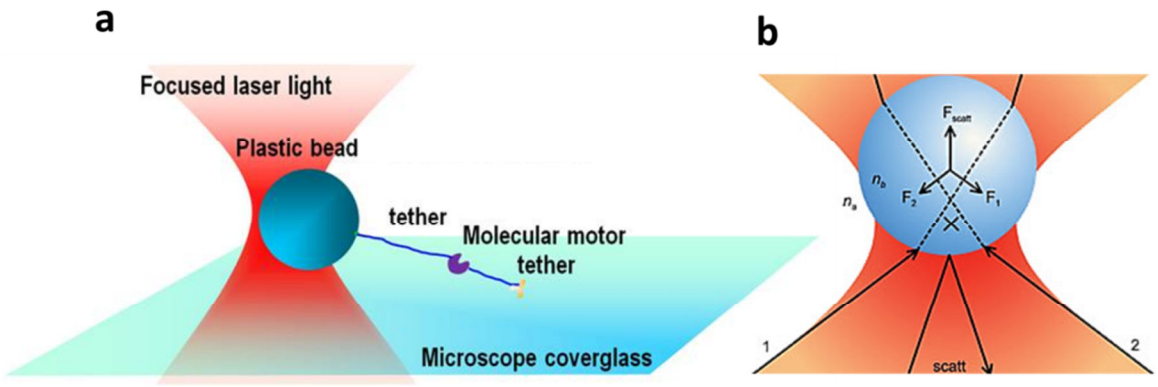

Figure 6.4 Optical trapping experiment configuration. (a) An example of an optical trapping experiment where the molecule of interest is tethered to the substrate and forces are exerted at its end. (b) Ray optics diagram showing a trapped bead. We note the upward scattering force is countered by the gradient restoring force. This leads to an equilibrium position of the bead in the forward light cone.

On a more microscopic level optical trapping is explained by understanding the particle as a polarizable material with a net electric dipole moment P which interacts with the electric field of the focused light and feel a force in the direction of the highest intensity gradient (hence gradient force). This is at the objective focus and scales as the electric field squared, we see here the electric field analogy to the magnetic field gradient force which acts in magnetic traps:

$$F_{Gradient} \propto \nabla I_0 \propto \nabla(E^2) \qquad (6.5)$$

In this case there is no simple formulation for the forces analytically, especially in the regime of beads on micron scale. Therefore each trap must be calibrated independently. As long as the

gradient force is greater than the scattering force the particle will be trapped and finds equilibrium in the forward direction of the light cone. Displacements of the bead can be recorded simply by video camera or otherwise by a photodiode detector.

It is noted here that an optical trap differs from a magnetic trap in concept in that it creates its own 3-D potential which can be used to manipulate the trapped particle in 3 dimensions. This facet makes optical trapping a likely candidate for eventual realization of manipulation of a SWNT probe. While not utilized in experiments reported in this thesis we will revisit this technique in Chapter 10 when we discuss future directions.

6.4 No Tweezers: Tethered and Non-Tethered Thermal Molecular Motion

Mapping thermal fluctuations of a molecule alone can reveal properties of the molecule, without exerting additional forces on the system.

One such class of experiments is referred to as "Tethered Particle Motion" or TPM, in which the dark field image of a reporter particle is tracked. This method was used to measure the persistence length of dsDNA(33). In that particular instance an 80 nm spherical gold particle was chemically attached to the end of a tethered dsDNA molecule. The light scattered by the gold tag made for a low background measurement of bead position, and thus fluctuation measurements could be made. The small size of the tag was chosen to minimize interaction between the substrate and the reporter particle, which can dominate when one is operating in the micron or so of fluid above the surface of the substrate. Numerous other measurements have been conducted where the molecule of interest was tagged with a particle and observed via light microscopy(75)(76)(77).

The other class of experiments corresponds to observing the molecule directly. This has been done with microtubules and actin filaments, for instance(2), where fluctuations were used to elucidate the persistence length of both. Additionally, measurements of fluctuations of SWNTs were made in solution using the photo-luminescent properties of the NT(16). In these experiments specific frequencies of light were used to optically excite the NT, and the NT

radiated light at IR wavelengths on the order of 0.8-1.5 microns depending on the chiral properties of the NT studied. This radiation was detected by a special IR camera. Image analysis was used to correlate the thermal fluctuation amplitudes and a measurement of the NT persistence length was extracted as a function of NT diameter.

6.5 Brownian Motion Theory

When working with micron scale objects in fluids, Brownian fluctuations are important and their effects often dominate an experiment. In both magnetic and optical trapping the thermal fluctuations are often used as an intrinsic force calibration device. The motion of a microscopic particle suspended in viscous fluid results from fluctuating forces which are the consequence of collisions with molecules of the fluid. The details of Brownian movement cannot be predicted exactly, however, we may assume that the events (collisions, displacements, etc.) are random. Therefore even though we cannot know the details of the phenomenon, we can determine the average behavior. In the derivation that follows we largely follow a derivation outlined in more depth in Reference (78).

6.5.1 The Einstein Relation and Stokes Formula

The motion of a particle in a fluid can be described in terms of its diffusion coefficient. The Einstein Relation gives this relation to be:

$$D = \mu k_B T \tag{6.6}$$

Where $\mu = v_d/F_D$ is the mobility of the particle, specifically the drift velocity of the particle over the drag force. For large objects the drag force F_D is given by

$$F_D = C_D \frac{1}{2} \rho v_d^2 A \tag{6.7}$$

Here ρ is the mass density of the fluid medium and A is the reference area and C_D is a dimensionless parameter that reflects the shape of the object. For a micron scale sphere in water

the Reynolds number of such a system is much less than one and the drag force has been found to be:

$$F_D = 6\pi\eta R v_d \tag{6.8}$$

Here $1/6\pi\eta R$ is the mobility in the Einstein relation, R is the radius of the bead, and η the dynamic viscosity of the fluid. Using this we find for the diffusion coefficient of a micron scale particle with Stokes radius R

$$D = \frac{k_B T}{6\pi\eta R} \tag{6.9}$$

When dealing with complex geometries one can still solve for an "effective" Stokes radius and for many micron scale systems this is representative

$$R_{Stokes} = \frac{k_B T}{6\pi\eta D} \tag{6.10}$$

6.5.2 The Langevin Stochastic Force and the Power Spectral Density

Langevin was the first to describe the stochastic thermal induced movement of microscopic particle in terms of macroscopic mechanics when describing the thermal motion of the particle(79). He attained an equation of motion beginning with terms for inertia and viscous drag

$$m\ddot{x}(t) = -\gamma\dot{x}(t) + F_s \tag{6.11}$$

Here m is the mass of the particle and γ is the friction coefficient. F_s is a fluctuating stationary stochastic force that is due to molecules in the surrounding liquid impinging on the particle that cause the apparent random motion. We add to this an external harmonic potential giving a restoring term. We then have:

$$m\ddot{x}(t) + \gamma\dot{x}(t) + kx(t) = F_s(x,t) \tag{6.12}$$

The inertial term is negligible in the highly damped case (timescales < $1\mu s$)

$$\gamma\dot{x}(t) + kx(t) = F_s(x,t) \tag{6.13}$$

We Fourier transform this resulting in:

$$(i\omega\gamma + k)x(\omega) = F(\omega) \tag{6.14}$$

Squaring (with the complex conjugate) we get

$$|x(\omega)^2| = \frac{|F(\omega)^2|}{\omega^2\gamma^2 + k^2} \tag{6.15}$$

Theoretically the one sided power spectral density PSD is defined by:

$$PSD(x, \omega) = \frac{2}{t_{meas}}|x(\omega)^2| \tag{6.15}$$

The factor of two is included because we only consider positive frequencies, and t_{meas} is the total time the measurement was made over. We now define the one sided PSD of the stochastic force $F(\omega)$ which by way of the fluctuation dissipation theorem can be found to be:

$$PSD(F, \omega) = \frac{2}{t_{meas}}|F(\omega)^2| = 4\gamma k_B T \tag{6.16}$$

We see that the power spectrum of the stochastic force is independent of the frequency as it is a white noise spectrum. Therefore the power spectral density of fluctuations is given by:

$$PSD(x, \omega) = \frac{4\gamma k_B T}{\gamma^2\omega^2 + k^2} \tag{6.17}$$

Now we want this in terms of frequenct *f* in *Hz* and the difussion coefficient *D:*

$$\omega_c = 2\pi f_c = \frac{k}{\gamma} \tag{6.18}$$

$$\gamma = \frac{k_B T}{D} \tag{6.19}$$

$$PSD(x, f) = \frac{k_B T}{\pi^2\gamma(f^2 + f_c^2)} = \frac{D}{\pi^2(f^2 + f_c^2)} \tag{6.20}$$

Equation (6.20) is the theoretical form of the PSD that is used to fit the experimental data. This power spectrum is a Lorentzian corresponding to the response function of a bead attached to a

spring, immersed in a viscous medium, and excited by the Langevin force. This noise depends only on dissipative terms.

We can see the graphical representation of the power spectral density in Figure 6.5 for two different diffusion coefficients as well as two different trap stiffnesses. At low frequencies $f < f_c$, the power spectrum is flat and represents an asymptotic white noise determined by the excitation of the spring through the Langevin noise, whereas, at high frequencies $f > f_c$, the behavior is dominated by the viscous term.

Experimentally, the one-sided PSD is given by the normalized square of the discrete fast Fourier transform of the signal *x(t)* is

$$PSD_{exp}(x, f > 0) = \frac{2}{f_{sample} * n_{samples}} |FFT\{x(t)\}|^2 \tag{6.21}$$

This is an even function about zero therefore when integrating only over positive frequencies one must again multiply the result by two to get the correct total energy. Meanwhile, the PSD relates to the variance

$$\langle x(t)^2 \rangle = \int_0^\infty PSD(x, \omega) d\omega \tag{6.22}$$

Equation (6.22) is the function we use to calculate the mean squared thermal fluctuation amplitude in the frequency domain.

6.5.3 Theoretical Resolution Limits

Spatial resolution is limited by the thermal fluctuations of the probe. Equating the equipartition of energy with a harmonic potential we can find the RMS amplitude of the fluctuations

$$\delta x = \sqrt{\frac{k_B T}{k}} \tag{6.23}$$

Where *k* is the spring stiffness, δx is the fluctuation amplitude, $k_B T$ is the thermal energy.

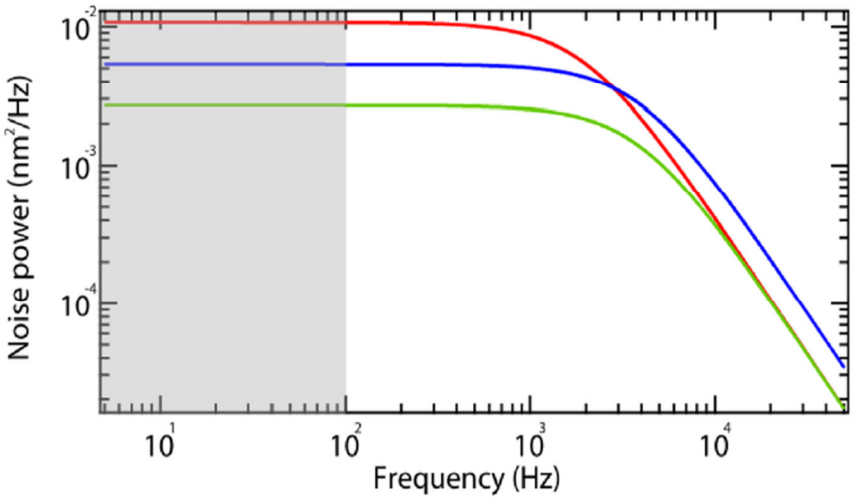

Figure 6.5 An example power spectrum of fluctuations of a trapped particle. The power spectrum for a one micron particle with a roll-off frequency of 2 kHz is shown in red. The power spectrum for the same particle with double the diffusion coefficient is shown in blue, and the power spectrum for a two-fold increase in effective spring stiffness is shown in green. The noise (area under the curve) is equivalent for the red and blue curves. Only increasing the stiffness reduced the fluctuations and the integrated area as in the case of the green curve.

From Hook's law ($F = -kx$) the corresponding force resolution is

$$\delta F = \sqrt{k * k_B T} \tag{6.24}$$

Two calibration methods are generally implemented to find the spring constant. The first is a measure of the raw displacements and extracting the spring constant with Eqn.(6.23). The second is using method of PSD analysis where a more accurate measure of the trap stiffness can be attained. Overall, the relative accuracy of a Brownian measurement is given by(73)

$$\%\, Error \approx \sqrt{\frac{\tau_b}{t_{meas}}} * 100 = \sqrt{\frac{1/2\pi f_c}{t_{meas}}} * 100 \tag{6.25}$$

Thus it is important to measure over a long enough period to bring the error into reasonable experimental error.

Because the effective stiffness depends on the force, the magnetic trap technique has a slow response time in the low force range ($F < 1$ pN). Consequently, measuring very weak forces is possible but requires a long time scale measurements to capture the full range of motion.

6.6 Conclusion

We have discussed both optical and magnetic trapping as actuation platforms for manipulating and measuring forces on individual molecules in solution. A tagged bead provides the optical and magnetic contrast, such that additional forces can be exerted on the bead/tethered molecule with externally applied fields. Additionally we have looked at the equations that govern the motion of the bead in a harmonic potential. We have seen that although thermal fluctuations limit the resolution of measurements, it provides an intrinsic calibration of the system.

This provides the framework for Chapters 7-9 where we employ the techniques outlined in this chapter to investigate magnetically tagged and tethered single-walled CNT devices.

Chapter 7

Fluctuation Measurements of Magnetically Tagged Carbon Nanotubes

7.1 Introduction

In the previous chapter we reviewed different methods to see, manipulate, and make measurements on single molecules by the attachment of a micron scale tag which has magnetic and/or optical contrast to the molecule of interest. In this chapter we will present the first work describing SWNTs with lithographically patterned micron scale iron tags attached to their ends. The tag lets us observe the NT fluctuations optically and exert forces on them magnetically. In this case the SWNT is the tethered molecule of interest, analogous to the DNA molecule described in the magnetic tweezer experiments in Chapter 6.2.2. A conceptual Image of our devices can be seen in Figure 7.1

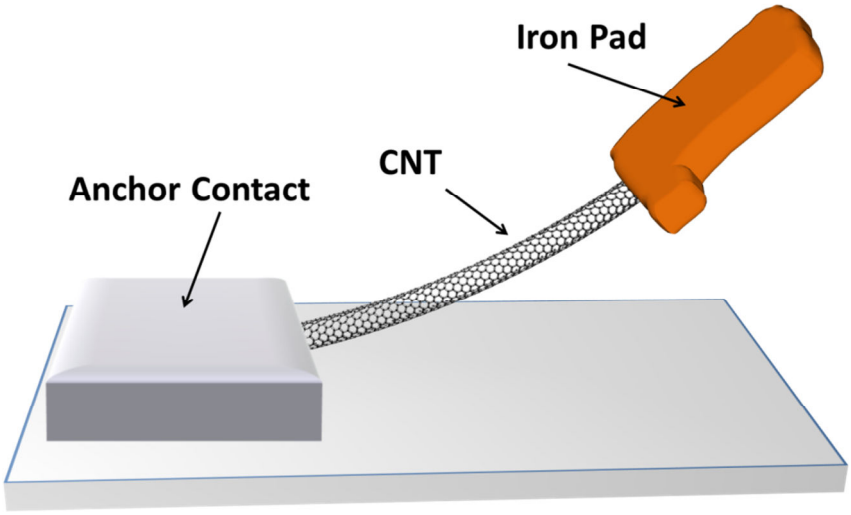

Figure 7.1 Conceptual Image of one of our magnetic SWNT devices, contacted on one end to the substrate with its other end attached to an Fe pad. The substrate is transparent fused silica for inverted microscope imaging.

In this chapter we report the fluctuations of NTs tethered to Fe pads measured in the absence of any externally applied magnetic field. We note here that in the absence of any other forces, we expect the thermal fluctuations to give us a measurement of the intrinsic NT spring constant, k_{NT} as in the familiar expression

$$\frac{1}{2}k_{NT}\langle\delta x^2\rangle = \frac{1}{2}k_B T \tag{7.1}$$

With this spring constant we can extract other fundamental properties of the NT by relating our knowledge of beam mechanics from Chapter 2. Measuring the fundamental properties of the NTs tethered in this system is the goal of these fluctuation measurements.

We begin with details of the device and the experimental setup, and then outline image and data analysis. We systematically study 10 different single-wall NT devices ranging from 4-10microns in length. One by one we elucidate the properties of our NT and NT—pad system, the NT radius, persistence length, and diffusion coefficient are all measurable by these methods. We show that fluctuation measurements are a sensitive and powerful technique to measure fundamental properties of CNTs.

7.2 Device Design and Fabrication

We use photolithographic techniques to pattern micron-sized iron pads at the ends of aligned patterned and clamped NTs. A device schematic can be seen in Figure 7.1(a). Our devices were made on a transparent 170 μm fused silica substrate, chosen for its compatibility with inverted microscopy imaging with high-NA objectives. A 50-nm-thick amorphous silicon sacrificial release layer was deposited via CVD and then patterned and etched away in areas that act as anchor regions for the NTs. (Aluminum was used as the sacrificial layer in some earlier designs). Aligned NTs were then transferred from their quartz growth substrate to the chip via PMMA (as described in Chapter 3.5.2), and aligned so that the NT length was perpendicular to the anchor bar

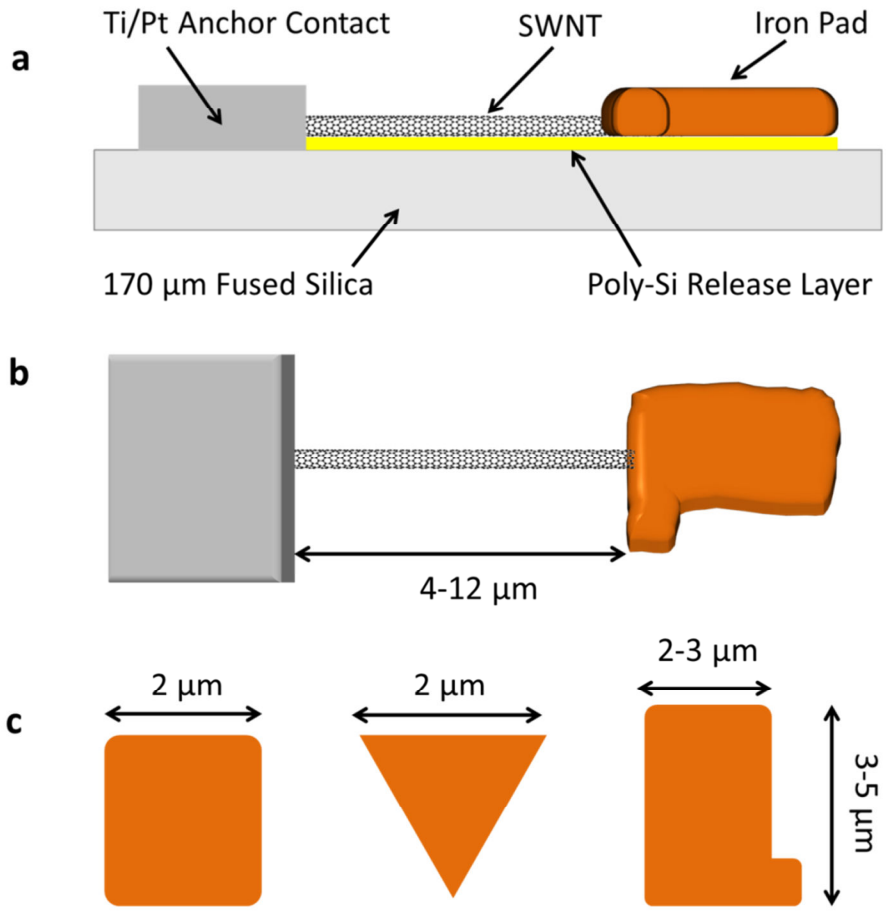

Figure 7.2 Device design schematic. (a) Cross section of lithography layers. The substrate is 170 µm fused silica. A release layer is deposited and patterned so it does not exist under the anchor contacts. Aligned NTs are then transferred covering the whole device region. Iron (Fe) pads and then anchor contacts are evaporated. Lastly the NTs are etched away from everywhere but the region between the Fe pads and contacts. (b) Top-down view of finished device with an Fe pad that has a symmetry breaking tab. (c) The three different geometry pads that were used for experiments described in this thesis.

and spanned the region between the contact and the Fe Pad. Square, rectangular and triangular pads (Figure 7.1(c) were patterned to be 2-10 µm per side and 150 nm of Fe was deposited via electron-beam evaporation. The anchor-point regions were then patterned and evaporated titanium/platinum (2 nm/40 nm) anchored the NTs to the fused silica surface. Finally, the NTs in non-device regions were etched away using oxygen plasma. The only NTs that remain were between the Fe pad and anchor contact. The lengths of the exposed NT region were between 4

μm and 12 μm in length and spaced so they were not able to interact with one another. A schematic of the top view of a finished device can be seen in Figure 7.3(b).

Figure 7.2(a) is an SEM image of completed magnetic NT devices prior to the release layer being etched away. We can see the same image annotated in 7.2(b) which identifies the corresponding features, most notably the two square regions are the Fe Pads and the slightly diagonal lines are the NTs.

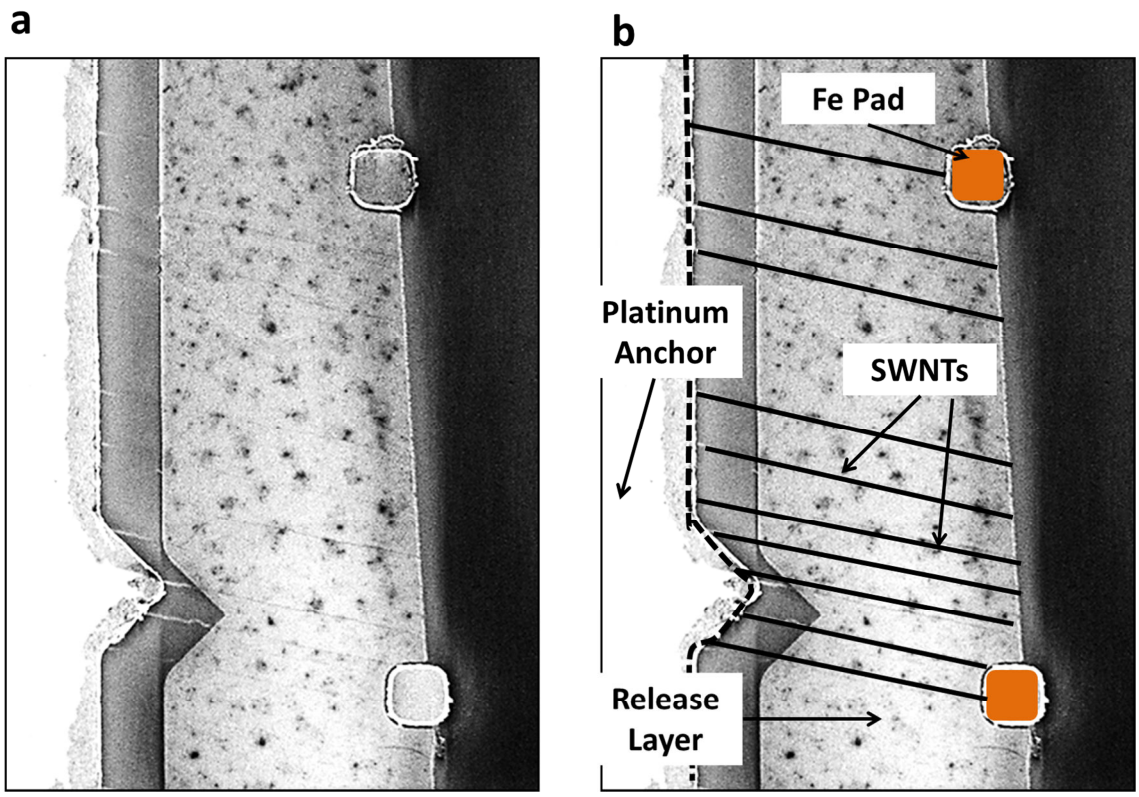

Figure 7.3 A SEM showing a top-down image of SWNT magnetic devices. (b) shows the original SEM image and (c) is annotated marking important features. Notably we see two false-colored Fe pads, each 2 μm^2 (shown orange). The NTs are running between the contact and Fe pad as illustrated by the black lines. The Fe pad in the top of (c) can be seen to be connected to one NT. The bottom device is connected by two NTs

Prior to experiments, the chip is immersed in 1 molar potassium hydroxide (KOH) to etch away the sacrificial release layer. The chip is then transferred to water and placed on the microscope with a layer of water on top ~500 μm thick. Water level is maintained during the

experiment. Nanotubes that span the region from contact to pads are released from the substrate but remain tethered under the opposite anchored end. Fe pads that are unattached to NTs diffuse away into the KOH or subsequent water baths. Devices are used for experiments within a week of the KOH etch, and are stored in water at 4°C to prevent bacterial growth.

7.3 Experimental Setup and Data Acquisition

Our experimental setup consists of an inverted microscope operating in transmitted light mode. It sits atop a vibration-isolated table and the standard microscope stage has been replaced with a home-built stage with micrometer adjustments designed to reduce stage drift when taking long time scale measurements. The sample holder of our stage was machined from brass, a non-magnetic material. The NT device sample was first adhered to the stage sample holder via hot wax (Tacky Wax) that was brushed on the stage plate with a swab and then heated on a hotplate to 60°C. The fused silica NT device chip (covered in water) was set into the melted wax frame and allowed a minute to cool before mounting on the microscope stage. The wax served as an effective clamp, minimizing drift, as well as a hydrophobic barrier that kept the water localized on the chip.

We collected a bright-field image of the Fe pad through a 60X water-immersion objective with a numerical aperture of 1.2. The use of a water objective is convenient as the top of the chip is also in water, making for a matching index of refraction above and below the substrate and no corrections for focal depth needed to be made. After the objective the image passed through a 2X image expander and was captured with a Sony XCD-V60 progressive scan CCD camera operated through a LabVIEW interface. The raw data is in the form of video 320 x 240 pixels per frame taken at 100 Hz with a shutter time of 5ms.

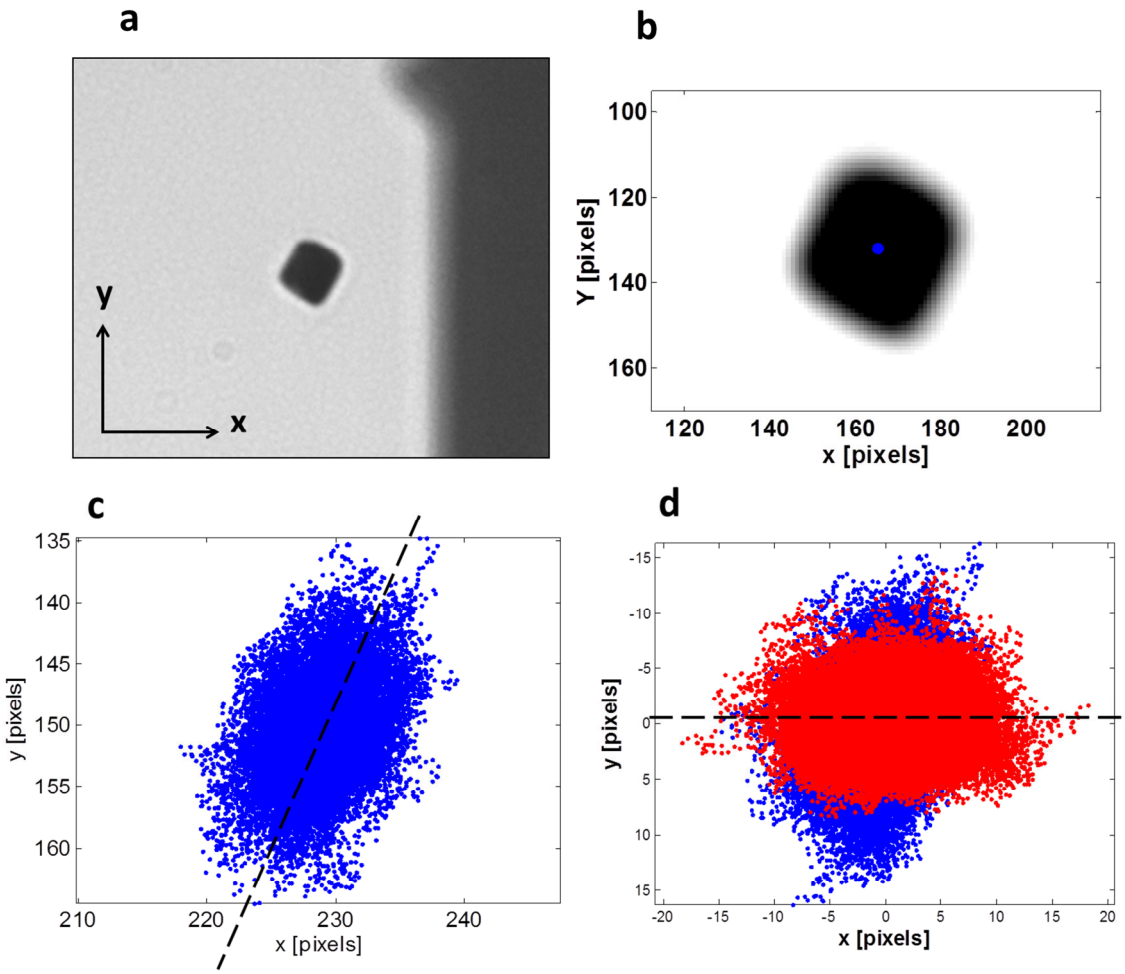

Figure 7.4 Raw and processed video data. (a) A video frame of a 2 μm^2 Fe pad tethered to a 7 μm long NT over a fused silica substrate (light grey) and anchored to its right under a Pt contact (dark vertical bar right side of image). (b) Image analysis of (a). The background is subtracted and the image is low pass filtered and thresholded. The resultant image is integrated and the centroid is calculated, shown as the blue dot in the center of the dark Fe pad.

7.4 Image Analysis of Iron Pad Fluctuations

We now look at fluctuations for one device. Figure 7.4(a) shows a single video frame of a square iron pad attached to a contact. This shows a 2 μm X 2 μm X 150 nm Fe pad attached via a 7 μm long SWNT (not visible) to an anchor contact which is seen as the dark bar in the right of the image. The contact bar in the image additionally acts as a reference marker for height

measurements and monitoring drift. The device fluctuates above the surface due to thermal motion, and has an out of plane orientation due to the ferromagnetic iron pad's orientation as a compass is the earth's magnetic field. This was established experimentally in early experiments which can be seen Appendix A. We will mention a particular application of this in the conclusion of this chapter.

We record fluctuations of our NT-Fe device for 60,000 video frames to capture the full motion of the device. We process the video data by using center-of-mass particle tracking to find the centroid in each video frame. In this process the frame is first background-subtracted and the region of interest containing the Fe pad is cropped. Then upper and lower threshold values are defined which uniquely identify the Fe pad in the image. A Gaussian convolution is used to average each pixel over the surrounding 4 pixels thus filtering the image. The centroid of the pad is found by calculating the weighted mean of the pixel positions. Given pixel intensity I_{xy}, the center of mass in x is given by:

$$\langle x \rangle = \frac{\sum_{x,y} x I_{x,y}}{\sum_{x,y} I_{x,y}} \tag{7.2}$$

A processed image of the Fe pad in the orientation of Figure 7.7(a) can be seen in 7.7(b), where the mean pixel position in x and y is given by the centroid which is superimposed as the blue dot at the center of the Fe pad. This method is a means of achieving sub-pixel position resolution, is computationally efficient, and at the same time is very accurate(80).

To visually see the region traversed by the pad we plots the centroid position for all frames as a function of its x-y plane pixel position. An image of this can be seen in Figure 7.4(c). It this picture the blue pixels represent the centroids for 20,000 of the video frames. We see a black dashed line which defines the axis through the data along which the largest amplitude fluctuations occur along. This is what we will refer to as the principal axis. Looking at Figure 7.4(d) we see the principal axis rotated onto the x axis for and the same data shown in red for distinction. This assignment is for ease of comparison of the results. The dashed line is shown again for reference

of the rotation angle. The fluctuation measurements reported in this study are all made with reference to the principal axis, or largest amplitude fluctuations.

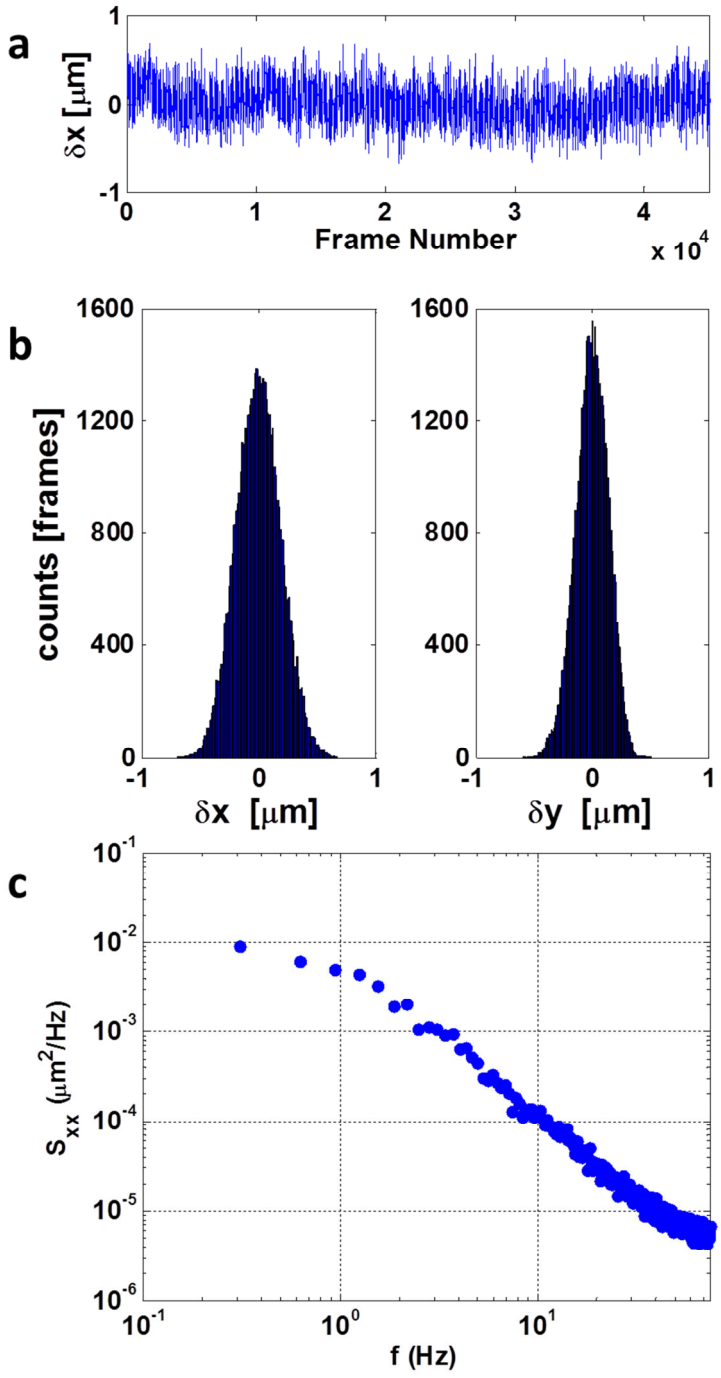

Figure 7.5 Centroid position in time and space. (a) Centroid position as a function of time shown for 45,000 video frames. (b) Histograms of the centroid distribution parallel and perpendicular to the principal axis of rotation, which will be simply referred to as *x* and *y* respectively

We next look at Figure 7.5 which shows a time trace of the centroid position for 45,000 video frames. This signal is consistent with that which is observed for random Brownian fluctuations. In Figure 7.5(b) we see two histograms that represent the centroid distribution parallel and perpendicular to the principal axis of rotation, (which will now simply referred to as *x* and *y* respectively). We see the fluctuations are normally distributed which is also consistent with what we expect to see for Brownian motion.

With this analysis alone we can get a measure of the spring constant directly from the width of the Gaussian distribution. In general however we calculate the mean-squared-fluctuations by using the power spectral density analysis that was defined in Chapter 6. We recall the PSD is found by the square of the fast Fourier transform of the signal *x(t)* seen in Figure 7.5(a). The PSD for our device can be seen in Figure 7.5(c). It is the integral of this PSD which gives a measurement of the mean squared fluctuations of the NT device. (Eqns. 6.21 and 6.22).

$$\langle x(t)^2 \rangle = \int_0^\infty PSD(x,f)df \tag{7.3}$$

We measure the thermal fluctuations arising from Brownian motion. The equipartition theorem gives us a way to relate this to the spring constant, and it is via the spring constant that we can relates the NT's physical properties with the measured thermal properties of the system.

7.5 Length Dependent Fluctuation Measurements

As we have seen in Chapter 2, the spring constant that we want to measure varies as a function of $1/L^3$. If we are truly measuring intrinsic properties of the NT then a study of NTs of various lengths should reveal differences in spring constants.

We identify single-NT devices for our study by rocking the air table the microscope sits on causing the fluid on the device chip to move in a wave like fashion along all axes while we observe the device motion. Devices which are contacted by more than one NT are apparent as they tend to have a flapping motion associated with movement preferentially perpendicular to the

NT length and an unwillingness to move side-to-side. Devices for our experiments must move freely in all three dimensions without preference, and map out an arc in space as would an inverted pendulum with respect to its anchor point at the CNT contact. We also check that the device can freely rotate about the anchor point by spinning a small permanent magnet over the sample by hand. We found that almost all device pads designed greater than 3 μm wide were most likely contacted by more than one NT and had to be eliminated from these studies.

We measure the thermal fluctuations of 10 different NT devices varying in length from 4 μm to 10 μm. The devices used in this study all had Fe pads that were either 2 μm triangles or 2 μm squares. These devices were all on the same chip (all went through the same processing) and all meet our criteria for single NT devices. We recorded the thermal fluctuations of each device for ~ 60,000 frames or 10 minutes each to capture the full motion. We then image processed the data finding the centroids for the device in each video frame.

In Figure 7.6(a) we can see the centroid distribution for three different length NTs. We see that the distributions are nearly spherical and note that longer NTs have larger amplitude fluctuations, which seems quite intuitive. We compute the mean squared fluctuations for each device and use this to calculate the spring constant for our NTs. We plot these results in Figure 7.6(b). The left hand Y axis represents the inverse squared fluctuations and the right hand Y axis gives the spring constant, in units of N/m which is plotted as a function of NT length. We observe two key things: First the nanotube string constant indicates a very soft spring indeed. We see that the sample has NTs with spring constants from $10^{-7} - 10^{-8}\,\mathrm{N/m}$. We can compare them with the softest commercially available AFM tips which are as low as 0.01 N/m, 5 orders of magnitude difference. Springs that are as soft as NTs, yet as strong, have the potential to be very sensitive in direct force detection devices—by Hooke's law smaller spring constants mean larger deflections for a given force. Therefore a CNT would be a very sensitive direct force detector.

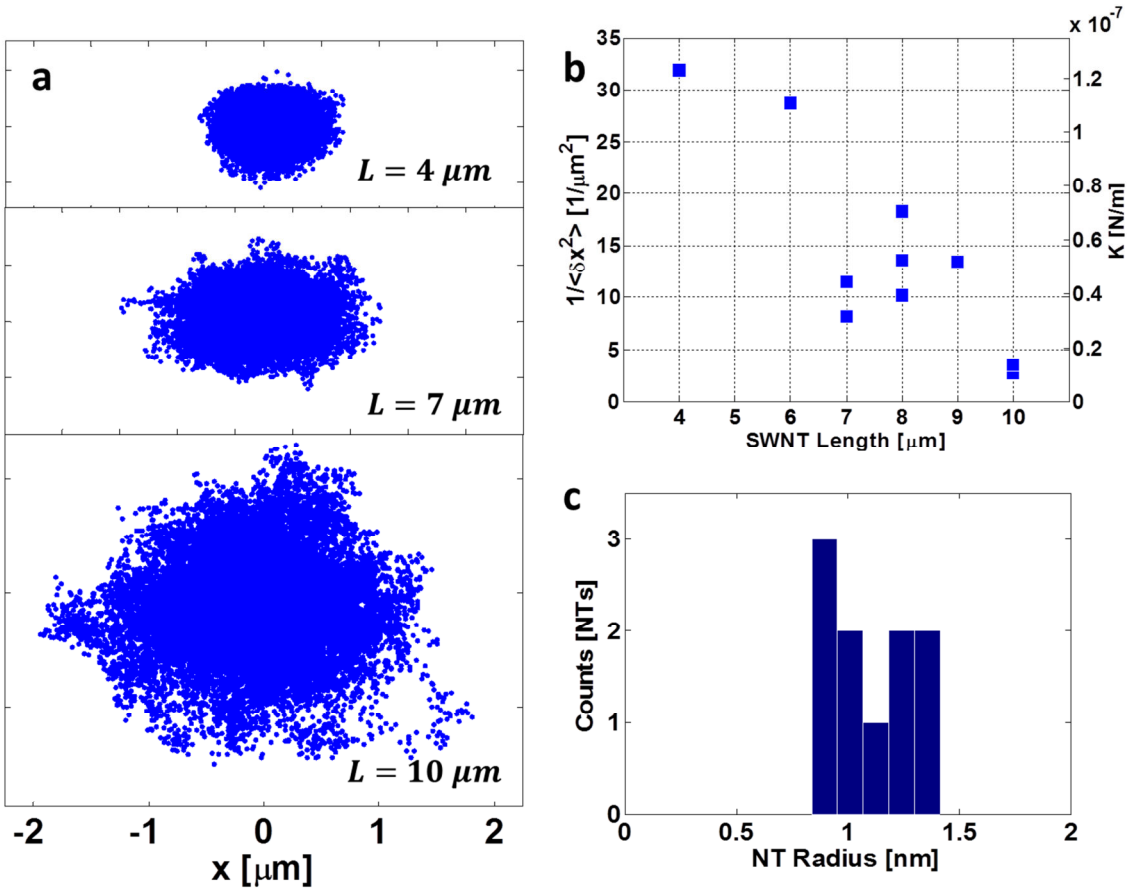

Figure 7.6 Thermal fluctuation results. (a) Centroid positions for 20,000 frames for 3 devices, a 4μm, 7 μm, and 10 μm long NT. We note increasing fluctuations with increasing NT length. (b) Inverse squared fluctuations as a function of NT length. This scaled by k_BT gives the NT spring constant seen on the right *y* axis in units of Newton per meter. (c) A histogram of the computed NT radii based on beam theory for the 10 devices measured here. The radii shown here are comparable to those used to make the device, here with a mean radius of 1.1 nm.

7.6 Measurements of the NT Radius and Persistence Length

To verify that the results that we were obtaining were due to properties of the NT, we equated the spring constant from Eqn. 7.1to the spring constant defined by continuum mechanics:

$$\frac{k_BT}{\langle x^2 \rangle} = \frac{\beta_0^4 E t \pi r^3}{L^3} \tag{7.4}$$

where E is the Young's elastic modulus, t the NT sidewall thickness and r and L the NT radius and length respectively. Meanwhile, $\beta_0 = 1.88$ satisfies boundary conditions for a cantilever fixed on one end free to move at the other end oscillating in its fundamental mode. We know the fabricated length of the NT and have measured the fluctuations and can thus solve for the NT radius directly:

$$r_{NT} \cong \left(\frac{k_B T L^3}{\langle x^2 \rangle \beta_0^4 E t \pi} \right)^{1/3} \tag{7.5}$$

We calculate this for all 10 devices and find for the radii, $0.83\,nm \leq r_{NT} \leq 1.41\,nm$ with a mean radius of 1.1 nm. A histogram of the radii distributions for all 10 CNT devices can be seen in 7.9(c).

This is in the range of diameter NTs used to make this device, as can be seen by comparing the AFM analysis in Chapter 3.4, which reflects a mean radius of 0.7 nm, a remarkable agreement indeed. We are therefore able to attribute the various varying spring for equivalent length NT devices constants to same length CNTs to having different radii. These results show our measurements are indeed sensitive enough to accurately measure intrinsic CNT properties.

Likewise a measure of persistence length can be extracted from the fluctuations but it differs in that it does not require explicit assumption of the Young's modulus

$$\ell_p = \frac{\kappa}{k_B T} = \frac{k_{NT} L^3}{\beta_0^4 k_B T} = \frac{1}{\beta_0^4} \frac{L^3}{\langle \delta x^2 \rangle} \tag{7.6}$$

We measure $16\,\mu m \leq \ell_p \leq 757\,\mu m$ with a mean persistence length of 370 µm. These numbers are in agreement with the values attained in(16) for the persistence length of SWNTs with radii similar to our devices.

7.7 Power Spectral Density Analysis

We have seen in Chapter 6 that by fitting our PSD data to theory, we could extract parameters from the frequency domain, such as the diffusion coefficient and corner frequency. We use home written MATLAB code to fit our experimental PSD to the theoretical form. We recall from Chapter 6.5.2 that the power spectral density is given by:

$$PSD(x,f) = \frac{D}{\pi^2(f^2 + f_c^2)} \tag{7.7}$$

We select six of the 6 of the devices we have just studied as they all have the same iron pad geometry—specifically a 2 μm/side equilateral triangular shape. We plot all six PSDs on the graph that can be seen in figure 7.7. We see that at high frequencies (above the corner frequency) all spectra collapse down to the same slope. We know that this is a reflection of the dissipation in the Fe-pad/NT geometry. A plot of the PSD vs. frequency is shown in Figure 7.7 with each color and fit corresponding to a different NT device of particular length as in the legend

As the area under the PSD curve represents the mean squared fluctuations of the system we note that the PSDs of the devices studied here reflect larger fluctuations for longer NTs. We also observe a change in frequency that is length dependent; for instance we find a 10 μm device has a characteristic frequency of ~ 0.1 Hz whereas this increases to ~1.0 Hz for a shorter 4 μm device. In general our data shows frequencies increasing with decreasing NT length.

. By using our fit parameters for the corner frequency and the zero frequency intercept, we are able to solve for the diffusion coefficient using Eqn. (7.7). We find values of $0.16 \leq D \leq 0.28$ μm2/Hz with a mean value of $D = 0.21\ \mu m^2/Hz$. As the diffusion coefficient is largely determined by the size and geometry of the Fe pad we expect that each device would have a similar diffusion coefficient, just as we found to be the case here. We do look at the length dependence on the diffusion coefficient and do not see a dependence on NT length.

Furthermore, with the diffusion coefficient we can calculate the effective stokes radius of our iron pad from Einstein's theorem given in Chapter 6.5.1,

$$R_{Stokes} = \frac{k_B T}{6\pi\eta D} \tag{7.9}$$

We find an effective Stokes radius of 1.0 μm, or 2 μm diameter as measured from our PSD fit parameters. This is in excellent agreement with our 2 μm triangular pad.

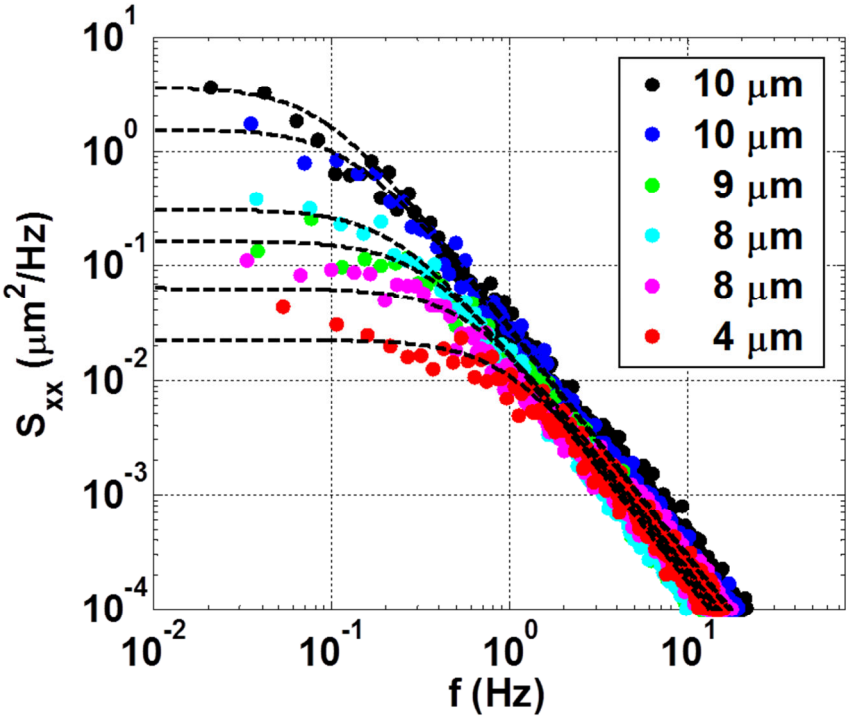

Figure 7.7 Power spectral densities of 6 different length devices attached to triangular iron pads 2 μm/side. The mean squared fluctuations are the areas under the PSD curves. We see in general that longer NTs have larger fluctuation density (Black and blue dots represent two different 10 um devices) than shorter NTs (red, magenta dots). (Refer to legend) Meanwhile, all six curves converge roughly to the same slope at high frequencies (f>fc). This represents the diffusion coefficient of the system which is determined by the size and shape of the probe, with a mean value of 0.21 [$\mu m^2/s$] for our 2 μm triangular devices.

7.8 Conclusion

We have seen that from thermal fluctuations alone we can extract from our NT system the spring constant, the persistence length as well as the diffusion coefficient and effective stoked radius of our pad. In particular the NT radii calculated based on fluctuation measurements were in the distribution of NT radii that were used to make the devices. Power spectral density fluctuations showed the length dependent nature of the fluctuation amplitudes, as well as gave diffusion coefficients that are representative of the size scale of our Fe pad.

This is rather remarkable when one considers the extreme size scales in operation. An iron metal pad on order thousands of times larger than the NT fluctuates due to random motion, and in doing so reveals the physical properties of NT that it is attached to with remarkable precision.

It is interesting to note that the earth's magnetic field serves to orient the Fe pad, but does not affect the obtainment of fundamental physical properties as we just saw. This is because it is a constant B field and does not actually exert a tensioning force on the pad. However there is a large energy cost associated with this orientation that causes the Fe pad to rotate and the NT to bend to accommodate this. The energy cost for the magnet pad aligned in the earth's is field given by $U = -\mu \cdot B \approx 2 * 10^{-18}[J]$ is approximately the same cost it takes to bend a 1 nm radius NT 5 µm long with a 1 µm radius of curvature ($\approx 2.7 * 10^{-19}[J]$).

The fact that our magnet pads orients in earth's field is indication of their flexibility. This is characterized by the very low spring constants we measured. This flexibility could be utilized to make a CNT into a sensitive electromagnetic probe to detect local magnetic fields.

Chapter 8

Tensioning the NT with a Magnetic Field

8.1 Introduction

In this chapter we continue to investigate the magnetic NT devices described in Chapter 7. Now we apply an external magnetic field via an electromagnet to tension the NT as is shown conceptually in Figure 8.1(a).

We will first look at the details of our magnetic measurement setup and then determine the magnetic moment of the Fe pads. We then describe how we calibrate the forces acting on the NT using thermal fluctuations. We discuss the model of the NT in the high-tension regime and determine the magnetic moment of the system by appropriate normalization of the slope of the force vs. magnetic field gradient plot. We analyze the data using the PSD analysis methods described in Chapter 6 and from the frequency domain extract the diffusion coefficient. We conclude by discussing force regimes that will be interesting to investigate.

8.2 Experimental Setup and Measurements

To tension our NT devices we used an electromagnet with 1200 turns of 32-gauge magnet wire coiled about an aluminum spool 1.5 cm in length. An image of this can be seen in Figure 8.1(b). The spool core is bored with a 500 micron diameter hole along the spool axis. A 500 micron diameter Permalloy-80 wire sharpened on one end to a 50 micron diameter point is inserted into the core, with the sharpened end extending from the core by 3 mm. The magnetic core serves to increases the magnitude of the field generated in the solenoid by a dimensionless factor called the relative permeability of the material, μ_r, as in the expression $B = \mu_r B_0$ where $B_0 = \mu_0 nI$ is the field of the solenoid with an air core given N turns per unit length with current I. In the case of Permalloy-80, the relative permeability μ_r can range from 8,000 to 100,000 depending on process

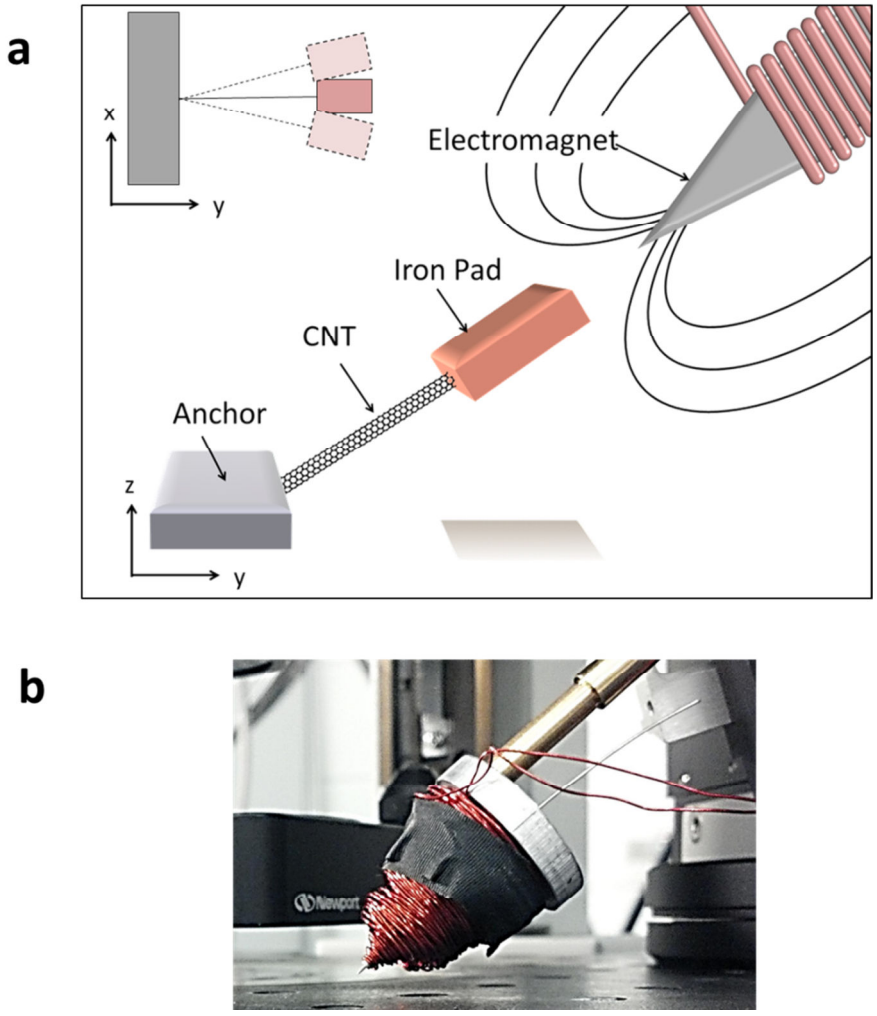

Figure 8.1 (a) A schematic (not to scale) of a Fe tagged CNT being tensioned by the magnetic field of an electromagnet with needle-like probe geometry. (b) A photo of the electromagnet used in the experiments described in this chapter. The magnet wire is seen coiled along the magnet's 1.5 cm length. A 500 µm Permalloy-80 core extends from the solenoid by 3mm and is sharpened to a 50 µm point at the end.

conditions such as high-temperature annealing. The core allows the magnetic field to be extended beyond the solenoid coils as the high susceptibility of the material will cause the field to lie along the solenoid axis. The needle-like probe geometry creates high magnetic field gradients close to the tip. The Pemalloy-80 wire is too flexible for machining so tips are sharpened by taking a 2 inch length of the wire in vice grips and lapping off the tip with a rolling motion to get at all sides of the wire. Tips can be shaped in this way down to 50 μm in diameter. During experiment one must use caution so as not to bump the probe tip into the surface as the Permalloy-80 is a soft material and contact can readily cause a blunting of the tip.

We first characterize the properties of the magnet. In Figure 8.2 we see the magnetic field of our electromagnet as a function of current through the solenoid. We see that Permalloy-80 is a soft ferromagnetic material as it exhibits extremely low hysteresis (~5 Gauss in width in our calibrations also upper left inset in Figure 8.2). We can compare these curves with those used in earlier experiments using a carbon enhanced steel core as seen in the black line of the lower right inset of Figure 8.2. We note that the steel tips exhibit a larger hysteresis making it difficult to turn the field on and off in a predictable manner.

In Figure 8.3 we can see the full configuration of the experimental setup. The electromagnet is mounted on an XYZ piezo nano-manipulator which positions the magnet over the device area with 100 nm precision. The tapered design of the solenoid allows the needle-like tip to be brought within 10 microns of the sample surface without hindrance when positioned at a 30° angle with respect to horizontal. The magnetic field is controlled via the current through a LabVIEW interface. The voltage is set by a DAC card. A 10:1 or 100:1 voltage divider is used to deliver a more stable signal at low voltages. The output signal is fed into a power amplifier which maintains a steady-state DC current to the solenoid. The magnitude of this current is read from the power amplifier via a voltage preamplifier fed into the National Instruments DAC card. This data was recorded with the video data for every frame.

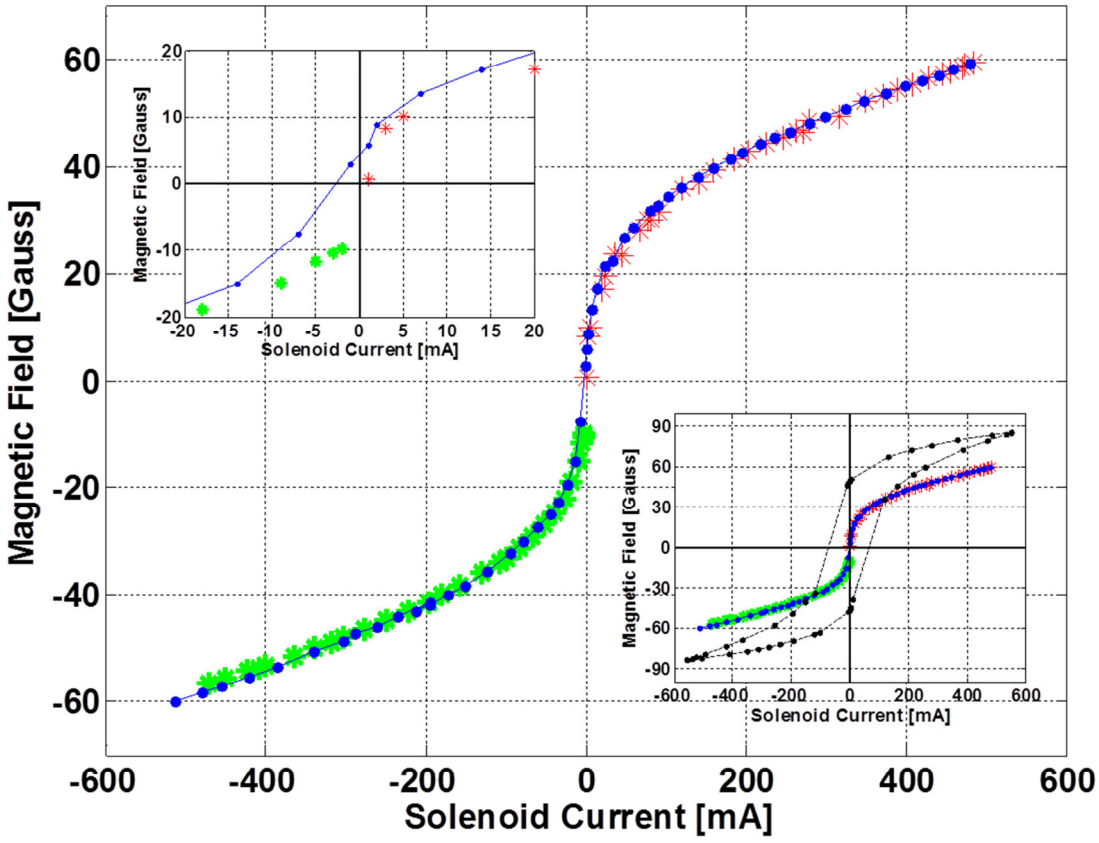

Figure 8.2 Magnetic field 500 µm from the probe tip as a function of current to the electromagnet. In the main figure the current is increased from 0 to 0.5 Amperes (red) then reduced to -0.5 Amperes (blue) and back up to zero (green) shows almost no hysteresis. Looking closer at the upper left insert we see that there is a small hysteresis near the origin of ~ 5 mA and 10 Gauss. Lower right insert shows main figure overlaid with magnetic field vs. current characteristics of a carbon enhanced steel core sharpened to a similar point (black curve). We note that there is a large hysteresis with steel that makes it undesirable for these experiments.

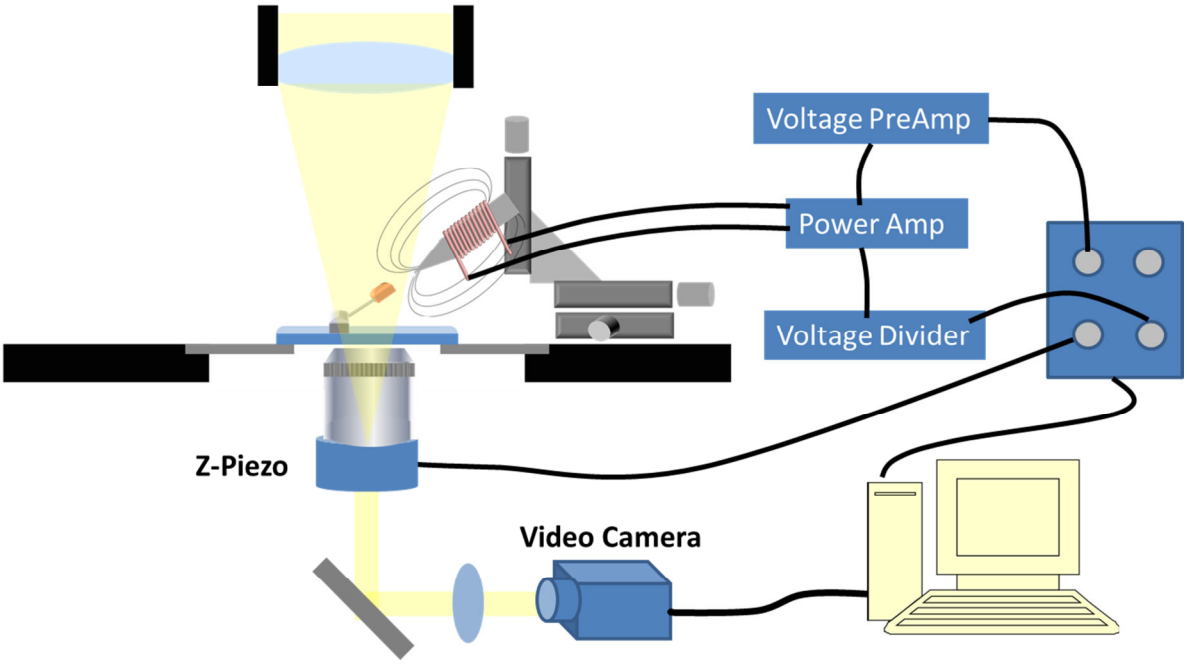

Figure 8.3 Single Pole Electromagnet setup for CNT experiments. The electromagnet is shown mounted on a nanopositioner mounted on a microscope stage which moves it precisely with respect to the device under investigation. A LabVIEW interface provides controls to the solenoid current and the focus as well as image acquisition parameters. Raw data is in the form of video.

8.3 Magnetic Moment of the Pad

We saw in Chapter 7 how the magnetic pads of our NT devices have intrinsic magnetic moments that aligned with the lab-frame magnetic field. We now determine the direction of the magnetic moment of the pad in a more controlled method.

The magnet is brought in at a 30° angle with respect to the device and positioned ~ 110 μm horizontally and 50 μm vertically away from the device under investigation, oriented so as to tension the NT against the anchoring contact along the NT length. We control the current to the solenoid about I = 0 where we can switch between a net clockwise or counterclockwise current through the solenoid, hence producing an alternating positive and negative magnetic field. Figure 8.4 (a) and (b) show the pad tensioned under a positive and negative magnetic field respectively. We observe that the device flips sharply when the polarity of the device is reversed, noting that

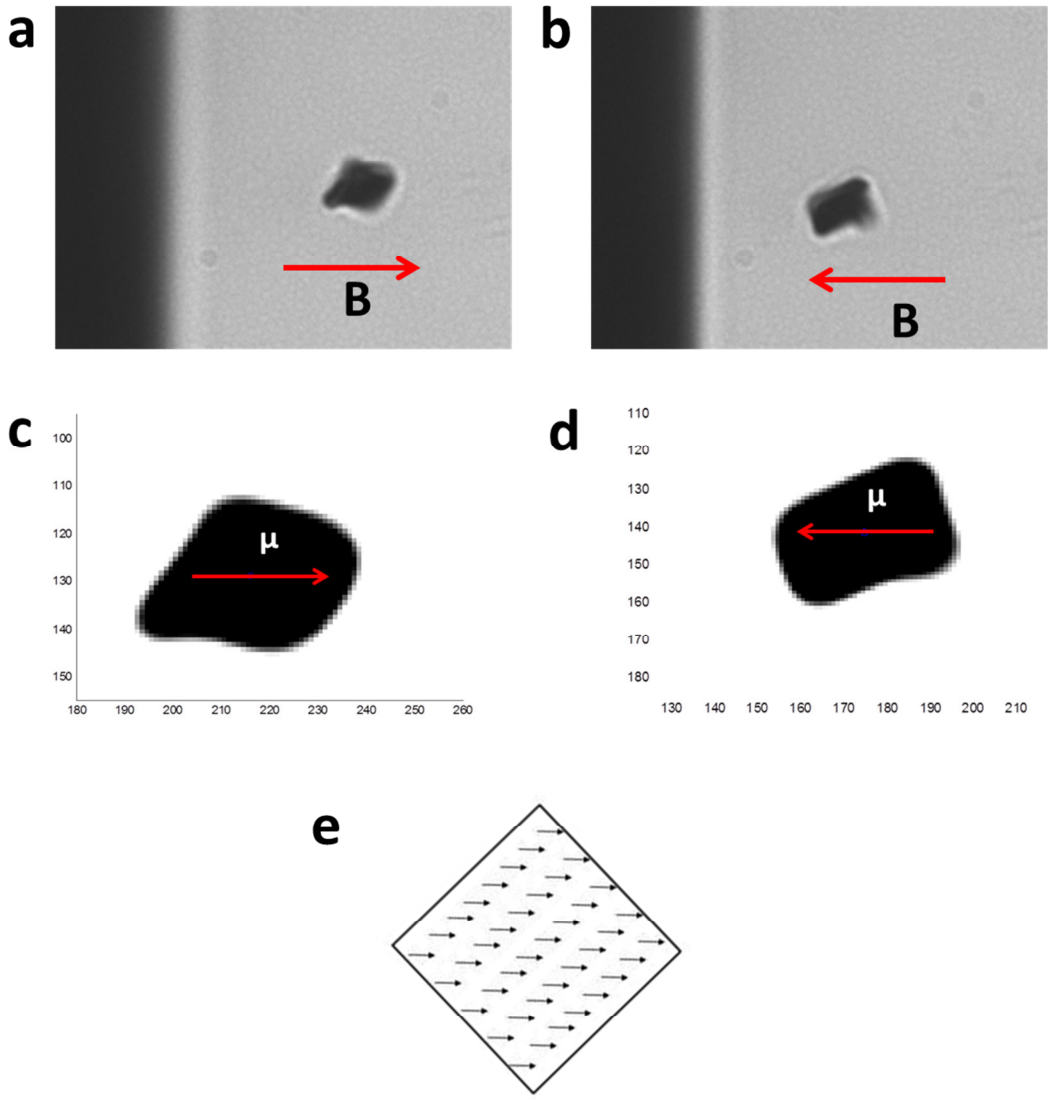

Figure 8.4 Video frames of Fe pad flipping orientation with B field polarity change. Switching the polarity of the field reveals the magnetic moment of the pad. (a) and (b) show video frames with the net in plane direction of the magnetic field indicated by the red arrow. (c) and (d) Show the processed images with the magnetic moment illustrated by the red arrow along the diagonal of the pad. (e) A schematic of magnetic diploes of a ferromagnetic material where the magnetic domains are preferentially aligned along the long axis of the diagonal.

the device appeared to be tensioned (extended along its length) with just the application of a milliamp of current. The magnetic moment will align with the magnetic field to minimize its energy according to $U = -\mu \cdot B$. By the tensioned pad's orientation with respect to the electromagnet it is clear that the magnetic moment lies along the diagonal, as in shown in Figures 8.4(c) and (d) superimposed on the processed image at each orientation.

Shape anisotropy becomes especially important in thin films. The dipolar anisotropy energy per unit volume is for a continuum film is given by(81):

$$E = \frac{1}{2}\mu_0 M_S^2 cos^2(\theta) \tag{8.1}$$

Where M_S is the saturation magnetization and θ is an angle with respect to the surface normal. We thus see the energy is minimized when the moment lies in the plane of the film *(θ=90°)*, which for us is the 150 nm thickness of the Fe pad. The shape of the area of the pad can also induce shape anisotropy, and we observe for our square and rectangle pads the magnetic moment is along the long, diagonal axis, as is predicted by theory(82).

8.4 Tensioned CNT Results.

We now demonstrate that we can exert precise forces on our NT device. In our method we used the thermal fluctuations to calibrate the forces acting on the NT. We will first present results from measurements made on one device, a 10-micron-long NT attached to a 2 μm X 3 μm X 150 nm Fe pad. This data is representative of other devices we tensioned in this way. We orient the electromagnet axis to the NT axis so that the tensioning force pulls against the contact the NT is anchored under. We then measure fluctuations of the Fe pad for ~40,000-60,000 frames for each value of solenoid current ranging from 5 mA to 300 mA.

We analyzed the video frames as was described in Chapter 7.6 and found the centroid distribution of the Fe pad as a function of current to the magnet. Figure 8.5 shows raw centroid data showing the x-y position for the device tensioned with a solenoid current of 4 mA, 80 mA

and 310 mA. We see that increasing current (and hence the magnetic field and magnetic field gradient) results in a decreased region traversed by the pad. We also note this device has a preferential motion nearly perpendicular to the NT axis and to the magnetic field, and additionally shows larger fluctuations perpendicular to the NT and the tensioning force. This movement orientation is maintained throughout all 23 measurements.

Again we calculate the variance of the fluctuations at each tensioning force. We see the results these measurements in Figure 8.6 which shows inverse squared fluctuations as a function

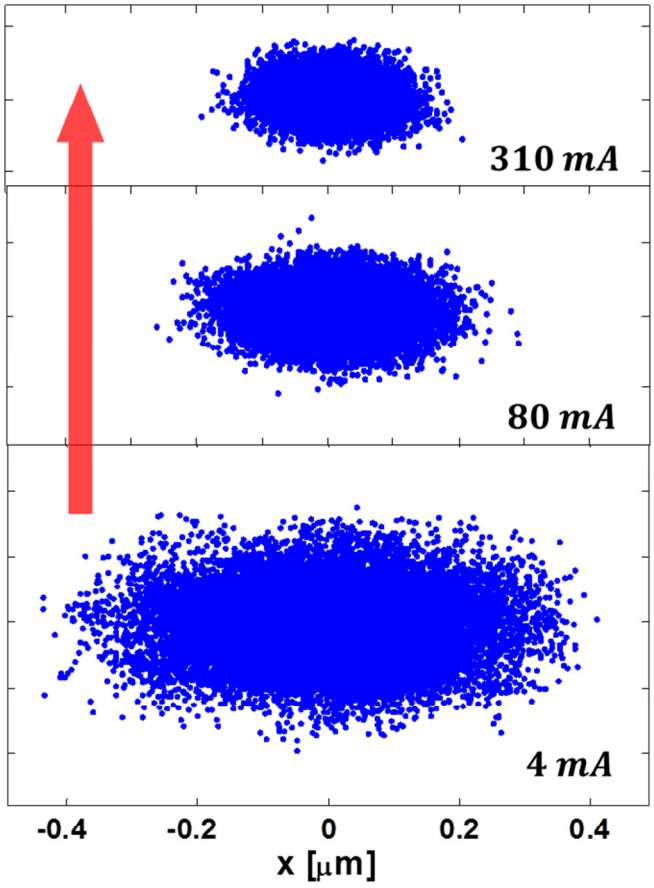

Figure 8.5 Distribution of fluctuation in the image plane. These represent data from one device that was 12 microns in length. Shown are three values of current to the solenoid. We see as the magnetic force is increased the amplitude of the fluctuations in both X and Y decrease, representative of the effective steepening the walls of the confining potential. The red arrow indicated the direction of increasing tension of the device.

of the magnetic field applied for the device. We assume that in the limit of large B fields the magnetic force dominates over the elastic forces of the NT and we can approximate the restoring potential as due to the magnetic field alone:

$$k_{mag} = \frac{k_B T}{\langle \delta x^2 \rangle} = \frac{F_{mag}}{L} \tag{8.2}$$

The geometry of the tensioned NT simplifies to that of a simple pendulum, which relates the restoring force to the spring constant by $k = F/L$. Therefore, using Equation 8.2 we can calibrate the forces directly from the fluctuations. The right hand y axis in Figure 8.6 shows the magnetic force calibrated for each measurement.

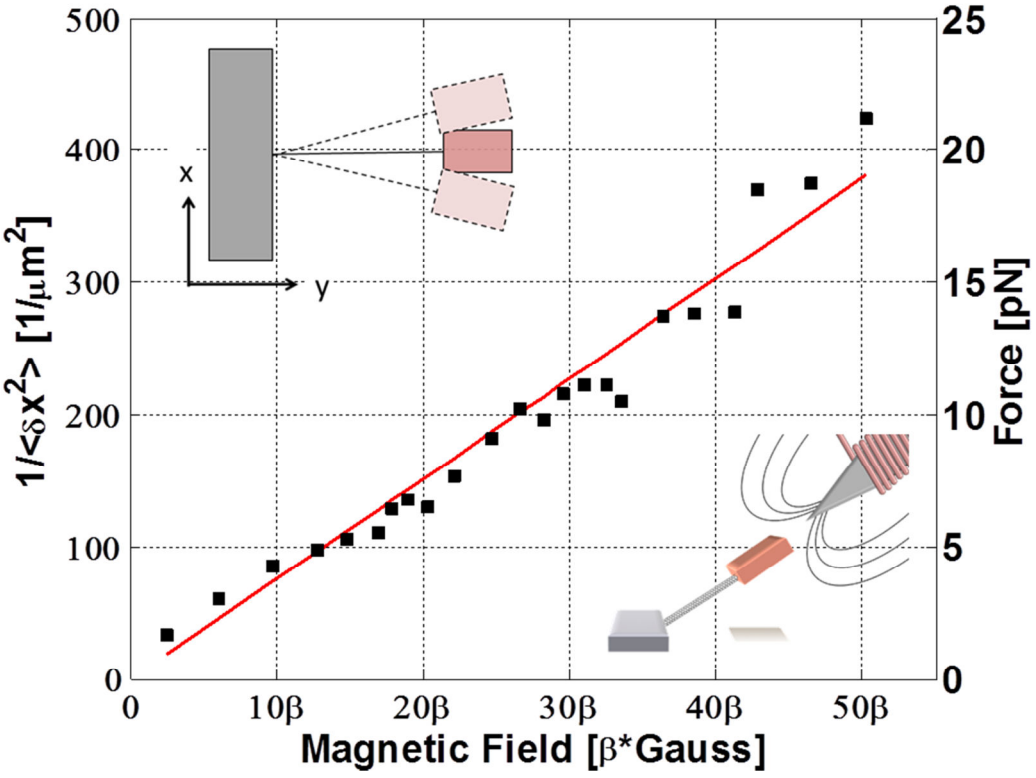

Figure 8.6 Inverse squared fluctuations as a function of magnetic field. This data is for one device measured at 23 different values of solenoid current. Calibrated forces are indicated by the right hand y axis. Note that the magnitude of the magnetic field is scaled by β.

We see that through thermal fluctuation measurements alone we are able to precisely calculate and thus calibrate the forces on the tethered NT system with 100 fN sensitivity from 1 pN to 21 pN, independent of any information of the device other than its length and a measurement of its thermal fluctuations.

F is a magnetic force which we know to be $F_{mag} = \mu \nabla B$. Here for convenience we align our coordinate axis *r* such that it lies along the axis of the electromagnet.

$$k_{mag} = \frac{\mu}{L}\left(\frac{\partial B}{\partial r}\right) \tag{8.3}$$

As this is linear in *B* it is also linear in ∇B. With proper scaling the slope in Figure 8.6 we can extract the proportionality constant μ, the magnetic moment of the Fe pad as is given by the right hand side of Equation (9). Our data finds $\mu \approx 3x10^{-13}[T/m]$ (using a rough method of estimating dB/dr) of We compare this with the saturation magnetization for the Fe pad of $\approx 9x10^{-14}[T/m]$. This is within a factor of three and in reasonable agreement.

We might also expect this increasing tension with increasing forces to be accompanied by a subsequent increase in frequency of the device. To see if this is the case we look at the PSDs of the data which give us the frequency content of the fluctuations. The results of this analysis can be seen in figure 4(c) which shows the PSD functions for the data shown in 8.7 with the top red curve representing the lowest force and the bottom black curve the highest force. The black dashed curves are the fits of the data to Eqn. (8.4). The area under these curves gives the variance of the measurement, and the corner frequency gives the characteristic time response of the system and can be seen to increase from ~ 1 Hz to ~10 Hz over a range of 20 pNs of force. These corner frequencies are notably one to two orders of magnitude higher than the corner frequencies we measured in Chapter 7.10 for untensioned devices. This data is consistent with NT mechanics theory where one expects increasing characteristic frequencies with increasing tension.

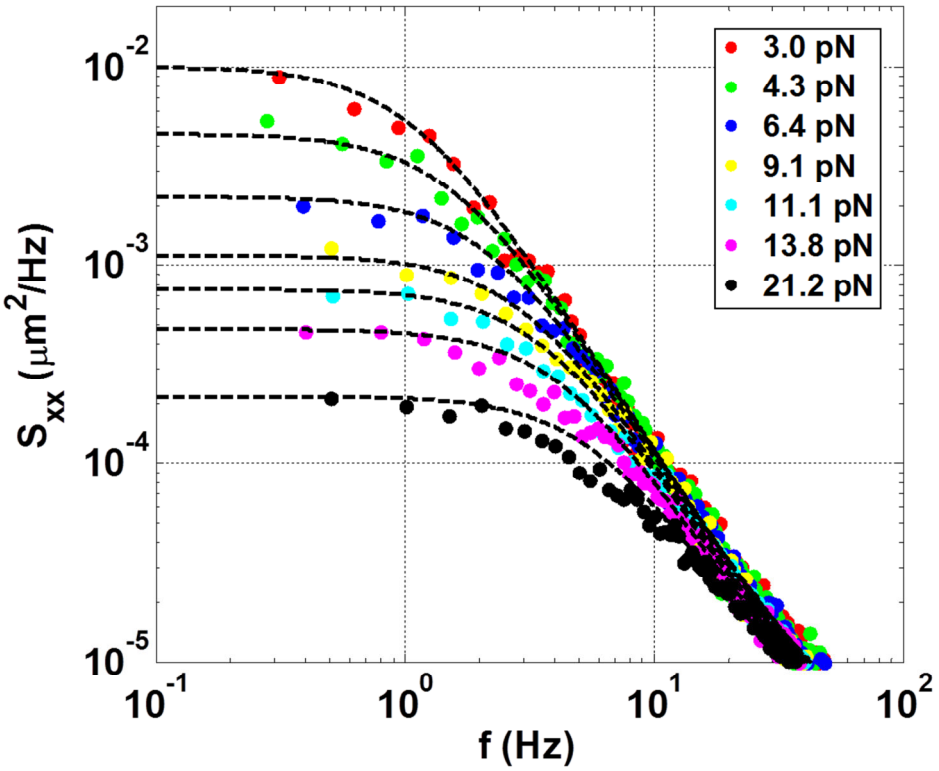

Figure 8.7 Calibration of magnetic forces through power spectral density analysis. We show PSD functions for one device tensioned in a magnetic field at seven different forces. The area under each curve gives the variance of the fluctuations $\langle \delta x^2 \rangle$. We see decreased fluctuation density and increased corner frequency with increasing tensions. The dashed black lines are fits to the data using equation 8.4. The slope of the curves at high frequencies is a measure of the diffusion coefficient.

We note that all seven PSD curves converge to the same slope at higher frequency. Using fit parameters obtained from the fluctuation data we calculate the diffusion coefficient $\langle D \rangle = 0.18\,\mu m^2/s$ for this device. The Einstein-Stokes diffusion equation for a sphere gives $D = (k_B T)/(6\pi\eta R)$. Using our value of D and $\eta = 1$ $[mPa * s]$ for the dynamic viscosity of water we find the effective Stokes radius, $R_s = 1.2\ \mu m$ or an effective diameter of 2.4 microns. This is in excellent agreement with this device with its 2 µm by 3 µm rectangular Fe pad. We note how a larger pad results in a smaller diffusion coefficient than that found in Chapter 6.7 with smaller pad geometry.

8.5 Tensioning the NT in Opposite Polarity Magnetic Fields

We now look at effect of tensioning a NT device in magnetic fields of both polarities. The NT we used for these studies was 10.5 microns long with a 2 x 3 micron pad attached. In Figure 8.8(a) we see video frames of the device in both a negative and positive magnetic field as indicated by the arrows and equivalent north-and-south-pointing horizontal fields. We record the fluctuations as a function of solenoid current following the same protocol as outlined for the device in Chapter 8.4. We compute the mean-squared fluctuations from the power spectral density function for each values of solenoid current ranging from -100 mA to +100 mA. We plot the inverse squares displacements as a function of the magnetic field which we see in Figure 8.8(b) for fluctuations along the principal axis of motion, and (c), perpendicular to the principal axis.

We first notice that the behavior is largely symmetrical for positive and negative magnetic fields aside from a small offset about zero due to hysteresis. We see similar values for the slope and variance given equivalent magnetic field magnitudes, regardless of direction of the fields. Additionally the principal axis of motion is the same regardless of the magnetic field orientation, which is perpendicular to the long axis of the NT. The only physical difference in the system tensioned at positive vs. negative fields is a kink in the NT at the anchor point attachment at the Fe pad, and this evidently does not cause a large change in the dynamic system properties

We notice that the curve describing the lower force regime has a slightly parabolic shape. The effects of this could be an interplay between the intrinsic NT properties and the magnetic field forces which may compete at low forces in this device.

With respect to the largest fields that magnetic tweezer geometries such as ours could attain, we are still operating in a relatively low force regime. We could easily get into hundreds of piconewtons, and resolve up to a nanonewton of applied force by reducing the distance between the NT device and the magnet tip to 10 μm, (currently at ~ 100 μm working distance) from

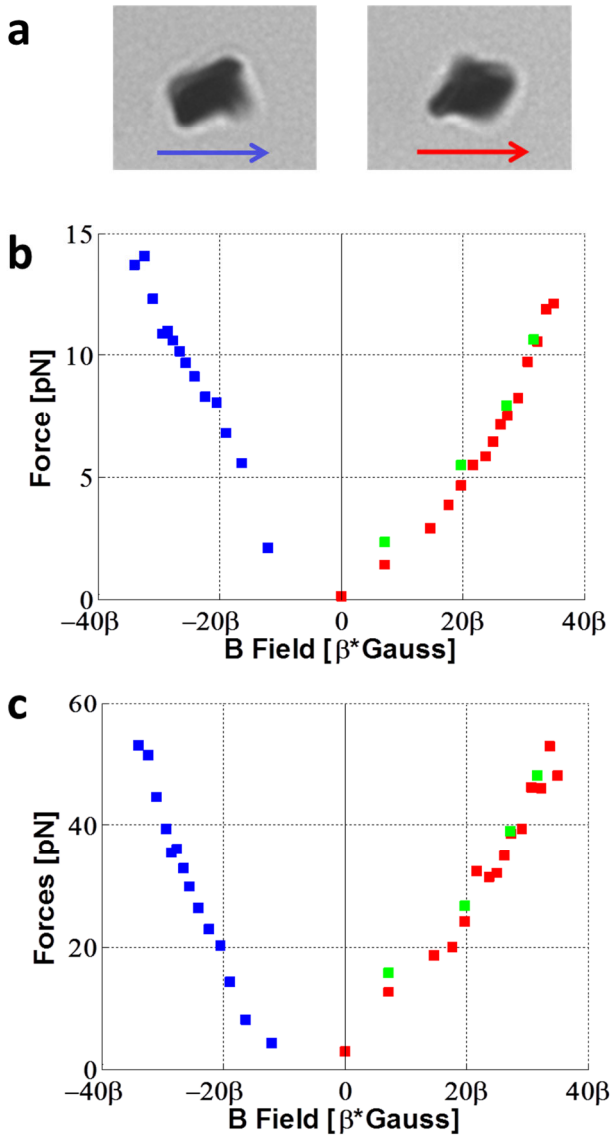

Figure 8.8 A 10.5 μm NT device tensioned in positive and negative magnetic fields. (a) Shows a video image of a 2 X 3 micron Fe Pad as tensioned by a negative (blue arrow) and positive (red arrow) magnetic field. We see the pad flips 180 degrees when the polarity of the field is reversed and that the device behaved symmetrically, (taking into account an offset around zero due to a small hysteresis in the electromagnet). The graphs show inverse-mean-squared fluctuations for the axis parallel (b) to the principal axis of motion and perpendicular (c) to the principal motion. The data was taken from zero current to 100 mA (red) back down to zero (green) and then through negative currents to -100mA (blue).

which we could gain a two orders of magnitude in field gradient alone. Additionally we could increase the current to the electromagnet, which would help up to the point the magnetic core became saturated.

8.6 Conclusions

We have finally gotten a handle on our SWNT via a magnetic field actuator. We have found that we can exert forces on the nanotube from 1 pN to 21 pN with resolution of 100 fN. We used the thermal fluctuations of the device to calibrate it for each value of solenoid current. As in the non-tensioned case in Chapter 7, we were able calculate the diffusion coefficient and corner frequencies using results from PSD analysis and find it to predict a diameter probe consistent with the dimension of our Fe pad. Additionally we showed results from a different device where we tensioned the device in both a positive and magnetic field and saw that the device behaved symmetrically with respect to the direction of the magnetic field.

From the perspective of learning new NT mechanics, it would be interesting to investigate the very low force regime where the intrinsic elastic NT properties compete with forces arising from interaction with the magnetic field. However, from an application standpoint one next step would be to use this geometry for the study of single-molecule—NT interactions, as we will propose in Chapter 9.

Chapter 9

Conclusion: The Next Two Experiments

9.1 Introduction

Throughout this thesis we have outlined a variety of diverse experiments that have included live cell migration experiments, cantilevered NT geometry experiments, as well as magnetic tweezer experiments, the last of which finally allows us to get a handle on a NT with a magnetic grip.

There are two immediate things that we want to do next:

1) Twist up the NT

2) Use this platform for measuring biological forces

As to the former, we will present an experimental platform which we recently developed that is capable of twisting and NTs in ways that has been previously possible for DNA and other linear molecules---we would like to extend this technique to twist CNTs while in a fluidic environment.

We will conclude this thesis with the prospect of using magnetically force clamped NTs in conjunction with optical trapping and fluorescence microscopy to study force interactions between NTs and other biomolecule of interest.

9.2 Carbon Nanotube Rotation Experiments

In DNA magnetic tweezer experiments reviewed in Chapter 6, the DNA was generally twisted. As the molecule was twisted it eventually gave up its torsional train by the formation of a loop structure which is called a plectonemes. We would like to be able to study the formation of such mechanical structures in CNTs by twisting them as well and have already conducted preliminary experiments. We begin with the same NT device structure as experimented on in chapters 7 and

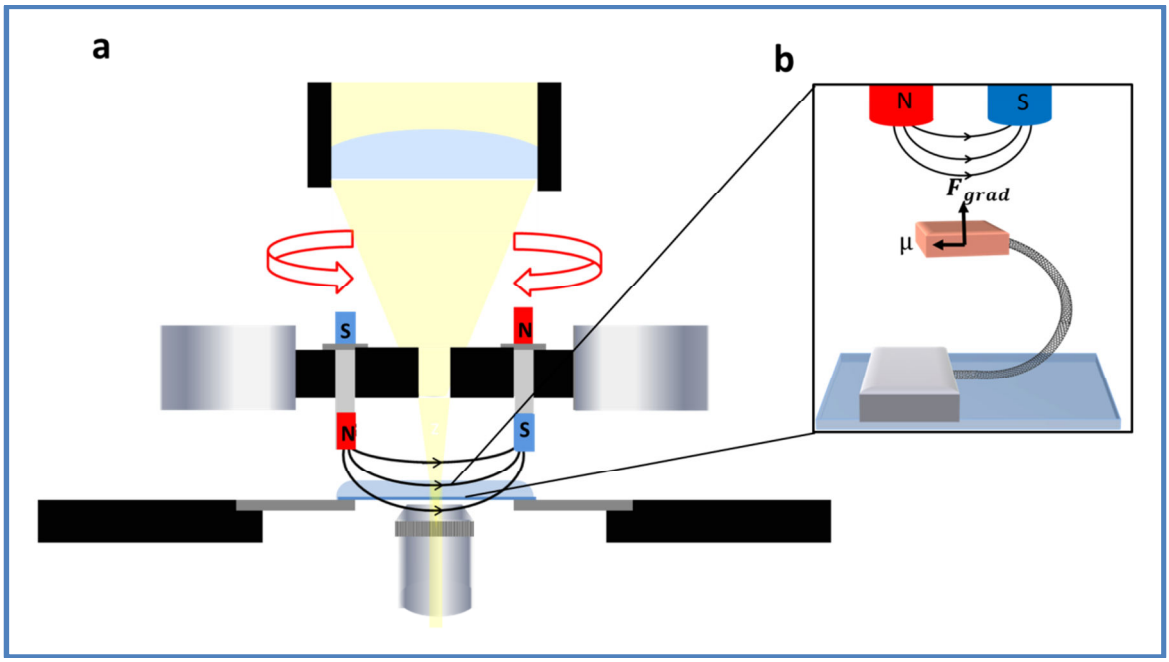

Figure 9.1 Configuration of rotation magnet geometry used in NT twisting experiments. We see two magnets 3mm in diameter each separated by 20 mm and held off the substrate by 2 mm, held in a rotation stage that is rotated over the device sample chip along the optic axis of the microscope objective.

8, with iron tagged SWNTs. We built a magnetic setup specifically for twisting experiments which can be seen schematically in Figure 9.1. Here we have a two magnet geometry tweezer design made with two permanent Neodymium magnets separated by a distance of 20 mm. These magnets are mounted into a rotation stage that is aligned over the optic axis. The magnets are brought within 2 mm of the NT device substrate. The results of applying a field like this is a constant magnetic field in the image plane , providing an orienting torque by aligning the magnetic moment of the pad, as seen in inset of figure 9.1(b) with a slight vertical magnetic field gradient, which provides an upward force during the rotation.

The results that follow are from twisting a NT device which showed characteristic individual NT behavior and was 10 microns in length with a Fe pad 3 μm by 5 μm by 150 nm thick with a symmetry breaking tab. The pad was established to have a net magnetic moment in the plane of the pad and along its diagonal. We rotated the magnets in successive 180° degree rotations both

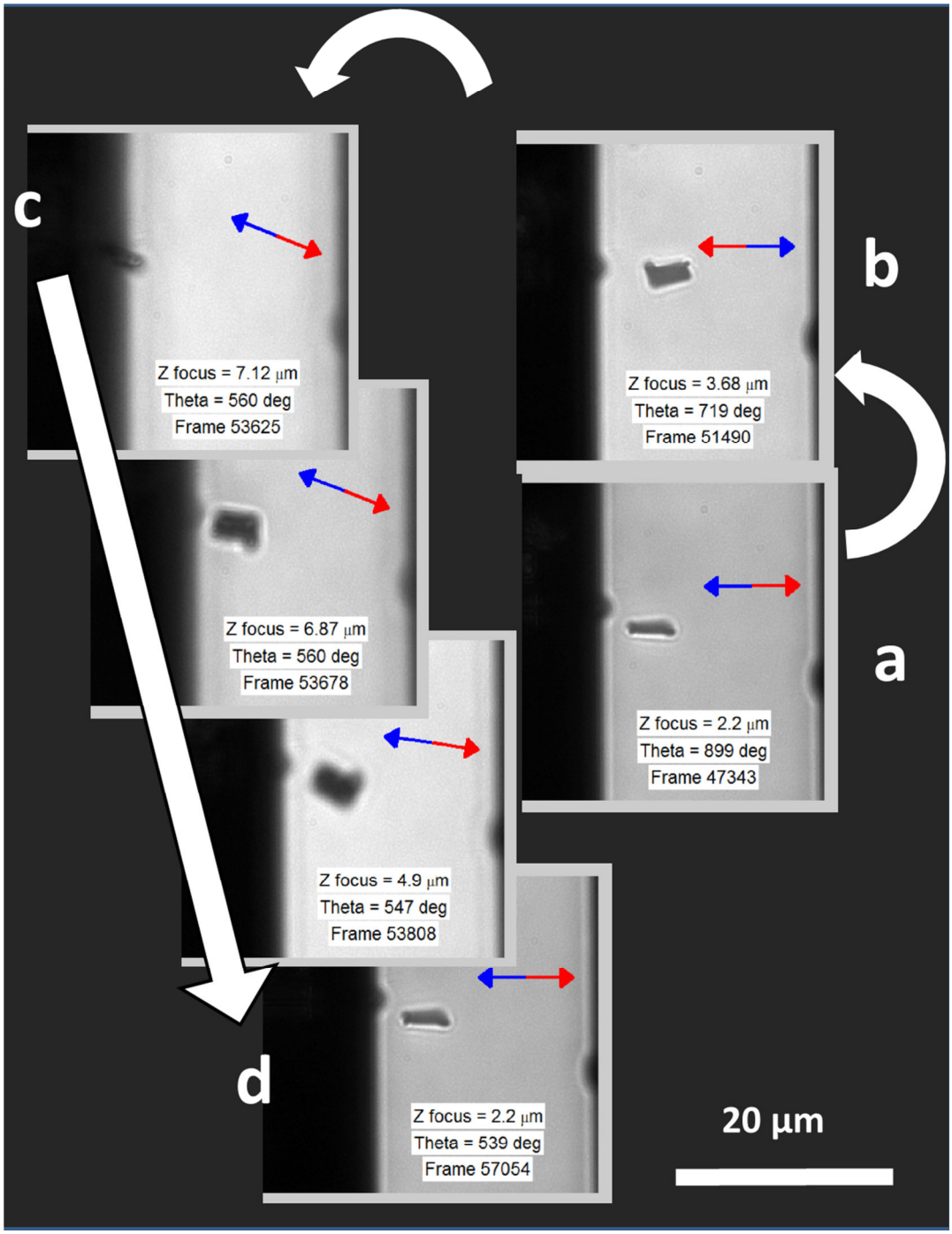

Figure 9.2 Preliminary results from a 360° counter clockwise (CCW) rotation of the magnets over the NT device chip. We start in the lower right with figure (a) where the red and blue arrows denote the north and south pole respectively. We see the difference between (a) and (b) is a 180° rotation CCW. From (b) to (c) there is an additional 165° of motion before the NT resists being twisted and untwists on axis in two 180° flips as is illustrated, returning back to its initial orientation where 9.2(a) and 9.2(d) are equivalent states

clockwise and counterclockwise at a rate of 5°/sec. During the course of these experiments focus was remotely changed using a piezo objective holder controlled through a LabVIEW interface to track the height of the pad during the rotation. Every 180° degrees rotation was stopped and focus was scanned through the pads entire focal plane, thus determining the height of the Fe pad from the surface more precisely at those two locations.

To understand the interesting NT dynamics, we will simply track one 360° counterclockwise rotation beginning with the NT in the configuration shown in figure 9.2(a). In total there are six video frames that summarize the 360° rotation. From Figure 9.2(a) to 9.2((b) the device was twisted about its anchor point 180° Counter-clock-wise (CCW). During this rotation the pad rotated completely in plane without flipping. Another subsequent 180° CCW rotation (completing the 360°) has the following pattern as followed in the image frames of Figure 9.2(c-d-e): First the pad is twisted on edge and swept 90° over the electrode. The NT is moving up as it is twisted and the pad can be seen on edge localized over the NT contact region. When the magnetic field reaches ~ 345° with respect to its initial orientation the device spins clockwise about its axis, (with respect to an end on orientation), undoing the 360° rotation in two distinct 180° flips;(shown by the video frames along the arrow pointing from Figure 9.2(c-d), transitions that take about ~ 3 seconds to complete. Simultaneously the tethered pad relaxes from its extended geometry over the electrode into its initial starting geometry about 3 microns above the substrate. Three subsequent full counterclockwise rotations were performed consecutively, and the behavior of the device was observed to have exactly the same pattern of motion on subsequent rotations.

This is an interesting type of grasp to have on a NT. One thing we will need to do is to first a way to increase the force gradient before these experiments can be successful in bending up a CNT plectoneme. We see that the strength of our magnet is not sufficient to effectively pin both ends of the NT, one end on the substrate and the other end a handle in a magnetic field. To increase the vertical field gradient using permanent magnets one would bring the magnets closer together. It has been shown that reducing the distance between the two permanent magnets to a

1-2 mm gap will increase the field gradient, but the result would only increase our field gradient by a factor or 2 (83)(84). Due to the NTs high flexural rigidity of SWNTs, higher field gradients than this may need to be implemented to overcome the next energy barriers to see morphologies like plectoneme formation in NTs. Higher field strengths that might be required for twisting experiments could possibly be attained with a dual tip electromagnet where both poles were sharpened to a point.

9.3 Force Sensing of Single-Molecule Interactions

One of the things we have discussed is that magnetic tweezer setup in a single pole electromagnet geometry is a constant force clamp. One idea is to use optical tweezers in conjunction with magnetic tweezers to bring biological molecules into contact with the NT and to measure the magnitude of the forces between single molecules and CNTs. If the molecules adhere or de-adhere, then subsequently pulling the molecule away will result in a displacement of the magnetic pad from the trap that should be measurable based on the small spring constant of the NT.

It will also be important to develop a way to image the NT during these experiments. The most non-invasive way one could do this is to implement fluorescent microscopy concurrently with the magnetic and optical trapping geometries. A setup of this sort would allow us to conduct a new class of important bio-mechanical experiments.

REFERENCES

1. Ando T (2009) The electronic properties of graphene and carbon nanotubes. *NPG Asia Mater* 1:17–21.

2. Gittes F, Mickey B, Nettleton J, Howard J (1993) Flexural rigidity of microtubules and actin filaments measured from thermal fluctuations in shape. *J Cell Biol* 120:923–934.

3. Krishnan A, Dujardin E, Ebbesen TW, Yianilos PN, Treacy MMJ (1998) Young's modulus of single-walled nanotubes. *Phys Rev B* 58:14013.

4. Rosenblatt S et al. (2002) High performance electrolyte gated carbon nanotube transistors. *Nano Lett* 2:869–872.

5. Heller I et al. (2008) Identifying the Mechanism of Biosensing with Carbon Nanotube Transistors. *Nano Lett* 8:591–595.

6. Heller I, Smaal WTT, Lemay SG, Dekker C (2009) Probing Macrophage Activity with Carbon-Nanotube Sensors. *Small* 5:2528–2532.

7. Larrimore L (2006) Chemical and Biological Sensing with Carbon Nanotubes in Solution.

8. Zhou X, Moran-Mirabal JM, Craighead HG, McEuen PL (2007) Supported lipid bilayer/carbon nanotube hybrids. *Nat Nanotechnol* 2:185–190.

9. Staii C, Johnson AT, Chen M, Gelperin A (2005) DNA-Decorated Carbon Nanotubes for Chemical Sensing. *Nano Lett* 5:1774–1778.

10. Maehashi K et al. (2007) Label-Free Protein Biosensor Based on Aptamer-Modified Carbon Nanotube Field-Effect Transistors. *Anal Chem* 79:782–787.

11. Larrimore L, Nad S, Zhou X, Abruña H, McEuen PL (2006) Probing Electrostatic Potentials in Solution with Carbon Nanotube Transistors. *Nano Lett* 6:1329–1333.

12. Allen BL, Kichambare PD, Star A (2007) Carbon Nanotube Field-Effect-Transistor-Based Biosensors. *Adv Mater* 19:1439–1451.

13. Balasubramanian K, Burghard M, Kern K, Scolari M, Mews A (2005) Photocurrent Imaging of Charge Transport Barriers in Carbon Nanotube Devices. *Nano Lett* 5:507–510.

14. Balasubramanian K et al. (2004) Photoelectronic transport imaging of individual semiconducting carbon nanotubes. *Appl Phys Lett* 84:2400.

15. Avouris P (2012) Spatially Resolved Electrostatic Potential and Photocurrent Generation in Carbon Nanotube Array Devices.

16. Fakhri N, Tsyboulski DA, Cognet L, Weisman RB, Pasquali M (2009) Diameter-dependent bending dynamics of single-walled carbon nanotubes in liquids. *Proc Natl Acad Sci* 106:14219–14223.

17. O'Connell MJ (2002) Band Gap Fluorescence from Individual Single-Walled Carbon Nanotubes. *Science* 297:593–596.

18. Havener RW, Tsen AW, Choi HC, Park J (2011) Laser-based imaging of individual carbon nanostructures. *NPG Asia Mater* 3:91–99.

19. Cherukuri P, Bachilo SM, Litovsky SH, Weisman RB (2004) Near-Infrared Fluorescence Microscopy of Single-Walled Carbon Nanotubes in Phagocytic Cells. *J Am Chem Soc* 126:15638–15639.

20. Kam NWS, O'Connell M, Wisdom JA, Dai H (2005) Carbon nanotubes as multifunctional biological transporters and near-infrared agents for selective cancer cell destruction. *Proc Natl Acad Sci U S A* 102:11600–11605.

21. Wallace EJ, Sansom MSP (2008) Blocking of Carbon Nanotube Based Nanoinjectors by Lipids: A Simulation Study. *Nano Lett* 8:2751–2756.

22. Pogodin S, Baulin VA (2010) Can a Carbon Nanotube Pierce through a Phospholipid Bilayer? *ACS Nano* 4:5293–5300.

23. Shi X, von dem Bussche A, Hurt RH, Kane AB, Gao H (2011) Cell entry of one-dimensional nanomaterials occurs by tip recognition and rotation. *Nat Nanotechnol* 6:714–719.

24. Chen X, Kis A, Zettl A, Bertozzi CR (2007) A cell nanoinjector based on carbon nanotubes. *Proc Natl Acad Sci* 104:8218–8222.

25. Vakarelski IU, Brown SC, Higashitani K, Moudgil BM (2007) Penetration of Living Cell Membranes with Fortified Carbon Nanotube Tips. *Langmuir* 23:10893–10896.

26. Martinez J et al. (2005) Length control and sharpening of atomic force microscope carbon nanotube tips assisted by an electron beam. *Nanotechnology* 16:2493–2496.

27. Wilson NR, Macpherson JV (2009) Carbon nanotube tips for atomic force microscopy. *Nat Nanotechnol* 4:483–491.

28. Qian D, Wagner GJ, Liu WK, Yu M-F, Ruoff RS (2002) Mechanics of carbon nanotubes. *Appl Mech Rev* 55:495.

29. Li C, Chou T-W (2003) A structural mechanics approach for the analysis of carbon nanotubes. *Int J Solids Struct* 40:2487–2499.

30. Sazonova V (2006) A tunable Carbon Nanotube Resonator.

31. Gautschi W (2008) Leonhard Euler: His Life, the Man, and His Works. *SIAM Rev* 50:3–33.

32. Bozkurt S, ztrk B (2012) in *Advances in Computational Stability Analysis*, ed Coskun SB (InTech). Available at: http://www.intechopen.com/books/advances-in-computational-stability-analysis/elastic-stability-analysis-of-euler-columns-using-analytical-approximate-techniques [Accessed November 2, 2013].

33. Brinkers S, Dietrich HRC, de Groote FH, Young IT, Rieger B (2009) The persistence length of double stranded DNA determined using dark field tethered particle motion. *J Chem Phys* 130:215105.

34. Iijima S, Brabec C, Maiti A, Bernholc J (1996) Structural flexibility of carbon nanotubes. *J Chem Phys* 104:2089.

35. Yakobson BI, Brabec CJ, Bernholc J (1996) Nanomechanics of carbon tubes: instabilities beyond linear response. *Phys Rev Lett* 76:2511–2514.

36. Rochefort A, Avouris P, Lesage F, Salahub DR (1999) Electrical and mechanical properties of distorted carbon nanotubes. *Phys Rev B* 60:13824.

37. Rochefort A, Avouris P (1999) Electrical and Mechanical Properties of Twisted Carbon Nanotubes. *ArXiv Prepr Cond-Mat9904411*. Available at: http://arxiv.org/abs/cond-mat/9904411 [Accessed November 16, 2013].

38. Hertel T, Walkup RE, Avouris P (1998) Deformation of carbon nanotubes by surface van der Waals forces. *Phys Rev B* 58:13870.

39. Yu M-F, Kowalewski T, Ruoff R (2001) Structural Analysis of Collapsed, and Twisted and Collapsed, Multiwalled Carbon Nanotubes by Atomic Force Microscopy. *Phys Rev Lett* 86:87–90.

40. Troiani HE et al. (2003) Direct Observation of the Mechanical Properties of Single-Walled Carbon Nanotubes and Their Junctions at the Atomic Level. *Nano Lett* 3:751–755.

41. Cozzarelli NR, Cost GJ, Nöllmann M, Viard T, Stray JE (2006) Giant proteins that move DNA: bullies of the genomic playground. *Nat Rev Mol Cell Biol* 7:580–588.

42. Zheng LX et al. (2004) Ultralong single-wall carbon nanotubes. *Nat Mater* 3:673–676.

43. Huang S, Woodson M, Smalley R, Liu J (2004) Growth Mechanism of Oriented Long Single Walled Carbon Nanotubes Using "Fast-Heating" Chemical Vapor Deposition Process. *Nano Lett* 4:1025–1028.

44. Kong J, Cassell AM, Dai H (1998) Chemical vapor deposition of methane for single-walled carbon nanotubes. *Chem Phys Lett* 292:567–574.

45. Dai P (1998) Synthesis of individual singlewalled carbon nanotubes on patterned silicon wafers. *Nature* 395:876–878.

46. Li Y et al. (2010) How Catalysts Affect the Growth of Single-Walled Carbon Nanotubes on Substrates. *Adv Mater* 22:1508–1515.

47. Han S, Liu X, Zhou C (2005) Template-Free Directional Growth of Single-Walled Carbon Nanotubes on a- and r-Plane Sapphire. *J Am Chem Soc* 127:5294–5295.

48. Kocabas C et al. (2005) Guided Growth of Large-Scale, Horizontally Aligned Arrays of Single-Walled Carbon Nanotubes and Their Use in Thin-Film Transistors. *Small* 1:1110–1116.

49. Kang SJ et al. (2007) High-performance electronics using dense, perfectly aligned arrays of single-walled carbon nanotubes. *Nat Nanotechnol* 2:230–236.

50. Ding L, Yuan D, Liu J (2008) Growth of High-Density Parallel Arrays of Long Single-Walled Carbon Nanotubes on Quartz Substrates. *J Am Chem Soc* 130:5428–5429.

51. Li B et al. (2008) Patterning Colloidal Metal Nanoparticles for Controlled Growth of Carbon Nanotubes. *Adv Mater* 20:4873–4878.

52. Nessim GD (2010) Properties, synthesis, and growth mechanisms of carbon nanotubes with special focus on thermal chemical vapor deposition. *Nanoscale* 2:1306.

53. Blees M (2008) Personal Communications and NT Transfer Figures.

54. Tsuneyuki S, Aoki H, Tsukada M, Matsui Y (1990) Molecular-dynamics study of the α to β structural phase transition of quartz. *Phys Rev Lett* 64:776.

55. Patil N et al. (2009) Wafer-Scale Growth and Transfer of Aligned Single-Walled Carbon Nanotubes. *IEEE Trans Nanotechnol* 8:498–504.

56. Hata K, Ohno Y, Kishimoto S, Mizutani T (2011) Improvement in alignment of single-walled carbon nanotubes grown on quartz substrate. *Phys Status Solidi C* 8:561–563.

57. Kang SJ et al. (2007) Printed Multilayer Superstructures of Aligned Single-Walled Carbon Nanotubes for Electronic Applications. *Nano Lett* 7:3343–3348.

58. Ishikawa FN et al. (2009) Transparent Electronics Based on Transfer Printed Aligned Carbon Nanotubes on Rigid and Flexible Substrates. *ACS Nano* 3:73–79.

59. Jiao L, Xian X, Wu Z, Zhang J, Liu Z (2009) Selective Positioning and Integration of Individual Single-Walled Carbon Nanotubes. *Nano Lett* 9:205–209.

60. Jiao L et al. (2008) Creation of Nanostructures with Poly(methyl methacrylate)-Mediated Nanotransfer Printing. *J Am Chem Soc* 130:12612–12613.

61. Ananthakrishnan R, Ehrlicher A (2007) The forces behind cell movement. *Int J Biol Sci* 3:303.

62. Small JV, Stradal T, Vignal E, Rottner K (2002) The lamellipodium: where motility begins. *Trends Cell Biol* 12:112–120.

63. Zheng Y (2012) In vitro microvessels for the study of angiogenesis and thrombosis.

64. Scavelli A et al. (2013) Single cell in-vivo carbon nanotube device with multimodal sensing potential. *AIP Adv* 3:032122.

65. Stevens RM et al. (2000) Carbon nanotubes as probes for atomic force microscopy. *Nanotechnology* 11:1.

66. Nishio M, Sawaya S, Akita S, Nakayama Y (2005) Carbon nanotube oscillators toward zeptogram detection. *Appl Phys Lett* 86:133111.

67. Crick FHC, Hughes AFW (1950) The physical properties of cytoplasm: A study by means of the magnetic particle method Part I. Experimental. *Exp Cell Res* 1:37–80.

68. Bustamante C, Bryant Z, Smith SB (2003) Ten years of tension: single-molecule DNA mechanics. *Nature* 421:423–427.

69. Dittmore A, McIntosh DB, Halliday S, Saleh OA (2011) Single-Molecule Elasticity Measurements of the Onset of Excluded Volume in Poly(Ethylene Glycol). *Phys Rev Lett* 107. Available at: http://link.aps.org/doi/10.1103/PhysRevLett.107.148301 [Accessed September 8, 2013].

70. De Vlaminck I, Dekker C (2012) Recent Advances in Magnetic Tweezers. *Annu Rev Biophys* 41:453–472.

71. De Vries AHB, Krenn BE, van Driel R, Kanger JS (2005) Micro Magnetic Tweezers for Nanomanipulation Inside Live Cells. *Biophys J* 88:2137–2144.

72. Yapici MK, Zou J (2008) Permalloy-coated tungsten probe for magnetic manipulation of micro droplets. *Microsyst Technol* 14:881–891.

73. Single-Molecule Studies Using Magnetic Traps Available at: http://cshprotocols.cshlp.org/content/2012/1/pdb.top067488.full.pdf+html [Accessed May 5, 2013].

74. Neuman KC, Nagy A (2008) Single-molecule force spectroscopy: optical tweezers, magnetic tweezers and atomic force microscopy. *Nat Methods* 5:491–505.

75. Greenleaf WJ, Woodside MT, Block SM (2007) High-resolution, single-molecule measurements of biomolecular motion. *Annu Rev Biophys Biomol Struct* 36:171.

76. Braslavsky I et al. (2001) Objective-type dark-field illumination for scattering from microbeads. *Appl Opt* 40:5650–5657.

77. Dietrich HR et al. (2009) Tethered particle motion mediated by scattering from gold nanoparticles and darkfield microscopy. *J Nanophotonics* 3:031795–031795.

78. De Grooth BG (1999) A simple model for Brownian motion leading to the Langevin equation. *Am J Phys* 67:1248.

79. Lemons DS (1997) Paul Langevin's 1908 paper "On the Theory of Brownian Motion" ["Sur la théorie du mouvement brownien," C. R. Acad. Sci. (Paris) 146, 530–533 (1908)]. *Am J Phys* 65:1079.

80. Bowman RW, Padgett MJ (2013) Optical trapping and binding. *Rep Prog Phys* 76:026401.

81. Johnson MT, Bloemen PJH, Den Broeder FJA, De Vries JJ (1996) Magnetic anisotropy in metallic multilayers. *Rep Prog Phys* 59:1409.

82. Bruno P Physical Origins and Theoretical Models of Magnetic Anisotropy.

83. Lipfert J, Hao X, Dekker NH (2009) Quantitative Modeling and Optimization of Magnetic Tweezers. *Biophys J* 96:5040–5049.

84. Lipfert J, Hao X, Dekker NH (2009) Supplementary Material to Quantitative Modeling and Optimization of Magnetic Tweezers. Available at: http://nynkedekkerlab.tudelft.nl/wp-content/uploads/dekker_biophysical_journal_2009_SI.pdf [Accessed April 14, 2013].